GEOPHYSICAL SIGNATURE OF UNREST EPISODES AT ACTIVE VOLCANIC SYSTEMS: INSIGHTS INTO THE HYDROTHERMAL SYSTEM FINGERPRINT

Lauriane Chardot

A thesis submitted in partial fulfilment of the requirements for the degree of
DOCTOR OF PHILOSOPHY
in the Department of Geological Sciences of the
UNIVERSITY OF CANTERBURY

Supervisors:
Dr. Ben M. Kennedy
Dr. Arthur D. Jolly
Dr. Bruce W. Christenson
Dr. Micol Todesco

September 2015

Dedicated to Uncle Henri, your strength and determination

I know you would have loved to see this

Abstract

The characterisation of unrest signals and eruption precursors is one of the main challenges in volcano research because of the complexity of volcanic systems (e.g., the interplay between magmatic and hydrothermal fluids). This thesis addresses the issue for White Island volcano (New Zealand), and presents a comprehensive analysis of geophysical changes associated with the recent unrest/eruptive episode (2011-2013). A modelling strategy was used to 1. characterise the source of the magnetic and gravity changes during this unrest/eruptive episode, 2. describe the effect of an inclined fumarole on hydrothermal circulation and gravity changes, 3. assess whether volcanic tremor can be used for eruption forecasting at White Island.

The observed magnetic changes were inverted for a dipole, and can be explained by temperature changes at shallow depth below the active crater. The lack of significant gravity changes was then used to constrain the heat source responsible for the magnetic changes. The geophysical changes are consistent with a model involving an episode of increased degassing from a possible shallow magmatic intrusion.

The effect of a period of increased degassing on hydrothermal circulation and gravity changes in the fumarole area was then investigated. Previous studies inferred an inclined conduit for the main fumarole at White Island (fumarole zero). I therefore investigated the effect of such an inclined conduit on hydrothermal circulation and gravity changes at steady state and associated with an unrest episode, using a numerical modelling approach (TOUGH2). The model was constrained using parameters consistent for fumarole zero (small conduit one order of magnitude more permeable than the surrounding medium). The effect of the fumarole inclination is to shift the hydrothermal plume and the gravity anomaly towards the injection area instead of the fumarole outlet. Such a model implies that regular microgravity measurements can inform on the location of the feeding source of the fumarole.

Finally, I calibrated an algorithm implementing the material Failure Forecast Method to issue eruption forecasts from volcanic tremor at White Island. Volcanic tremor increases preceding four out of the five eruptions of August 2011–January 2014 period are well explained by a model where an eruption is a case of material failure due to magma pressurisation. These

tremor increases were therefore likely precursory to the eruptions. The good fit between the model and data allowed the issue of reliable eruption forecasts so that four eruptions (out of the five eruptions of the episode) occurred during forecast eruption windows. The probability of having an eruption during a forecast eruption window is 0.21 for the whole period, 37 times higher than the probability of having an eruption on any day, demonstrating that eruption forecasting capabilities can be enhanced using our procedure.

We conclude that, at White Island, magnetic and gravity measurements are valuable to characterise the unrest source, and that the evolution of volcanic tremor can be used for eruption forecasting. Magnetic measurements can help characterise unrest because of their sensitivity to temperature changes. Additional gravity measurements allow constraining the source of the magnetic changes, and they could also inform on location of the source of the fluid injection in the fumarole area. The evolution of volcanic tremor can be precursory to eruptions and allow an estimate of the timing of the eruptions onset. This study therefore brings insights into unrest sources and eruption precursors at White Island, while providing methods that could be applied at other volcanoes. It also highlights the importance of continuous measurements to constrain volcanic processes.

Acknowledgments

First of all, thank you so much to my four supervisors for guiding me throughout this journey.

- Ben, thanks for your enthusiasm about my project, for your support whenever I needed it, and for always challenging my argumentation. It was very good to have you on the supervisory team because you really made me step back at some crucial times when I had to make sense of all this geophysics.
- Art, thanks for always supporting me in my decisions and for trusting me, for making sure I had everything I needed to do good research, and for the great discussions we have had.
- Bruce, I wished I spent more time with you, because you always inspire me to think forward. I hope we keep working together on all these projects that emerged during this PhD!
- Micol, despite the distance, you have been so responsive and helpful, thank you very much for that! I learnt so much from you in such a short amount of time. Thank you.

I acknowledge the different sources of funding which made this project achievable.

- The University of Canterbury for granting me a doctoral scholarship.
- GNS Science for hosting me and providing me with the facilities to do good research.
- GNS Science Core funding for additional funding for the PhD research and for funding me the TOUGH2 2012 Symposium and the EGU 2015 Conference.
- GeoNet for the co-funded trips to White Island for data collection of Chapter 2 and for the high quality seismic data used in Chapter 4.
- EQC Taupo for the first 6 months where I discovered the method that would make the subject of Chapter 4.

- Mason Trust for additional funding throughout this project.

A huge thanks for the great support from the GNS Science Department of Volcanology, particularly Tony Hurst, and for making me part of the team. It has been a great experience and I learnt so much working by your sides.
Then, thanks for all the support from my friends and family.

- Sam, thanks a lot for your daily support, for listening to me whenever I was a bit lost and for cheering up at my successes. These make you a great friend.

- Thanks to my officemate and friend, Karen, for showing me so many nice places and teaching me a lot about volcano chemistry monitoring, but most of all thank you for your warm daily presence.

- Agnes, it was very nice to talk about volcanoes and to share with you these pleasant breaks. Thanks for your support along the way.

- Isabelle, thank you for always being here whenever I needed help, for a reference or for a quick chat about volcanic processes.

- Natalia, thanks for your advice, your support and your little attentions.

- Debi, thank you for your kindness and generosity, for helping me in my weekly escape towards my Heart Centre and thank you Dani for your smile or word and introducing me to this magical thing.

- Paul and James, thanks for hosting and driving me around during my annual visit to the Uni. Flo, Jonathan, Paul, thank you for making feel welcome. I hope we stay in touch.

- A huge thanks to my parents, brother and sister-in-law for being here whenever I needed to. I miss so much.

Finally, a special thanks to my partner in life who has supported me since the very beginning. No regrets. Doing a PhD is great, but you made my life even more enjoyable. You are such a great companion to share my adventures with. On to the next one! I am so grateful to have you in my life.

Thank you all, and many more, for being part of this journey, I really enjoyed the ride.

Contents

List of Figures

List of Tables

List of Publications

I present below a list of publications that are either in preparation or have been published as peer review articles or conference presentations. They all benefited from the work I did during my PhD. In first author publications (Chapters 2, 3, 4), I performed fieldwork, data processing and interpretation, and I wrote the manuscript. In co-author publications, I contributed to data interpretation, discussion and manuscript editing.
Peer review journals:

- Chapter 4: **Chardot, L.**, Jolly, A. D., Kennedy B.M., Fournier, N., Sherburn, S. 2015. *Journal of Volcanology and Geothermal Research*, 302(C), pp 11-23, doi: 10.1016/j.jvolgeores.2015.06.001.

- Chapter 2: **Chardot L.**, Hurst T., Fournier N., Kennedy B.M., Jolly A.D., Christenson B.W., Todesco M., Evolution of magnetic and gravity observables associated with the 2011-2012 unrest/eruptive episode at White Island volcano (New Zealand), in preparation for *Bulletin of Volcanology.*

- Chapter 3: **Chardot L.**, Todesco M., Christenson B., Kennedy B.M., Jolly A.D., Effect of an inclined fumarole conduit on hydrothermal circulation and gravity changes, in preparation for *Geophysics, Geochemistry, Geosystems.*

- Jolly A.D., **Chardot L.**, Neuberg J., Fournier N., Scott B.J., Sherburn S. 2012 High impact mass drops from helicopter: a new active seismic source method applied in an active volcanic setting. *Geophysical Research Letters*, 39: L12306, doi: 10.1029/2012GL051880.

Conference presentations:

- Fry B., **Chardot L.**, Jolly A. D. 2015 Shallow velocity imaging of an active volcano. AGU Fall Meeting 2014, 15-19 December. San Francisco.

- **Chardot L.**, Jolly A.D., Sherburn S., Fournier N., Kennedy D.B. 2013 The material failure forecast method as a potential eruption forecasting tool: application to the 2012

unrest episode at White Island volcano, New Zealand. Abstract 3P24C-O17 In: IAVCEI 2013 Scientific Assembly: forecasting volcanic activity, July 20 - 24 , 2013, Kagoshima, Japan. Oral

- **Chardot L.**, Christenson B.W., Todesco M., Hurst A.W., Fournier N. 2013 Geophysical changes and hydrothermal activity at the early stage of the White Island 2012 unrest episode. Abstract 1W1E-P11 In: IAVCEI 2013 Scientific Assembly: forecasting volcanic activity, July 20 - 24, 2013, Kagoshima, Japan. Poster.

- Fournier N., Williams C.A., Wallace L.M., Sherburn S., Jolly A.D., Hurst A.W., Scott B.J., **Chardot L.**, Ristau J., Bourguignon S., Beavan R.J. 2013 From subduction processes to volcanic unrest: unravelling domino effects at Lake Taupo caldera, New Zealand. Abstract 1A22F-O21 In: IAVCEI 2013 Scientific Assembly: forecasting volcanic activity, July 20 -24, 2013, Kagoshima, Japan. Oral.

- Nicol A., Gerstenberger M.C., Bromley C.J., Carne R., **Chardot L.**, Ellis S.M., Jenkins C., Siggins T., Viskovic G.P.D. 2013 Induced seismicity, observations, risks and mitigation measures at CO2 storage sites. p. 4749-4756, In: Dixon, T., Yamaji, K. (eds) 11th International Conference on Greenhouse Gas Control Technologies, 18th-22nd November 2012, Kyoto International Conference Center, Japan. Elsevier. Energy procedia 37, doi: 10.1016/j.egypro.2013.06.384.

- **Chardot L.**, Hurst A.W., Fournier N., Jolly A.D., Scott B.J., Mazot A. 2012 Magnetic and gravity changes at White Island volcano prior to the 2012 unrest episode. In: Pittari A., Hansen R.J. (eds) Geoscience Society of New Zealand 2012 conference: abstracts. Geoscience Society of New Zealand miscellaneous publication 134A. Poster

- Gerstenberger M.C., Nicol A., Bromley C.J., Carne R., **Chardot L.**, Ellis S.M., Jenkins C., Siggins T., Viskovic G.P.D. 2012 Seismicity induced by CO2 injection: perceptions, observations and risk management. In: 2012 CO2CRC Research Symposium: program and abstracts. Canberra, ACT: Cooperative Research Centre for Greenhouse Gas Technologies (CO2CRC).

- Gerstenberger M.C., Nicol A., Bromley C.J., Carne R., **Chardot L.**, Ellis S.M., Jenkins C., Siggins T., Viskovic P. 2012 Induced seismicity and implications for CO2 storage risk. Abstract S32A-04 In: AGU Fall Meeting 2012, 3-7 December, San Francisco California: abstracts. Washington, DC.

- Jolly A.D., **Chardot L.**, Sherburn S., Cole-Baker J., Scott B.J., Fournier N., Neuberg J.N. 2012 Dropping sand bags from helicopters: a low cost and environmentally benign approach to determine subsurface velocity and attenuation structure of active volcanic systems. Abstract EGU2012-2189 In: 9th EGU General Assembly, 22-27 April 2012, Vienna.

- Jolly A.D., Neuberg J., Jousset P.G., **Chardot L.**, Fournier N., Scott B.J., Sherburn S. 2012 New applications for helicopter based high impact weight drops (Invited). Abstract V21B-2770 In: AGU Fall Meeting 2012, 3-7 December, San Francisco California: abstracts. Washington, DC.

Chapter 1

Introduction

Abstract

Interpreting signs of volcanic unrest and characterising eruption precursors are challenging tasks because of the complexity of volcanic systems. At White Island volcano (New Zealand), interactions between magma and the volcano hydrothermal system lead to a variety of signals. It is only by understanding the nature of the source of these signals and their evolution with time that an accurate assessment of the state of the volcano can be made and eruption forecasts can be produced.
In this chapter, I will first introduce the aim and objectives of this thesis, then present the context for this research. Finally, I will highlight the research questions addressed in this study and provide an outline of the thesis.

1.1 Thesis aim and objectives

This thesis aims at characterising the source of some geophysical changes associated with the 2011–2013 unrest/eruptive period at White Island volcano, to determine whether they can help interpret volcanic unrest and/or were precursory to the eruptions.
This aim will be reached by achieving the following objectives:

- To characterise the source of the gravity and magnetic changes which accompanied the 2011-2013 unrest/eruptive episode at White Island to assess the usefulness of these magnetics and gravity measurements for unrest characterisation at the volcano.
- To describe the effect of an inclined fumarole conduit on hydrothermal circulation and gravity to highlight the contribution of structural effects to the geophysical observables and help constrain the source of the observables.

- To assess the potential of using increasing levels of volcanic tremor to forecast eruptions at White Island, to determine the tremor characteristics that are precursory for eruptions at the volcano.

This thesis provides a summary of the recent unrest/eruptive episode and associated geophysical observables at White Island. It also assesses the use of magnetic, gravity and seismic data for unrest characterisation and eruption forecasting, using a comprehensive modelling approach. Despite being a hindsight analysis only based on one unrest/eruptive episode, these results give insights into the changes to look for during the next volcanic crisis at this particular volcano. Moreover, the same methodology could be applied to other volcanic systems where similar geophysical changes are observed.

1.2 Geophysical changes during unrest and prior to eruptions

Volcano monitoring involves measuring geophysical and geochemical parameters that are expected to change according to the volcano activity. An appropriate interpretation of these changes can bring some valuable insights into the state of the volcano, and inform on the likelihood of an eruption. Unrest is considered when changes from the normal state of the volcano are depicted (Newhall and Dzurisin, 1988). Each volcano has a different normal state, or background activity, which needs to be well understood to assess when there is departure from that state. An unrest phase can, but not always, lead to an (or several) eruption. Here, I define an eruption as the explosive ejection of fragmented new magma or older solidified material and/or the effusion of liquid lava (Siebert et al., 2015). It is only by recognising precursory phenomena to eruptions that reliable forecasts can be made. Unfortunately, this is a challenging task because of the complexity of volcanic systems (Cashman and Sparks, 2013). Each volcano has its own characteristics implying that, even if the physical processes may be similar, they will produce different observables (Cashman and Biggs, 2014). I focus this study on White Island volcano in New Zealand, where unrest observables and eruption precursors are currently poorly understood. As this volcano is one of the major attractions in the country and a potential threat to aviation, enhancing unrest characterisation and eruption forecasting capabilities would help mitigate human and economic impacts during increased volcanic activity.

Complex processes occur during unrest (Figure 1.1) and preceding eruptions (Acocella, 2014; Rouwet et al., 2014). These lead to a variety of signals to interpret. For example, rock failure and fluid movements (magma and hydrothermal) lead to seismicity (Chouet, 1996; Neuberg et al., 2000; Bean et al., 2014), and can also lead to deformation (e.g., Todesco et al., 2004).

Changes in mass and/or density lead to gravity changes (Rymer, 1994; Todesco and Berrino, 2005). Changes in temperature, stress, flow direction lead to magnetic changes (Rikitake and Yokoyama, 1955; Stacey et al., 1965; Zlotnicki and Le Mouel, 1988). Changes in temperature and gas saturation (hence conductivity) lead to resistivity changes (Rinaldi et al., 2011 and references therein). Geophysical changes can also occur without being associated with unrest (e.g., Legaz et al., 2009; Vandemeulebrouck et al., 2005). Each geophysical technique can bring valuable information into the nature of the changes, but it is only by interpreting the changes together that a full assessment of the state of the volcano can be made. The integration of multiple parameters is exemplified in several well-documented unrest periods (Bardarbunga volcano (Gudmundsson et al., 2014; Sigmundsson et al., 2014), Santorini caldera (Aspinall and Woo, 2014 and references therein), El Hierro volcano (López et al., 2012)). This highlights the need for comprehensive studies when attempting to characterise unrest and eruption precursors.

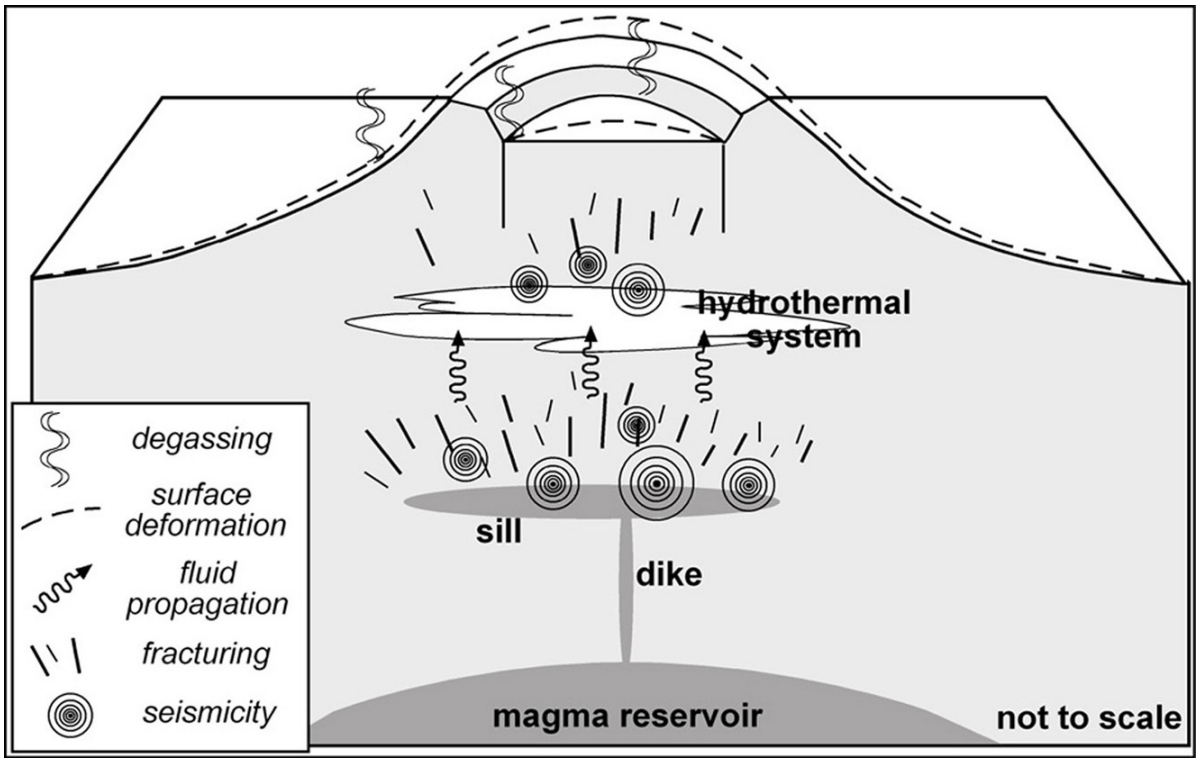

Figure 1.1: Volcanic processes during unrest (from Acocella, 2014).

The interpretation of the source of these geophysical changes often involves modelling techniques. The similarities of volcanic processes, regardless of the volcanoes, allowed the development of models based on physical laws. For example, the study of hydrothermal circulation relies on Darcy's law. However, these models need tuning to each volcano, because each volcano

has its own settings and characteristics (Cashman and Biggs, 2014). In the case of hydrothermal circulation, the outcomes of the model will, for example, depend on the location of the permeable pathways, which depends on the volcano studied. Studying common processes while accounting for the unique behaviour of individual systems has been recently highlighted as one of the main challenges in volcano research (Cashman and Biggs, 2014).

If precursors are characterised in a timely way, they can be used for eruption forecasting. Successful eruption forecasts using seismicity were made for example at Villarica (Ortiz et al., 2003) and Colima (Reyes-Davila and De la Cruz-Reyna, 2002); and proved to be useful for hazard management in the latter case. In contrast, other eruptions occur with limited warning (if any) either because they are preceded by a very short period of precursory activity (e.g., the 2^{nd} May 2008 eruption at Chaiten was preceded by two days of seismicity, Carn et al., 2009) or because the precursory activity is only recognised after the eruption (e.g., the 27^{th} September 2014 at Ontake was preceded by seismicity only interpreted as precursory for the eruption after it occurred, Kato et al., 2015). A careful and timely analysis of the signals with the implementation of automated and tested algorithms are therefore essential for reliable eruption forecasts.

1.3 White Island volcano

1.3.1 Geological setting

White Island volcano is the northernmost active volcano of the Taupo Volcanic Zone (Cole and Lewis, 1981) located ∼50 km off the Bay of Plenty coast of New Zealand (Figure 1.2). It is formed of two overlapping cones: an older eroded western cone and a younger cone that forms most of the island (Black, 1970). Its area of 3.3 km^2 only represents the emergent summit of the much larger White Island Massif (Cole and Nairn, 1975). The volcano is of andesite to dacite composition, and consists of a succession of lava flows, breccias, agglomerates, and unconsolidated beds of ash and tuffs containing lava blocks (Figure 1.3) (Black, 1970; Heap et al., 2015). Main Crater, its main topographical feature, is formed from three subcraters: western, central and eastern (Houghton and Nairn, 1989a; Houghton and Nairn, 1991). These characteristics demonstrate the complexity of the White Island system, and highlight the presence of heterogeneities within the edifice.

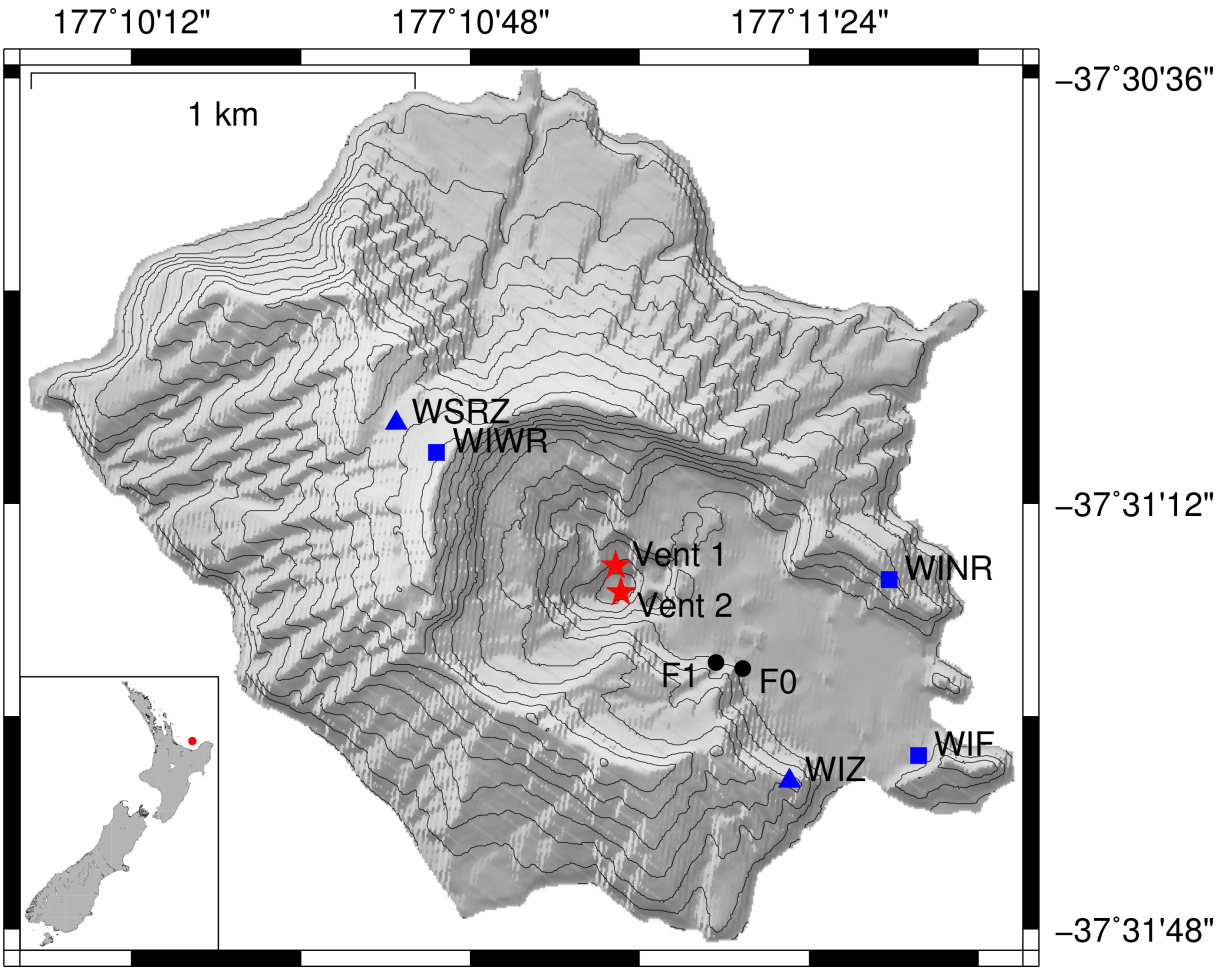

Figure 1.2: Map of White Island volcano showing the location of the main volcanic features during the 2011-2013 unrest: active vents (red stars) and main fumaroles (black dots) and of the monitoring sites: seismic (blue triangles) and webcams (blue squares). During quiescent periods, a crater lake drowns the two vents. The insert indicates the location of White Island (red dot) compared to New Zealand.

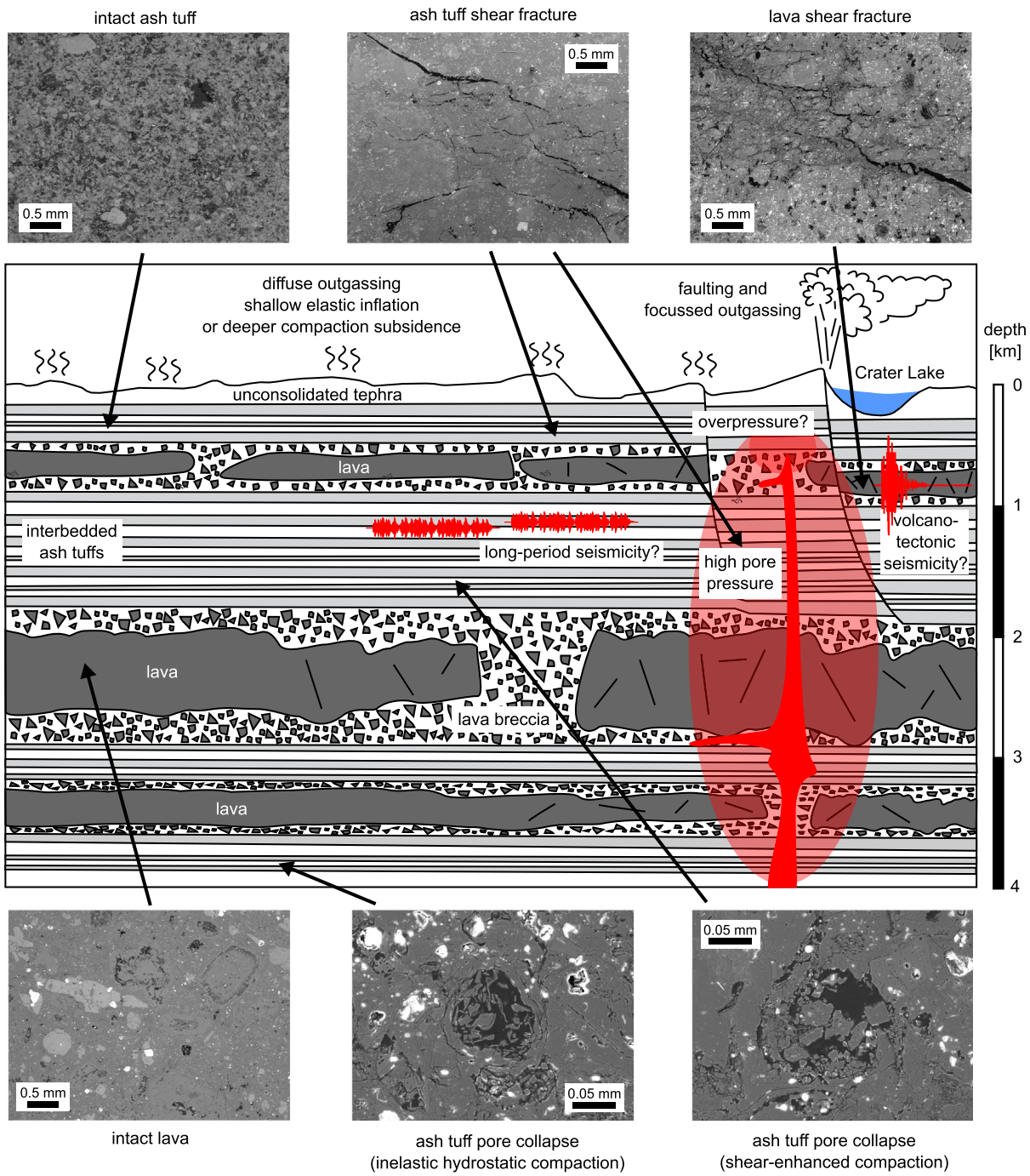

Figure 1.3: Interpretative schematic cross section of White Island volcano (from Heap et al., 2015).

The volcano has a history of long periods of fumarolic and hydrothermal activity, with the major magmatic episode occurring between 1976 and 1980. This activity has also been punctuated by phreatic and phreatomagmatic eruptions (Cole and Nairn, 1975; Nishi et al., 1996) and by strombolian eruptions as in 1979 and 1980 (Houghton and Nairn, 1989a). Another eruptive episode happened in 2000 with ash emissions and seismic tremors and culminated in

an eruption on 27 July 2000, forming a crater in the 1978-90 Crater Complex. Magmas feeding these eruptions are thought to originate from different magma chambers located at 500 m, 1-2 km, 2-7 km depth (Cole et al., 2000; Houghton and Nairn, 1989a and references therein). The last unrest/eruptive episode occurred between 2011 and 2013, was accompanied by geophysical changes (e.g., Chardot et al., 2015) and is the subject of this study.

White Island hosts an active hydrothermal system within Main Crater which has existed for at least 10,000 years (Giggenbach and Glasby, 1977). Steaming ground areas, hot springs, fumaroles and a significant acidic crater lake are the surface expressions of the hydrothermal system. Infiltration of sea water is shown by analysis of subsurface brines and diffuse degassing (Bloomberg et al., 2014); but is absent from the fumarolic output (Giggenbach et al., 2003). Wilson et al. (1995) mentioned that the rocks and sediments at White Island are weathered and hydrothermally altered and Wood (1994) specified that this intense alteration is only present on the crater floor (the main interest of this study), leaving the rocks that comprise the rest of the edifice relatively fresh.

Several attempts have been made to characterise the volcano hydrothermal system. Two Audio-Magnetotelluric surveys were conducted at White Island in 1990 (Ingham, 1992) and 1996 (Nishi et al., 1996) in order to determine the resistivity structure of the volcano. Both studies revealed very low resistivity in the crater floor. Ingham (1992) quantitatively constrained the depth of the top of the hydrothermal system (between 55 and 200 m depth according to the site) whereas Nishi et al., 1996 inferred the presence of clay layers at the surface with shallow sea water intrusion or very conductive hydrothermal water underneath. To constrain fluid circulation within the volcano-hydrothermal system, two self-potential studies were carried out at White Island (Nishi et al., 1996; Hashimoto et al., 2004). Results were consistent with a change in the flow direction due to the crater lake level variations (Hashimoto et al., 2004); and surface features (hot ground, fumaroles). However, the very low resistivity of the ground masks and attenuates most of the signal, limiting the use of self-potential methods at White Island. Thermal infrared mapping (Mongillo and Wood, 1995) and soil temperature measurements (Bloomberg et al., 2014) proved to be useful to detect thermal areas within Main Crater. Some hot zones clearly coincided with thermal features such as fumaroles and springs while others delineated the limit of the eastern subcrater, a zone of microearthquake activity (Nishi et al., 1996). Hot zones were attributed to fractured zones where convective heat transfer occurs from the hydrothermal system while colder more impermeable zones were interpreted as older lake sediments capping this hydrothermal system.

1.3.2 Geophysical and geochemical observables

Volcano monitoring at White Island has been regular since 1967, involving visits to the volcano to conduct various campaign measurements (levelling, magnetics, chemistry sampling, temporary seismic deployment). The first seismic station (WIZ, Figure 1.2) started operating in 1976. Another site was added to the seismic network in March 2012 (WSRZ). This site also has a co-located tiltmeter, gravimeter, GPS station and a webcam continuously recording. Other continuously recording instruments include two MiniDOAS stations for SO_2 emissions, two webcams and a GPS station. This continuous monitoring is complemented by monthly gas flights to measure gas emissions (CO_2, SO_2, H_2S) and by three-monthly visits to measure changes within the crater floor (levelling, CO_2 soil gas emission, fumarole sampling and crater lake/springs sampling). The monitoring programme has been funded by the GeoNet project since 2001. Whenever possible, other measurements complement the monitoring effort. For example, additional gravity and magnetics campaigns were conducted as part of this study.

Observables include various types of seismicity that may or may not be associated to eruptive activity (Latter et al., 1989; Sherburn et al., 1998), deformation within Main crater (Clark and Otway, 1989) and more recently in the fumarole area (Peltier et al., 2009; Fournier and Chardot, 2012), continuous degassing (CO_2 emissions between 250 and $>$ 2000 t day^{-1}, SO_2 emissions between 0 and 400 t day^{-1}, Werner et al., 2008), fumarolic activity, hot springs and a crater lake since 2003.

This integrated monitoring strategy has allowed a better understanding of the White Island system. Werner et al. (2008) observed an annual cyclicity of CO_2 emissions and of the number of low-frequency earthquakes that they attributed to the strain induced by sea level changes on the volcano. The same study highlighted that the volume of magma derived from CO_2 emissions was validated by Cl^- content in the lake so they proposed that gas and magma are transported from deep to shallow levels as a closed system (magma convection), while an open system characterises the upper conduit (Figure 1.4).

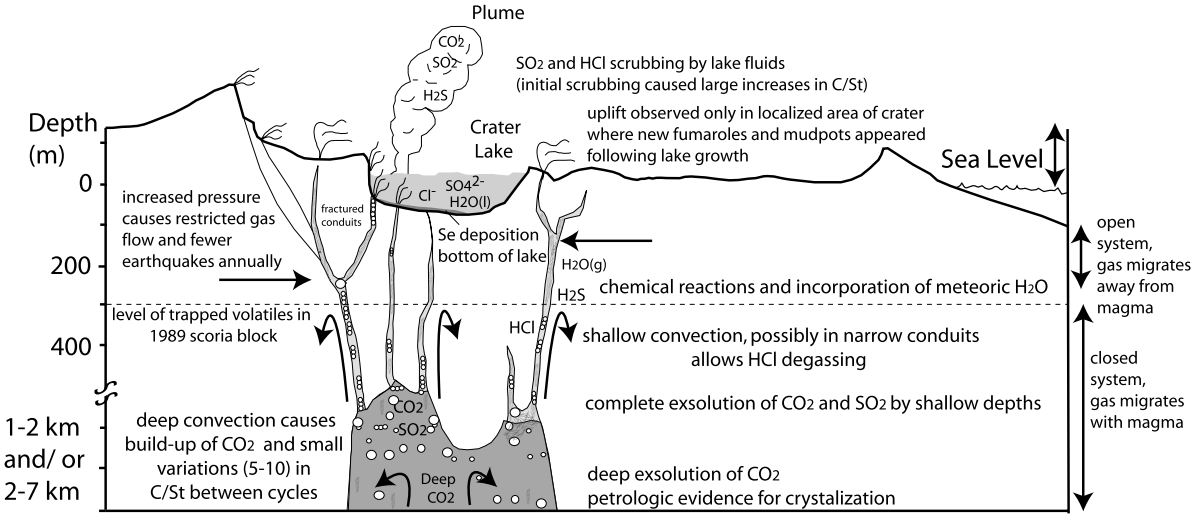

Figure 1.4: Schematic model of White Island crater and conduit system (from Werner et al., 2008).

Several studies emphasised the role of the hydrothermal system in the monitoring observables at White Island. Chemical analyses showed that gas discharges comprise both a magmatic and a hydrothermal component, the latter due to the absorption of magmatic gases in groundwater as a source for the White Island brines (Giggenbach, 1987; Bloomberg et al., 2014). It is also thought that the majority of the earthquakes occurring shallower than 1 km depth are due to variations in pore fluid pressure within the volcano hydrothermal system (Nishi et al., 1996). Magnetic field changes, which mainly reflect heating/cooling effects according to (Hurst et al., 2004); involve the hydrothermal system which heats highly magnetised rocks if shallow magma is present or rapidly cools them via groundwater circulation if the magma retreats. Finally, hydrothermal processes have been proposed to explain ground deformation patterns such as the uplift observed between 2002 and 2008 in the central subcrater (Peltier et al., 2009; Fournier and Chardot, 2012). Recent deformation mainly occurs within the fumarole area, with the maximum deformation off-centre from the fumaroles outlet. Fournier and Chardot (2012) suggested pore pressure changes within the feeding system of the fumaroles as a potential model to explain the uplift. This model implies a non-vertical fumarole conduit. How such a non-vertical fumarole conduit affects hydrothermal circulation and associated geophysical changes is currently unknown. Understanding this effect will help characterise potential unrest observables, and is one objective of this study. This thesis presents the first assessment of the effect of an inclined fumarole on geophysical observables.

Eruptions at White Island have been preceded by increased level of seismicity (Latter et al., 1989); magnetic changes (Hurst et al., 2004) and deformation within main crater (Clark and

Otway, 1989). Changes in these parameters were observed months before the start of eruptive activity. However, magnetic campaigns were interrupted in 2003 because the recorded changes were no longer correlated with volcanic activity. The recent unrest/eruptive episode at the volcano (2011-2013) provides a new case study to investigate unrest signals and eruption precursors. Were the eruptions characterised by signs of elevated unrest? What are the sources of the gravity and magnetic changes recorded during this period? Can the observed geophysical changes inform on the state of the volcano? Finally, can the evolution of volcanic tremor be precursory for eruptions and how can volcanic tremor increases be used for eruption forecasting? All these research questions (Table 1.1) will be addressed in this thesis.

1.4 Towards a better understanding of unrest sources and eruption precursors

1.4.1 Interpreting geophysical changes

Volcano monitoring techniques can record changes in degassing, water chemistry, seismicity, acoustics, deformation, magnetics, gravity and resistivity. In order to characterise the source of these changes, a modelling approach is often undertaken. It consists of retrieving the parameters of the source (e.g., location, size) that best explain the observables, when the source parameters are not immediately self-evident from the observations. For example, surface deformation due to overpressure within a spherical body of rock (at a certain location and with a certain radius) embedded in an elastic media can be calculated from the simple Mogi model (Mogi, 1958). Two types of modelling approaches allow the characterisation of the source of the observables. The forward approach models geophysical changes due to many different sources (each with different parameters) and chooses the source that leads to the geophysical changes closest to the observables. This approach can be time-consuming because of the number of models to be run. Inverse methods present an alternative approach to assess the source of the changes. Usually, a first guess is given for the parameters of the source, and an algorithm will search for the parameters that improve the fit between the modelled and observed signals. This limits the number of models computed and is therefore preferred in many situations where the models are complex. However, despite these efficient techniques, the outcome is rarely a unique and completely characterised source. For example, there is usually uncertainty regarding the nature of the fluids involved (magma or hydrothermal). It is therefore only by integrating other parameters that the nature of the source can be assessed. This can either be done by discussing

the results in light of other changes at the volcano, or by performing coupled inversions (e.g., Anderson and Segall, 2013), which aim at finding the best source of several types of signals at the same time.

The integration of several datasets can bring some valuable insights into the state of the volcano. Chiodini et al. (2015) recently proposed the presence of two overlapping processes to explain the evolution of fumarole composition and deformation at Campi Flegrei: a short–term magmatic fluid injection into the hydrothermal system and a long–term heating of the rock. At Nisyros, the combination of microgravity, seismic, GPS and electromagnetic data showed that the observed short–term gravity changes were likely due to degassing instabilities (Gottsmann et al., 2007). Other case studies of the interpretation of microgravity along with other observables at several volcanoes (Mount Etna, Masaya volcano, Krafla and Askja volcanoes, Tenerife, Campi Flegrei) are summarised in Williams-Jones et al. (2008). Some studies even highlighted some changes precursory to eruptions. For example, the combined analysis of microgravity and deformation can bring some valuable insights into precursory processes within the magma reservoir at large calderas (Williams-Jones and Rymer, 2002). At Kelut volcano, Vandemeulebrouck et al. (2000) observed variations in hydroacoustic noise, seismicity and crater lake temperature prior to the 1990 eruption, that were used to describe pre-eruptive activity. At White Island, magnetic changes and deformation have been explained by thermal changes of a shallow source within the crater, involving the addition of hot hydrothermal fluids during unrest or the inflow of cold fluids when unrest ceases (Hurst and Christoffel, 1973; Hurst et al., 2004).

In this study, I focus on interpreting the source of gravity and magnetic changes using a combination of inverse and forward modelling approaches, and I discuss the results within the wider monitoring observables (Chapter 2).

1.4.2 Numerical modelling of volcano hydrothermal systems

Complex models are needed to capture the range of processes during unrest (e.g., deformation (Hickey and Gottsmann, 2014); gravity (Battaglia and Segall, 2004)) and preceding eruptions (e.g., model comparison in Sahagian (2005)). In a volcanic environment hosting a hydrothermal system, the response of the hydrothermal system to a magmatic input can lead to geophysical observables that are similar to a magmatic signature only (e.g., Todesco and Berrino, 2005; Hurwitz et al., 2007). Better understanding the effect of hydrothermal activity on geophysical observables is therefore of paramount importance to constrain the unrest source. A volcano hydrothermal system represents the complex interface between the magma chamber and the

surface (Norton, 1984). Hydrothermal activity results from several processes whereby hot magmatic fluids escape the magma, propagate through fractures and pores and interact with shallow groundwater (Figure 1.5). Modelling hydrothermal circulation therefore requires the integration of several physical processes. Multiphase fluids (gas, liquid, supercritical) as a function of pressure and temperature, and accounting for the effect of one phase on the other (using relative permeability capillary pressure) need to be considered. Fluids are usually of different nature (water and other magmatic gases) so the effect of solubility of one component within the other also need to be addressed. Finally, hydrothermal circulation involves mass and heat flow (advection, conduction) within a complex domain with varying rock properties. There is therefore the need for solving highly non-linear and coupled equations (Todesco, 2008; Ingebritsen et al., 2010).

To tackle this issue, I use TOUGH2, a multi-component and multiphase simulator describing the coupled flow of heat and mass through a porous medium (Pruess et al., 1999) (Chapter 3).

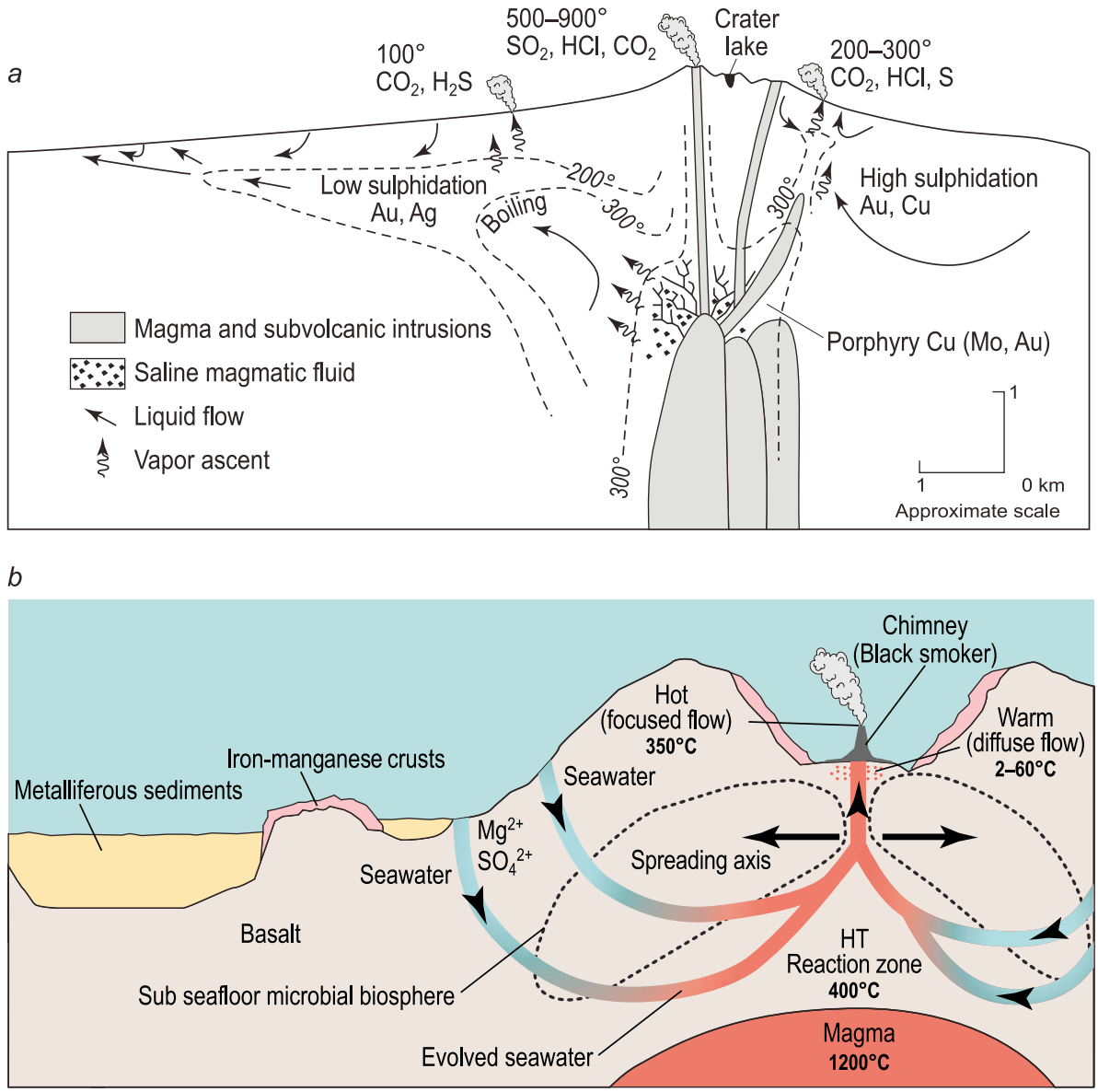

Figure 1.5: Conceptual models of hydrothermal circulation (from Ingebritsen et al., 2010).

Hydrothermal circulation can lead to geophysical observables. For example, changes in fluid composition affect degassing (Chiodini et al., 2003), changes in pressure and temperature affect surface deformation (e.g., Todesco et al., 2004; Hurwitz et al., 2007; Hutnak et al., 2009; Rinaldi et al., 2010; Fournier and Chardot, 2012), changes in density affect gravity (Todesco and Berrino, 2005; Todesco, 2009) and changes in gas saturation and temperature affect electrical conductivity (Rinaldi et al., 2011). Accounting for the effect of hydrothermal circulation has proven to be a reliable model to explain unrest at several volcanoes. For example, Todesco and Berrino (2005) explained the observables at Campi Flegrei (evolution of degassing and gravity) by a varying magmatic input feeding the volcano hydrothermal system (Figure 1.6). Such an

approach could be applied to other volcanic systems. However, the models will need to be volcano-specific because for example, the results strongly depend on the permeability distribution within the domain. There is currently no model of hydrothermal circulation for White Island where geophysical changes occur within the fumarole area.

In this study, I present a TOUGH2 model with parameters consistent for this fumarole area to assess the effect of a fumarole on the geophysical observables (Chapter 3).

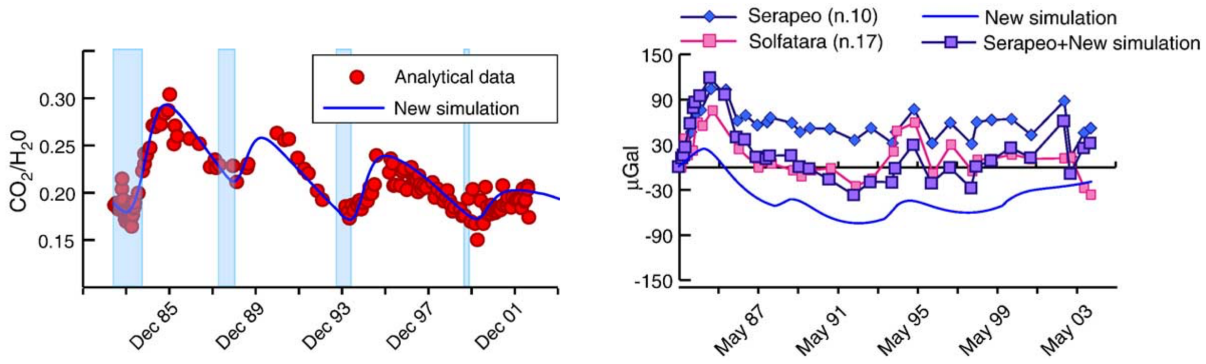

Figure 1.6: Comparison of outputs from TOUGH2 numerical simulations with measured (a) CO_2/H_2O ratios and (b) gravity at Campi Flegrei (from Todesco and Berrino, 2005).

1.4.3 Eruption forecasting

Eruption forecasting is one of the main objectives in volcanology (Sparks, 2003). Successful and reliable forecasts would be a huge step towards improving our ability to mitigate eruption impacts. This challenging task involves 1. identifying and characterising eruption precursors (Tarraga et al., 2008; Carniel et al., 2008) and 2. producing reliable eruption forecasts from the precursory activity. Because of the underlying uncertainties, due for example to the variation in the dataset, these forecasts need to include probabilities (Sparks, 2003). Also, the need for consistency and timely forecasts requires the implementation of automated and reliable algorithms. Several approaches have been developed so far. Bayesian-based approaches (e.g., Bayesian Event Tree (BET) (Marzocchi et al., 2008); Bayesian Belief Network (Hincks et al., 2014; Aspinall and Woo, 2014) integrate a range of observables, models and expert opinions to produce eruption probabilities within a certain period. Geostatistical approaches allow forecasts in space and time but can only be used when a time series of geophysical changes keeps memory of its past so that future activity can be forecast (Carniel et al., 2008). Deterministic methods such as the material Failure Forecast Method (FFM) (Voight, 1988; Cornelius and Voight, 1994) allows the assessment of the timing of the eruption onset but relies on the hypothesis that

an eruption is a case of material failure due to pressurisation of a magma reservoir. Because eruptions at White Island are usually preceded by increased activity, these three approaches could potentially be developed to produce eruption forecasts for the volcano.
In this thesis, I present an automated process to issue eruption forecasts at White Island using volcanic tremor and the FFM presented above (Chapter 4).

1.5 Research questions and thesis organisation

Several objectives were highlighted at the beginning of this chapter (Section 1.1). Answering the research questions presented in Table 1.1 will allow to reach these objectives.

Objective	Question	How this will be addressed	Chapter
Characterise the sources of the gravity and magnetic changes at White Island	What are the source of the magnetic changes associated with the 2011-2013 unrest/eruptive episode?	Acquisition, processing of magnetic data and modelling of the potential sources	Chapter 2
	What is the evolution of gravity changes observed prior to the eruptions?	Acquisition, processing of gravity data and modelling of the potential sources	Chapter 2
	Can the observed geophysical changes inform on the state of the volcano?	Interpretation of the source of the observed changes with other monitoring observables	Chapter 2
Describe the effect of an inclined fumarole on hydrothermal circulation and gravity changes	How does the fumarole inclination affect hydrothermal circulation?	Comparison of results between numerical simulations of hydrothermal circulation with two fumarole inclinations	Chapter 3
	What are the effects of an inclined fumarole on gravity changes at the surface?	Computation of gravity changes from the aforementioned TOUGH2 simulations and comparison of results	Chapter 3

Assess the potential of using volcanic tremor for eruption forecasting at White Island	Can the evolution of volcanic tremor be precursory for eruptions?	Analysis of the goodness-of-fit between the Material Failure Forecast Method and the tremor evolution during the 2011-2013 unrest/eruptive episode	Chapter 4
	How can volcanic tremor increases be used for eruption forecasting?	Implementation of an algorithm to forecast eruptions	Chapter 4
	Can the source of volcanic tremor be reconciled with current models?	Discussion of the source of the volcanic tremor at White Island within the literature context	Chapter 4

Table 1.1: Research questions and how they will be addressed in this study in order to reach the objectives of this thesis.

This thesis is written in manuscript format, with each of the central chapters (Chapter 2 to 4) corresponding to a manuscript that has either been published or is to be submitted. However, care has been taken to ensure this thesis remains a coherent and comprehensive single body of work.

In Chapter 2, I focus on the analysis and interpretation of the magnetic and gravity data associated with the 2011-2013 unrest/eruptive period at White Island. The aim of this chapter is to assess whether these two geophysical techniques depicted the unrest at the volcano. I therefore discuss the potential volcanic source(s) responsible for the evolution of these geophysical parameters and propose an unrest scenario that can explain the data. This chapter will be submitted to Bulletin of Volcanology.

Chapter 3 summarises findings from a numerical modelling analysis which aims at characterising the effect of an inclined fumarole on hydrothermal circulation and gravity changes at the surface. This chapter will contribute to a submission in Geophysics, Geochemistry, Geosystems.

In Chapter 4, I present an eruption forecasting tool which estimates the timing of the eruption onset from increasing levels of volcanic tremor recorded during the 2011-2013 unrest/eruptive episode. This chapter is published in a peer reviewed journal as **Chardot, L.**, Jolly, A. D., Kennedy B.M., Fournier, N., Sherburn, S. 2015. *Journal of Volcanology and Geothermal Research*, 302(C), 11-23, doi:10.1016/j.jvolgeores.2015.06.001.

Preamble

In the introduction chapter of this thesis, I presented the common geophysical changes recorded at White Island during both unrest and eruptive activity. I highlighted that interpreting the source of these changes is challenging because of the potential numerous and complex sources, partly due to the presence of an active volcano hydrothermal system. The need for comprehensive analyses to constrain the source of these geophysical changes was therefore emphasised. Such analyses ideally comprise a modelling approach (forward and/or inverse) allowing a quantification of some of the source parameters. In this chapter, I present magnetic and gravity observables associated with the recent 2011-2013 unrest/eruptive episode at White Island, and analyse the source of the changes using a combination of forward and inverse modelling approaches. I then discuss the source of these changes in the context of other observables during the same period in order to assess the usefulness of magnetic and gravity techniques for unrest characterisation at White Island. This chapter will therefore answer the first three research questions of this thesis (Table 1.1) in order to reach the first objective of this research set in the introduction chapter ("To characterise the source of the gravity and magnetic changes which accompanied the 2011-2013 unrest/eruptive episode at White Island to assess the usefulness of these geophysical techniques for unrest characterisation at the volcano").

Chapter 2

Evolution of magnetic and gravity observables associated with the 2011–2013 unrest/eruptive period at White Island volcano (Whakaari), New Zealand

Abstract

Volcanic unrest typically involves changes in temperature and changes in density/mass at depth that can be recorded with magnetic and gravity measurements. White Island volcano (New Zealand) experienced an unrest period between August 2011 and July 2012, followed by an eruptive period which ended in October 2013. We present magnetic and gravity changes observed at White Island volcano between May 2011 and February 2015 to determine whether magnetic and gravity techniques can be used to characterise volcanic unrest. A decrease in the total magnetic field was observed between May 2011 and March 2012 in a local area close to the active crater, followed by an increase until June 2012. The magnetic field then remained almost constant until February 2015, despite several eruptions in August 2012 and August and October 2013. We measured no significant gravity changes (above the noise level) within the crater floor during the period. We inverted the magnetic anomaly for a dipole, representing a body of rock whose magnetisation changes due to a thermal effect (a 50 °C change between 300 and 600 °C). We found that the best source for the magnetic changes is located in the upper 500 m below the active crater. Our results are consistent with a heating episode between May 2011 and March 2012, followed by cooling between March and June 2012. To constrain the heat source, we then modelled gravity changes due to the

lake and groundwater level decrease and due to an intrusion. Combining modelling results of both the magnetic and gravity changes, we propose that the thermal changes (heating followed by cooling) are due to the rise of hydrothermal fluids from a possible small intrusion. The hot fluids are the likely source of the observed heating episode. They discharged at the surface in May 2012 and likely depressurised the system, allowing the inflow of colder fluids. This model could explain the following inferred cooling episode, even during an unrest phase with increased degassing. The integration of magnetic and gravity data can therefore be a powerful tool to depict signs of volcanic unrest at White Island.

2.1 Introduction

Detecting signs of volcanic unrest is challenging because of the complexity of the recorded signals that stem from different potential sources (e.g. magmatic, hydrothermal, tectonic, anthropogenic). Discriminating these different sources is therefore of paramount importance in order to assess the state of the volcano. We address this issue by focusing on magnetic and gravity changes at White Island volcano.

In volcano-hydrothermal system environments, magmatic and hydrothermal processes can lead to similar geophysical observables. For example, an injection of hot fluids within a hydrothermal system might create the same deformation pattern as a pressure source often associated with a magmatic intrusion (Todesco et al., 2004; Hurwitz et al., 2007; Hutnak et al., 2009; Fournier and Chardot, 2012). Todesco and Berrino (2005) showed that the same situation can occur with changes in gravity and CO_2 passive degassing, i.e., that a magmatic intrusion is not always the only explanation for the observed changes. Hydrothermal activity can lead to geophysical changes of strong amplitude that do not always reflect the volcano state. For example, the volcanic tremor level during geysering activity can be similar to that during eruptive activity (Chardot et al., 2015). The integration of several datasets is therefore recommended to help understand the source of the signals.

Monitoring changes in the total magnetic field and in the gravity field can bring some valuable information about the state of the volcano. Changes in temperature, stress, flow direction, chemistry can lead to magnetic changes (respectively the thermo-magnetic effect (Rikitake and Yokoyama, 1955); piezomagnetic effect (Stacey et al., 1965), electrokinetic effect (Zlotnicki and Le Mouel, 1988) and the effect due to alteration for example (Bouligand et al., 2014)). Slow magnetic changes are usually explained by thermal effect (as the rock magnetisation changes as a function of temperature until the Curie point is reached), whereas rapid changes are generally ascribed to the piezomagnetic or electrokinetic effect (Hurst et al., 2004). Changes in mass and/or density affect gravity. The combined interpretation of microgravity and deformation

measurements can inform on the potential emplacement of an intrusion and on the effect of hydrothermal activity (e.g., Rymer, 1996; Gottsmann et al., 2005; Williams-Jones et al., 2008; Zurek et al., 2012).

White Island volcano (New Zealand, Figure 2.1) is a case in point where interactions between magma and the volcano–hydrothermal system lead to a variety of geophysical signals. This hydrothermal system has existed for at least 10,000 years (Giggenbach and Glasby, 1977). Its effect on deformation has been highlighted by Peltier et al. (2009) and Fournier and Chardot (2012). Magnetic measurements were performed regularly and showed some correlation with the volcano activity until 2003 (Christoffel, 1989; Hurst et al., 2004). The source of the observed changes was ascribed to thermal effects whereby hydrothermal fluids heat the medium during unrest and meteoric water cools it during quiescence. However, whether microgravity can inform on the volcano state has never been tested extensively at White Island.

In this study, we focus on assessing whether magnetic and gravity campaign measurements can detect unrest at White Island. We present results from 5 magnetic and 3 gravity campaigns completed between May 2011 and February 2015 on the White Island crater floor and assess the potential source(s) for the observed changes. We first give an overview of the volcano activity during the period of interest. We then present our processing procedure and the observed magnetic and gravity changes during this period. Finally, we discuss the source(s) of the changes by using a holistic modelling approach and propose a scenario for the period preceding the eruptive phase.

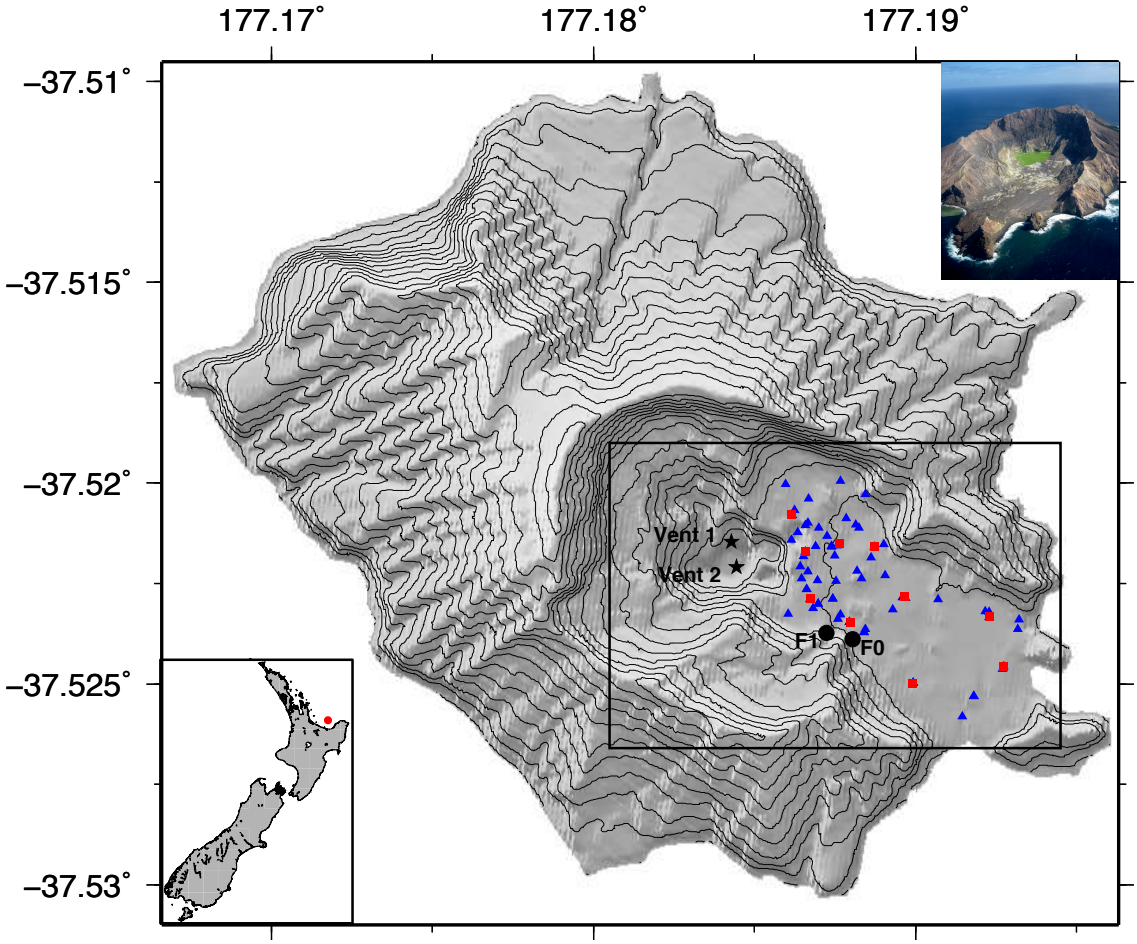

Figure 2.1: Map of White Island volcano showing the features of interest for this study: active vents between August 2012 and October 2013 (black stars), most active fumaroles (black circles), magnetic pegs (blue triangles), gravity tiles (red squares). The box indicates the crater area that will be plotted in the following figures. The location of the island relative to New Zealand is shown in the bottom left corner insert. The picture in the top right corner shows the volcano during quiescence (2010).

2.2 White Island activity: May 2011 - February 2015

After more than 10 years of relatively minor hydrothermal activity, White Island volcano entered a new phase of unrest in August 2011, which started with a period of elevated tremor. Between August 2011 and November 2013, the volcano activity oscillated between periods of high energy release with elevated tremor and low crater lake level, and periods of lower energy release with lower tremor activity and a higher crater lake level. This period was punctuated by several eruptions and the different phases are illustrated by Figure 2.2. The crater lake level

first decreased between August 2011 and July 2012. The tremor level and the SO_2 emission increased from May 2012, while the CO_2 emission remained within background during the whole period (measured in the plume during monthly gas flights and emitted from the soil during the 3-monthly soil gas surveys). Chemical measurement at the main fumarole of the volcano indicates a CO_2 pulse and a heating period during December 2011–June 2012 and December 2011–December 2012 respectively (increasing CO_2/H_2O ratio and R_{CO}) (Bruce Christenson, pers. comm., June 2013). A 5–m lake level increase accompanied a strong tremor episode on 27 July 2012, and marked the start of a more active period. The first eruption of this period occurred on 4 August 2012 from Vent 1 (Figures 2.1 and 2.2) and contained some juvenile material (Kilgour G., pers. comm., 2013). The tremor level stayed elevated with varying amplitudes until April 2013, while the surface changes evolved from mud eruptions in September 2012 and a dome building event in November 2012 from Vent 1, to geysering between January and March 2013 from Vent 2 (Figures 2.1 and 2.2). The lower tremor level between April and July 2013 accompanied a crater lake level increase. Another more active period started in July 2013 and was characterised by several strong tremor periods and eruptions on 19 August and 4, 8 and 11 October. The ejecta from the October eruptions again suggest that juvenile material was involved (Kilgour G., pers. comm., 2013). Between November 2013 and February 2015, the tremor level decreased and the crater lake level slowly increased again, marking the end of the unrest episode. Volcanic activity and associated geophysical observables during the period August 2011 - February 2015 are summarised on Figure 2.3.

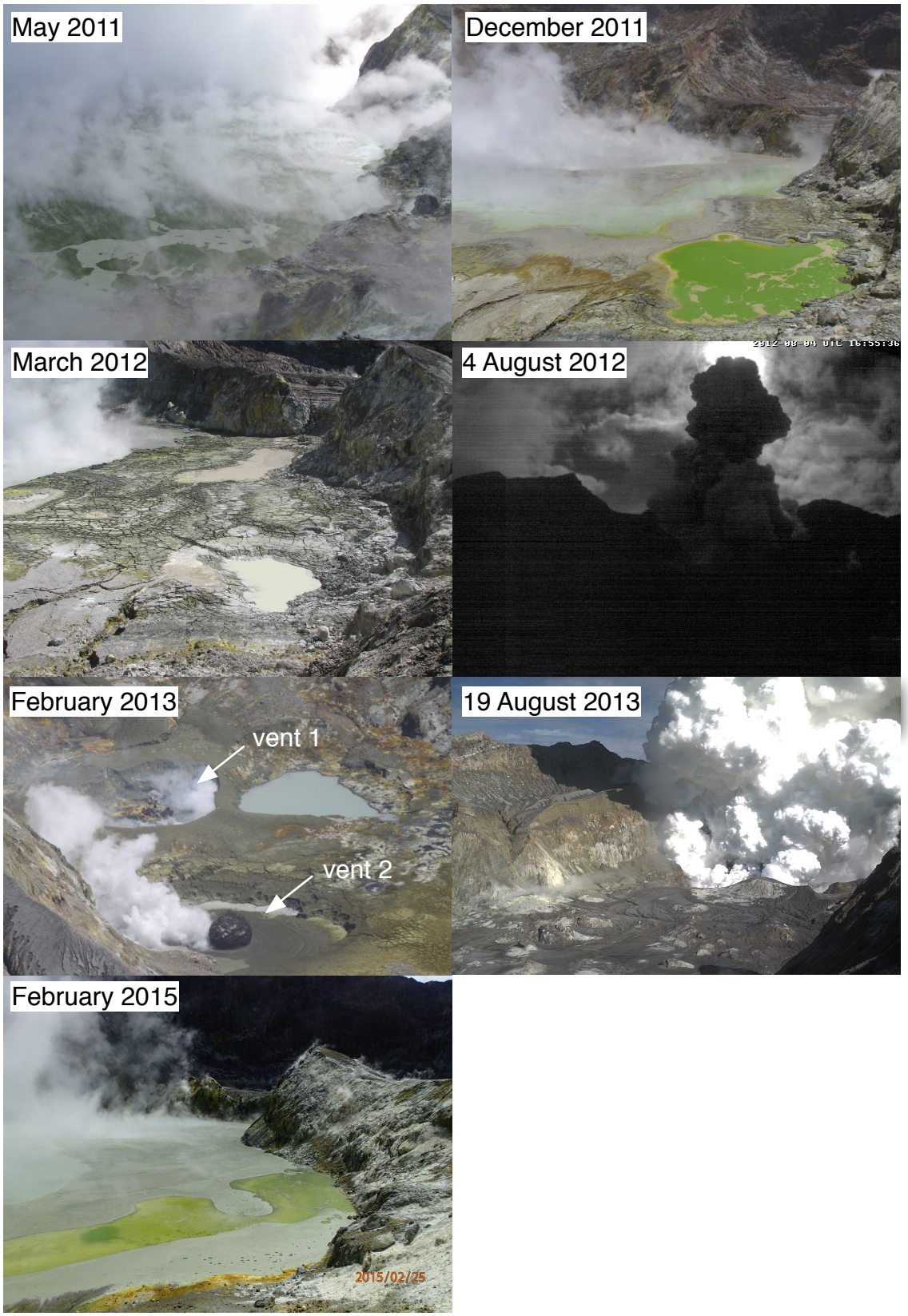

Figure 2.2: Pictures showing the different phases of the volcano activity between May 2011 and February 2015. Photos credits: Karen Britten and Brad Scott, GNS Science/EQC.

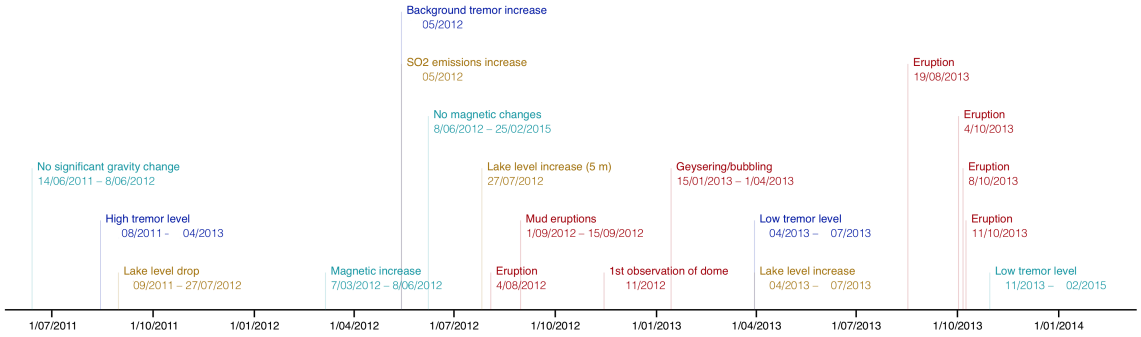

Figure 2.3: Volcanic activity and geophysical observables between August 2011 and February 2015. The colours represent: magnetic and gravity changes (light blue), seismic activity (dark blue), observed hydrothermal changes (brown), eruptive activity (red).)

2.3 Data acquisition and processing

2.3.1 Magnetic surveys

Five magnetic surveys were completed within the White Island volcano crater floor on 24 May 2011, 7 March 2012, 8 June 2012, 11 October 2012 and 25 February 2015. Data were collected at approximately 70 pegs (more pegs were added through time; Figure 2.1) with a GSM–19 magnetometer for the first four surveys, and with a GEM-856 for the last survey. Both instruments recorded the intensity of the total magnetic field, with the sensor mounted on a 2.4 m staff. At each site, we measured the magnetic field several times until the value became stable. The last survey was completed after the eruptive sequence which buried some of the pegs, leading to a smaller coverage.

To investigate the magnetic changes of volcanic origin, variations of the total magnetic field of all the other origins needs to be removed. The different processing steps are shown on Figure 2.4. We first removed the short-term variations (syn–survey) mainly dominated by diurnal variations (whereby the sun ionises the atmosphere and modifies the currents in the ionosphere) and by magnetic storms. We corrected each survey data for these diurnal variations using continuous total magnetic field measurements acquired: at the Eyrewell observatory close to Christchurch (NZ, $\sim$ 770 km south-west from White Island) for the first three campaigns and at a local base station that we installed on the north-eastern part of the crater floor during the last two surveys. Diurnal variations were usually of $\sim$ 15 nT at Eyrewell for our survey periods. They are of higher amplitude when measured locally ($\sim$ 40 nT). The maximum difference between the total

magnetic field recorded at these two sites was ∼30 nT for the only survey when they were both operating (second to last survey). The local base station likely records similar diurnal magnetic field variations as observed at the repeated sites. This implies that an additional error (30 nT to be conservative) is considered for each measurement of the first three surveys when the Eyrewell station was used for diurnal corrections. No magnetic storms occurred during our survey. We then corrected for the longer-term variations of the magnetic field (between surveys), mainly due to variations in the Earth interior that affect the magnetic field inclination, declination and intensity (secular changes). We assumed that a reference site located on the eastern part of the crater is not affected by volcanic processes and only records the Earth's total magnetic field. The magnetic change between one survey and the next will therefore only represent the secular changes. By computing each survey relative to this reference site, we therefore correct for the secular changes.

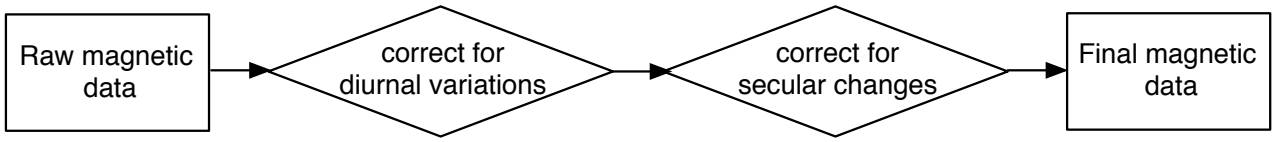

Figure 2.4: Flowchart of the different processing steps performed on the magnetic data.

To analyse the magnetic changes of volcanic origin between two surveys, we finally substracted the magnetic value of each site of the later survey from the magnetic values of the previous survey.

2.3.2 Microgravity surveys

Three gravity surveys were completed on 14 June 2011, 21 December 2011 and 8 June 2012 on the White Island crater floor. Data were collected at the centre of 10 fixed concrete tiles (Figure 2.1) with a Lacoste & Romberg G-meter for the first survey and with a Lacoste & Romberg D-meter for the last two surveys. Measurements at each site were repeated several times during each survey to quantify the instrument drift. Data were corrected for Earth tides and ocean loading (using a continuous gravitymeter located on the island whose characteristics are summarised in Jolly et al., 2013; Appendix A) and for the instrument drift. Because the area studied is small, we did not apply a latitude correction. We did not account for the effect of a varying atmospheric pressure that we consider negligible. The processing steps are shown

on Figure 2.5. Finally, we computed the gravity of each site relative to a reference site.
The coverage of the December 2011 survey is smaller than the others (7 sites instead of 10) because an earthquake occurred during the December survey (Mw 5.2 at 10 km depth in Kermadec Islands (USGS website)). We interrupted the survey until the surface waves no longer affected the readings and discarded the readings acquired within the loop affected by the earthquake.

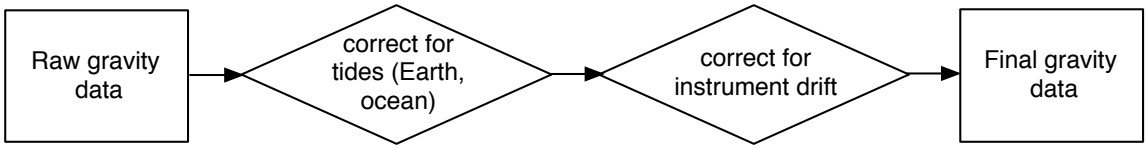

Figure 2.5: Flowchart of the different processing steps performed on the gravity data.

To analyse the gravity changes between two surveys, we removed the gravity value of each site of the later survey to the gravity values of the previous survey. We finally corrected for the effect of elevation changes between surveys using levelling data acquired within a few days of each survey (20 May 2011, 6 December 2011, 11 June 2012), at pegs within 20 metres of each gravity tile. The June 2012 did not close as indicated by the first measurement point being discrepant from the final measurement point. Hence, this survey was discarded for this study. Deformation for June 2012 was obtained by interpolating linearly the deformation observed between March and August 2012. Caution was therefore used when analysing the gravity changes relative to June 2012.

2.4 Results

2.4.1 Magnetic data

2.4.1.1 Survey data

The corrected magnetic data of each survey are presented on Figure 2.6; relative to a site on the eastern part of the crater floor (red triangle). Raw and corrected data are given in Appendix B.1. The error on each survey is estimated to be ∼15 nT so we will not interpret changes below an amplitude of 30 nT. The magnetic field presents some spatial anomalies close to the active crater, whereas the variations are small on the rest the of the crater floor. The first survey indicates the presence of a positive anomaly (A) (maximum amplitude of 1100 nT) of ∼100 m

diameter on the east edge of the active crater, and of a larger negative anomaly (B) of smaller amplitude (maximum ∼360 nT) south-east of the first. During the second survey (March 2012), we repeated measurements at the same pegs and added a few more between these two anomalies to better constrain their location. The previously observed anomalies are still present and the additional pegs allow the location of another positive anomaly (C) (of higher amplitude, ∼1300 nT) between these two anomalies. The same anomalies are observed for the subsequent surveys (June and October 2012 and February 2015), with the first positive anomaly decreasing in amplitude with time. For this last survey, the data acquired on the two pegs in the north-eastern part of the crater floor were discarded for the subsequent analysis because they showed a very strong and local magnetic decrease that we consider as outliers. The near crater anomaly (C) is similar to an earlier anomaly identified by Woodward and Mumme (1993) and may be related to that that earlier feature.

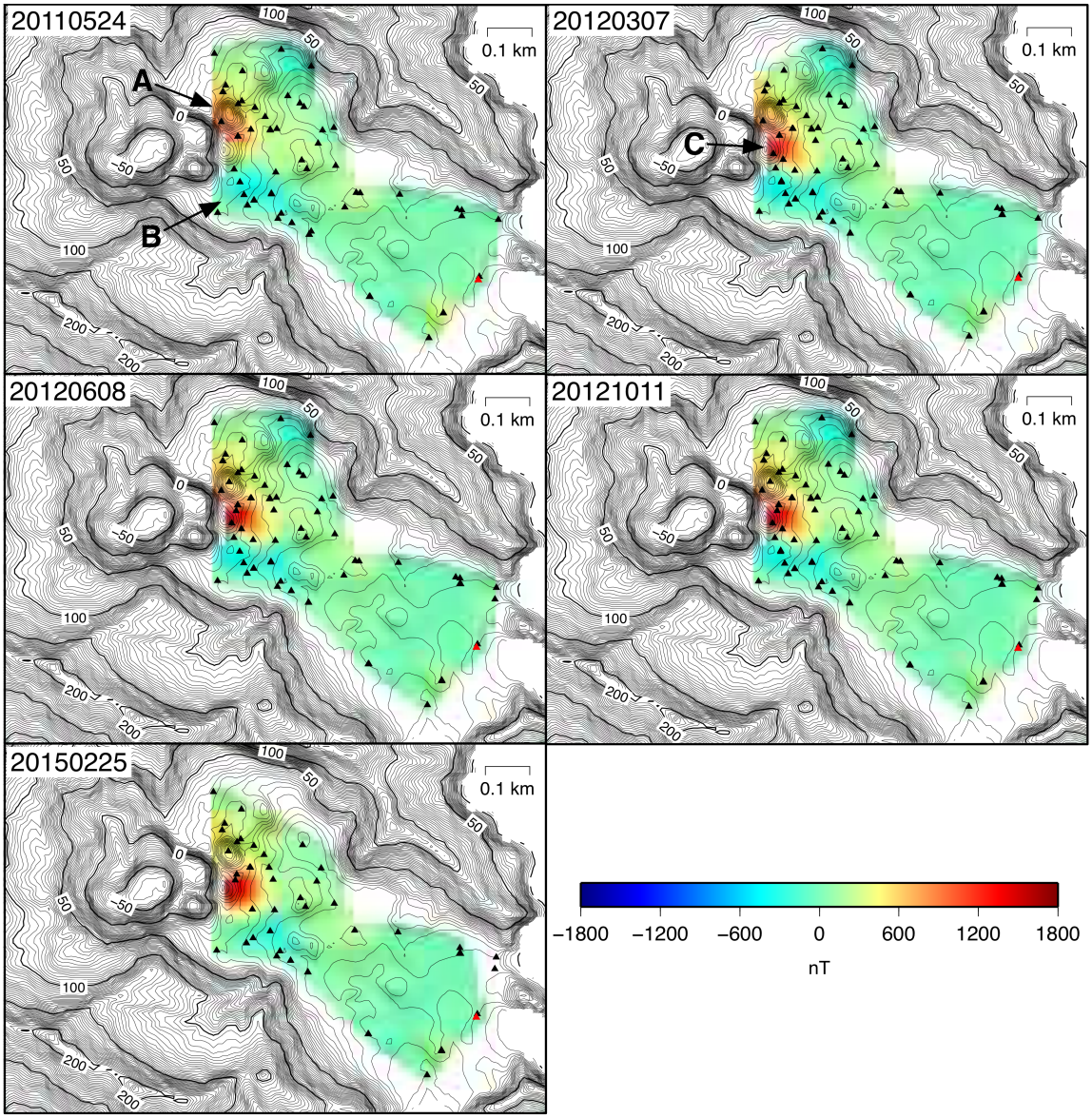

Figure 2.6: Corrected magnetic data (in nT, colour) for each survey on top of the White Island topography (in m, contours) (see Figure 2.1 for the coordinates of the area). If the distance between the sites was less than 5 m, the magnetic value at each was considered to be the average of the two individual measurements. This procedure yields smooth spatial variations as an aide to plotting. Magnetic changes computed at each site were then interpolated on a 10–m grid. The triangles are the location of the measured magnetic sites for each survey, the red triangle shows the reference site.

2.4.1.2 Magnetic changes

The magnetic changes observed between the five surveys are presented in Figure 2.7. Changes on the eastern side of the crater floor are close to 0 nT which confirms that the secular changes were appropriately removed. We observe no significant (i.e., above noise) magnetic changes on the whole crater floor, apart from the anomaly located in the central subcrater (north-east of the active crater) between May 2011 and June 2012. This anomaly is characterised by a magnetic decrease (between May 2011 and March 2012) followed by a magnetic increase (between March and June 2012). The maximum amplitude of the decrease (70 nT) is slightly higher than that of the increase (50 nT) but this is within our error estimate so the amplitude difference is considered as insignificant.

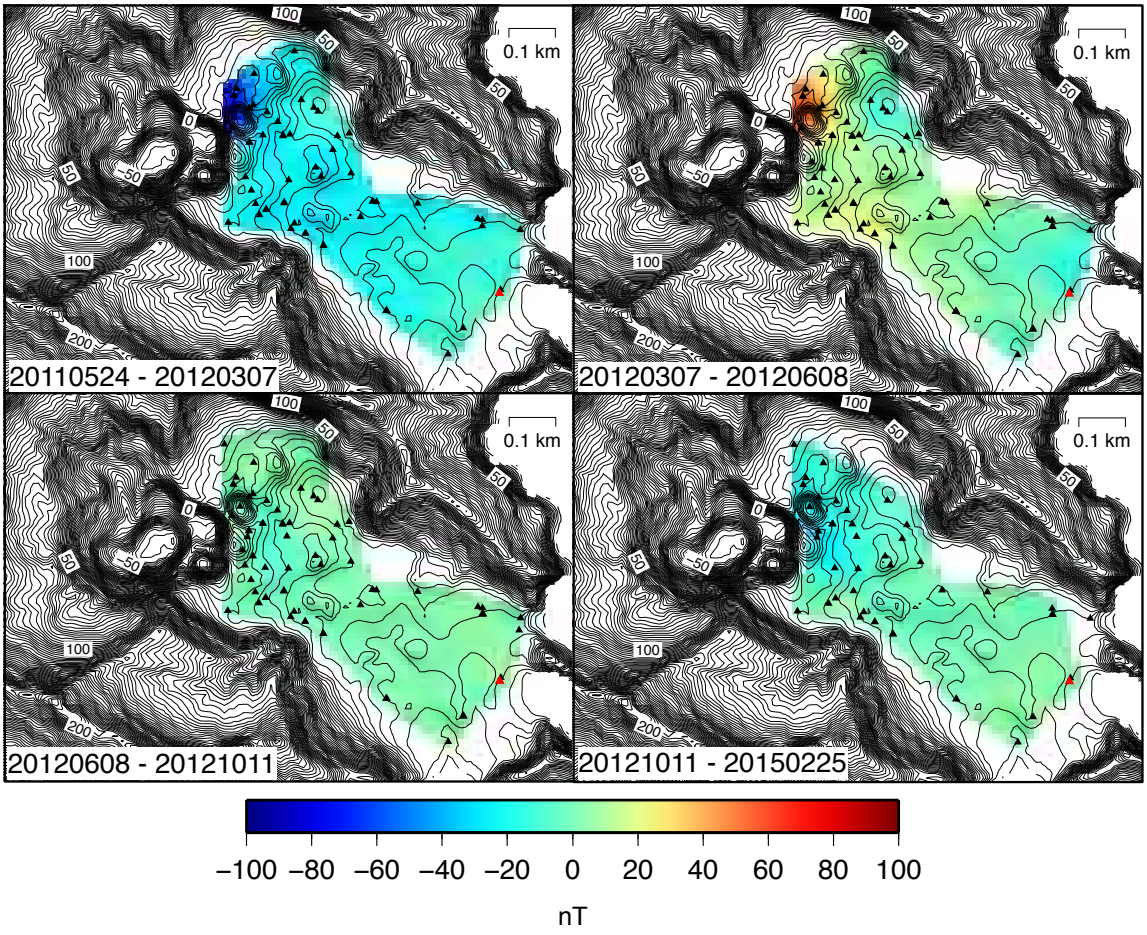

Figure 2.7: Magnetic changes observed between each survey (in nT, colour) on top of the White Island topography (in m, contours) (see Figure 2.1 for the coordinates of the area). If the distance between the sites was less than 5 m, the magnetic value at each was considered to be the average of the two individual measurements. This procedure yields smooth spatial variations as an aide to plotting. Magnetic changes computed at each site were then interpolated on a 10–m grid. The triangles are the location of the measured magnetic sites for each survey, the red triangle shows the reference site.

2.4.2 Gravity data

2.4.2.1 Survey data

Gravity data acquired on June and December 2011 and on June 2012 are presented on Figure 2.8; relative to the southeast site of the White Island crater floor (see raw and corrected data in Appendix B.2). The three surveys present the same pattern: the gravity decreases closer to the active crater with a minimum of ∼4 mGal at the north-westernmost site, relative to the

reference site.

The first survey (June 2011) was the most comprehensive and allows the assessment of the error/uncertainties in the measurements at some sites. The closest site to the north crater wall presents variations of 25 μGal around the averaged gravity value. The other sites have variations of 15 μGal around their mean values. The site located between the fumarole and the crater lake (GR03) also presents some strong short-term variations during the December 2011 survey: a difference of $\sim$120 μGal is recorded between the morning and the afternoon measurements. We can not exclude a reading error but this difference could also be due to short-term volcanic processes (Gottsmann et al., 2005; Gottsmann et al., 2007; Williams-Jones et al., 2008), possibly related to the earthquake that occurred between the two measurements. In the subsequent analysis, we therefore used the measurement acquired before the earthquake, and considered a large error (+/-120 μGal) at this site.

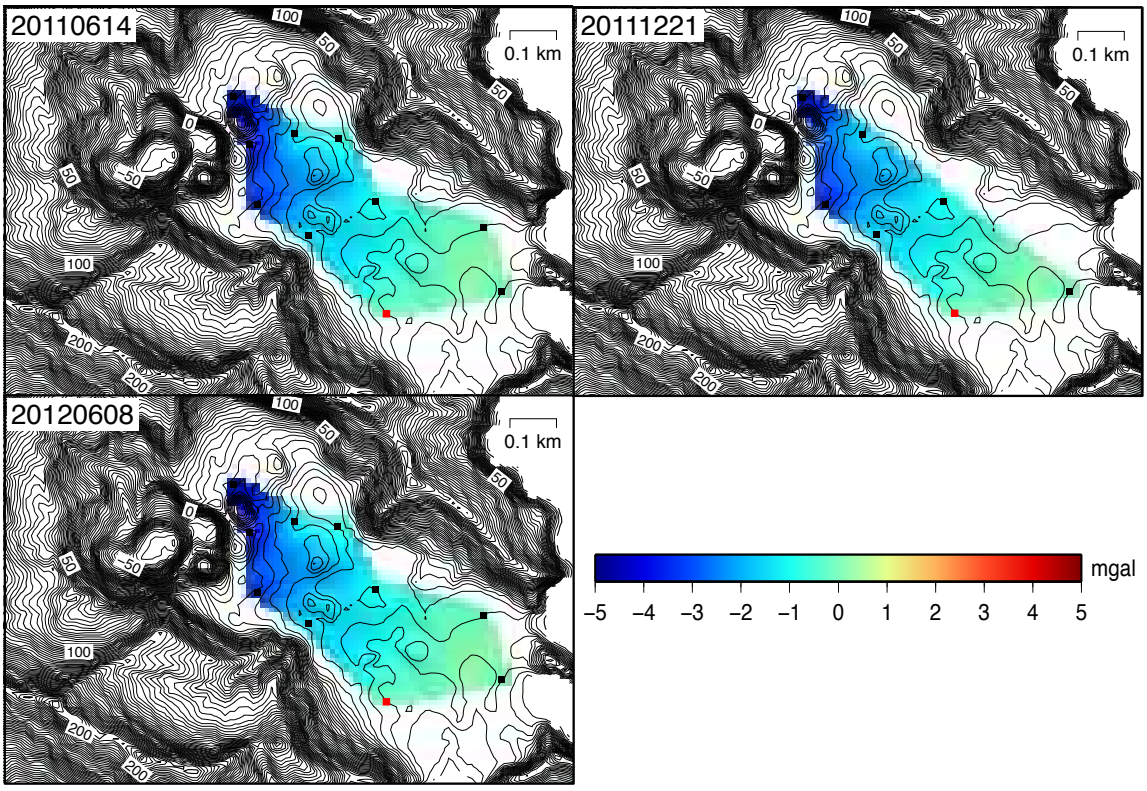

Figure 2.8: Corrected gravity data (in mGal, color) for each survey (interpolated on a 10–m grid) on top of the White Island topography (in m, contours) (see Figure 2.1 for the coordinates of the area). The squares are the locations of the measured gravity sites for each survey, the red square shows the reference site.

2.4.2.2 Gravity changes

The gravity changes observed between the three surveys are presented in Figure 2.9. Overall, we observe gravity changes within 30 μGal at all the sites of the crater floor but three: the site between the fumarole area and the crater lake (GR03), the westernmost site (GR04) and the closest tile to the north crater wall (GR07). However, given our error estimate previously defined (+/-120, 25 and 15 μGal for GR03, GR07 and GR04, respectively), the only noticeable gravity change is measured at site GR04 and shows a gravity decrease (-47 μGal) between June 2011 and June 2012.

Ground deformation occurred during this period (Figure 2.9), and its contribution to the gravity changes needs to be removed. A general subsidence centred on the fumarole area occurred between June 2011 and December 2011, followed by a mixed pattern of uplift/subsidence between December 2011 and June 2012, with subsidence in the fumarole area and uplift at several sites including GR04. Although the free-air gradient may vary due to terrain effects and Bouguer anomalies (Rymer, 1996; Williams-Jones et al., 2003), we consistently used the common value of 0.3086 μGal mm^{-1} to correct the gravity changes from elevation changes. After this correction, the gravity changes at most of the sites are within error apart from GR04 which still shows a gravity decrease of 43 μGal between June 2011 and June 2012. However, due to our estimate of the levelling data from interpolation between other surveys, we do not consider this gravity change as significant. Overall, due in part to our large error estimate on the gravity sites, we measured no significant gravity changes over the White Island crater floor between June 2011 and June 2012. This implies that either no gravity changes occurred, or if they did occur, were of the same amplitude at all the sites.

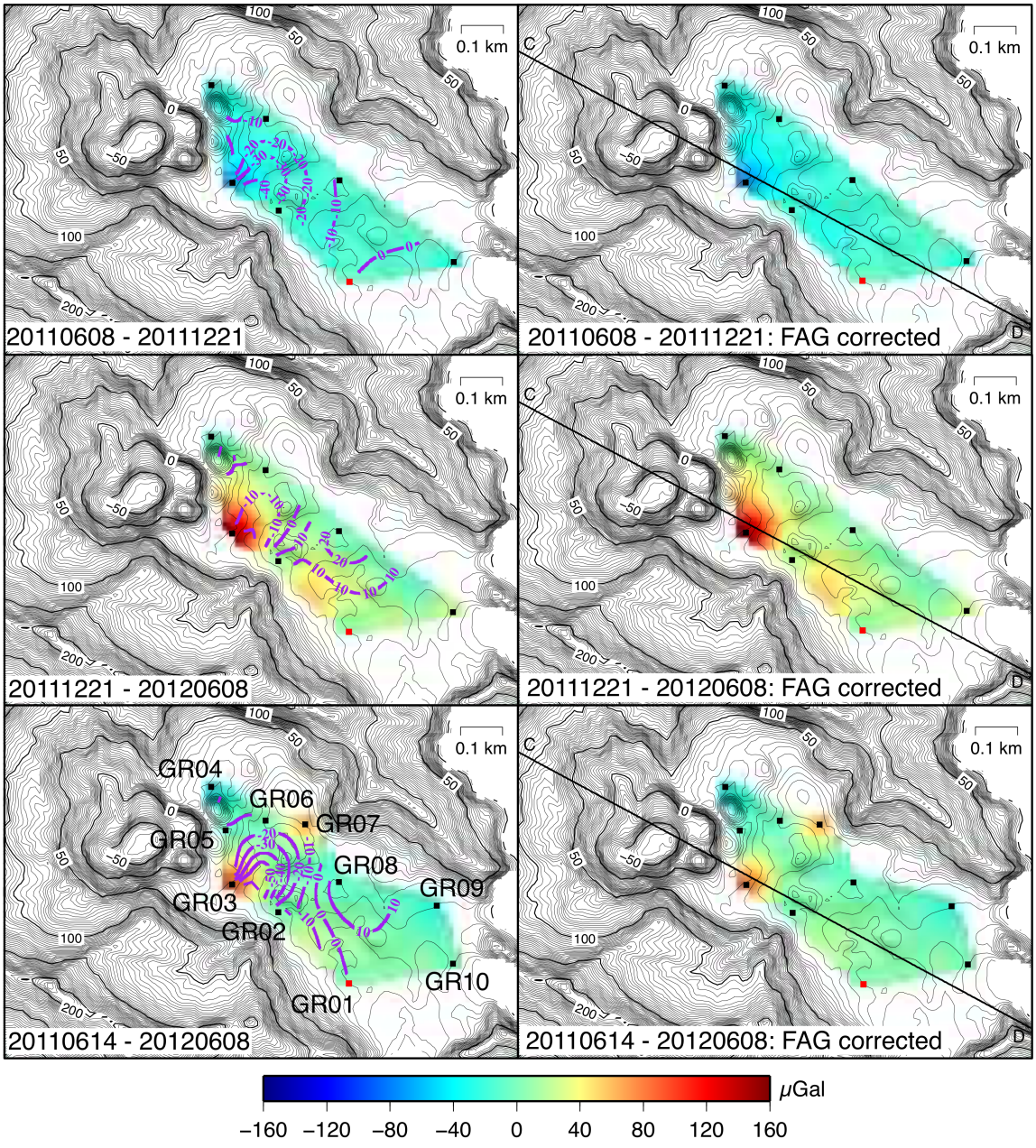

Figure 2.9: Gravity changes observed between each survey (in μGal interpolated on a 10–m grid, colour) on top of the White Island topography (in m, contours) (see Figure 2.1 for the coordinates of the area). The left panels show gravity changes (in μGal, colour) and levelling changes (in mm, purple contours), the right panels show gravity changes corrected for elevation changes using the levelling data and a free-air gradient coefficient of 0.3086 μGal mm^{-1}. The forward gravity modelling will be performed on profile C–D.

2.5 Discussion

2.5.1 Inversion of the magnetic anomaly for a dipole source

The observed magnetic anomaly is close to the edge of our network and observed on ∼10 sites. Previous studies suggested that changes of this order of magnitude are likely to be related to thermal effects (Hurst and Christoffel, 1973; Christoffel, 1989; Hurst et al., 2004). Heating would cause a demagnetisation of the rock which loses its magnetic properties until the Curie point (which depends on the mineral assemblage) is reached. At this temperature, the rock entirely loses its inherent magnetic properties. This process is reversible, so if cooling occurs, the rock regains its magnetic properties and becomes remagnetised. If this process occurs in a spherical body of rock, the magnetic changes due to thermal effects in this sphere can be approximated by a dipole.

2.5.1.1 Magnetic field due to a dipole

Magnetic field changes (nT) due to a dipole were computed using parameters representative for White Island volcano (see Appendix C for the formulation). The Earth magnetic field has a declination of 20.1° (to true north) and an inclination of -62.87° (to horizontal, the negative sign indicates that magnetic field points upwards). The magnetisation of the source is 0.7 A m^{-1} (Hurst and Christoffel, 1973) which corresponds to a temperature change of ∼50 °C between 300 and 600 °C (Figure 2.10). This source of magnetisation has the same orientation as the Earth magnetic field but the sign of the inclination is positive if we consider demagnetisation (i.e. heating). We use a rock susceptibility of 1×10^{-2} (SI unit), which is the average value used in Hurst et al. (2004).

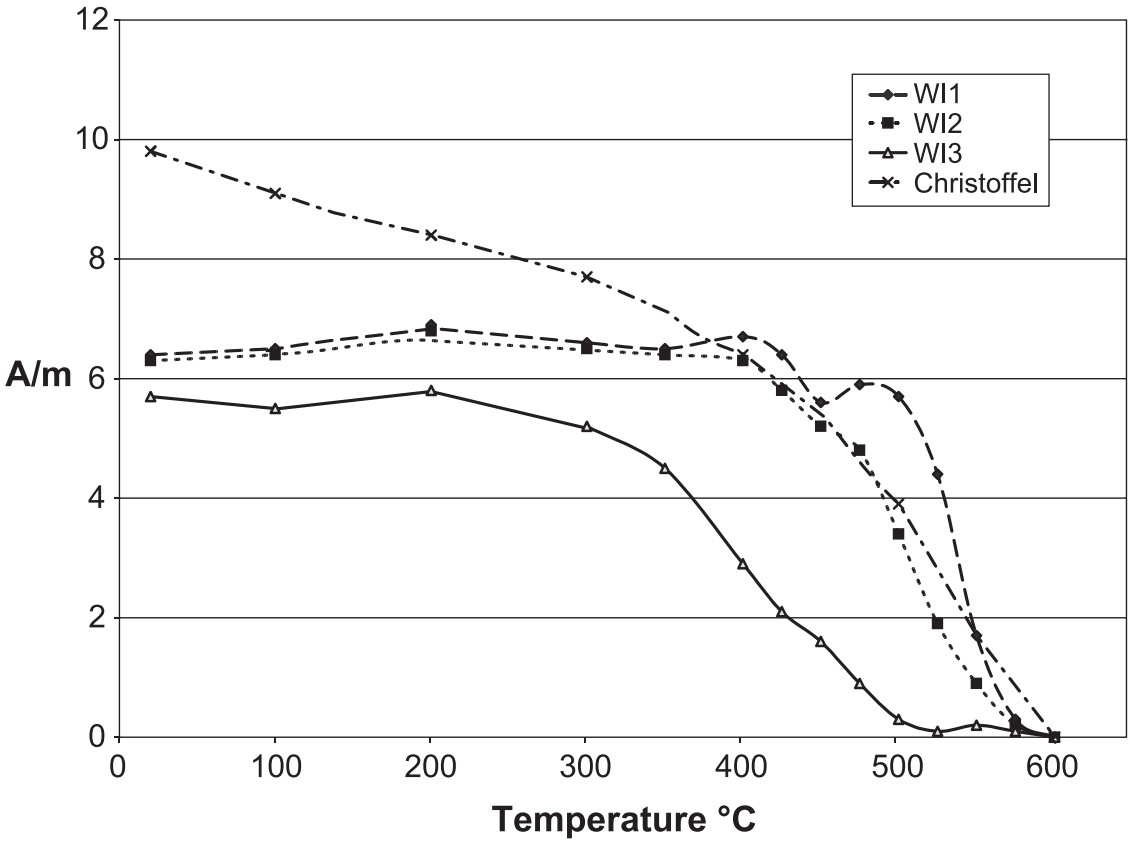

Figure 2.10: Thermal demagnetisation curves for several White Island samples (from Hurst et al., 2004).

Figure 2.11 shows an example of the magnetic anomaly at the surface (map view and South-North profile) created by a spherical volume of magnetisation of radius = 30 m placed in x = 0 m (East), y = 0 m (True North), z = 60 m (depth), being demagnetised (Figure 2.11a and b) and remagnetised (Figure 2.11c and d). This is consistent with previous results (Hurst and Christoffel, 1973; Christoffel, 1989; Hurst et al., 2004): a demagnetisation creates a magnetic decrease to the north-east of the source while a remagnetisation creates a magnetic increase at this same location.

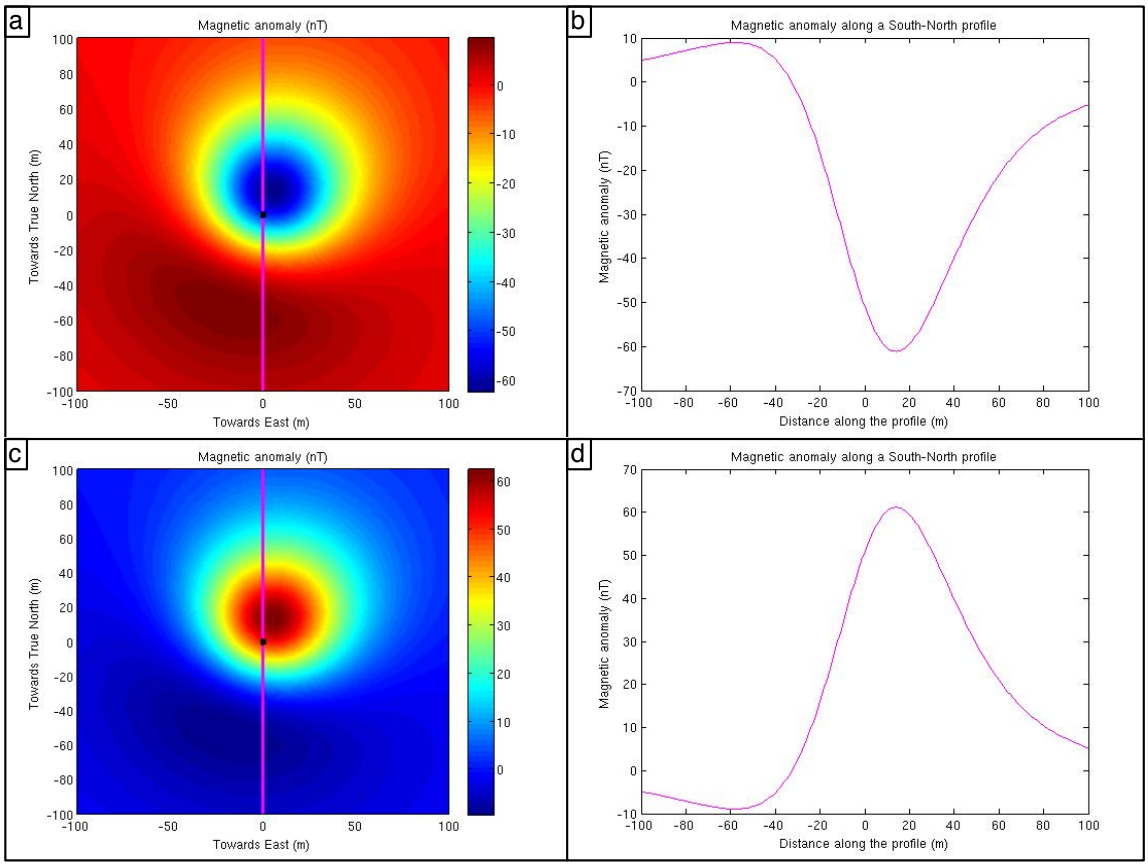

Figure 2.11: Results from forward modelling of thermal changes in a spherical source (30 m radius, located at (0,0) and 60 m deep): a. Map view of magnetic anomaly when demagnetisation of the spherical source. The black dot indicates the source location, and the pink line the location of the profile on panel b.; b. South-North profile when demagnetisation of the spherical source; c. Map view of magnetic anomaly when remagnetisation of the spherical source: The black dot indicates the source location, and the pink line the location of the profile on panel d.; d. South-North profile when remagnetisation of the spherical source

Heating of a spherical body of rock causes magnetic changes similar in magnitude and spatial extent to those observed between May 2011 and March 2012: magnetic field decrease N-E of the crater (maximum amplitude of about -60 nT) and small magnetic changes elsewhere (Figure 2.7). Additionally, cooling of this body of rock leads to magnetic changes similar in magnitude and spatial extent to those observed between March and June 2012: magnetic field increase N-E of the crater (maximum amplitude of about 60 nT) and small magnetic changes elsewhere. These forward models suggest that a dipole source is an appropriate model to explain the magnetic changes observed at White Island between May 2011 and June 2012.

2.5.1.2 The simulated annealing inversion method

We inverted the observed magnetic changes to find the best source explaining these changes. We chose the simulated annealing algorithm to solve the inverse problem because: 1. it samples the whole model space (to avoid getting stuck in local minima) and 2. it uses the shape of the error to direct the search of the solution sequence. It is based on the physical annealing of metals where the atom's motion becomes restricted as the temperature decreases. A parameter T (analog to the temperature) controls the size of the space where the search occurs. Starting from an initial guess, a solution is accepted if the error (E_2) (E is analog to energy) is smaller than the error of the previous solution (E_1). If the error is higher than the previous one, the solution is also accepted if t, defined as:

$$t = exp\left(-\frac{E_2 - E_1}{T}\right) \tag{2.1}$$

is higher than a random number between 0 and 1. When T is high, t is close to 1 so the new solution is almost always accepted which allows sampling of the whole space. Conversely, when T is small, t is close to 0 so the new solution is almost never accepted which implies that the new solution is accepted only if its error is smaller than the previous one.

The Matlab code from Menke (2012) was adapted to our problem. The dipole modelling code described in Appendix C was used as a forward model with the error defined as the difference between the modelled and the observed magnetic changes at the different sites. We set a high number of iterations to 1,000,000 and ran each inversion with two different initial guesses (for the source location and radius) to increase our chance to find the global solution and not a local minimum.

2.5.1.3 Application to the observed magnetic changes

Several inversions of the observed magnetic changes (May 2011–March 2012, March 2012–June 2012) were run in order to find the best dipole source explaining these changes and the results are presented in Table 2.1. The inversions were run with two different initial guesses (1) x=0 m, y=0 m, z=-250 m, r=150 m and (2) x=100 m, y=100 m, z=-350 m, r=250 m where (x=0, y=0, z=0) defines the centre of the active crater. We fixed the Earth and dipole magnetic field orientation (inclination = -62.87, declination = 20.1), the source magnetisation (0.7 A m^{-1}), the rock susceptibility (1×10^{-2} SI unit) and inverted for the source location (latitude, longitude, depth) and radius. Given that the magnetic changes were observed at more than 4 sites, our problem is over-determined.

We first inverted for the best source explaining the changes observed over the whole crater floor for both periods. The best source is not well-constrained even when increasing the number of iterations to 5,000,0000, especially for the first period (May 2011–March 2012) (Table 2.1; Data used: Crater floor). For both periods, the best source is located on the south-west side of the active crater. However, the residuals close to the active crater are large and not randomly distributed (Figure 2.12a and 2.13a) indicating that the magnetic changes in this area are not well–explained.

We therefore isolated this area by inverting a subset of the data (the sites west of the fumarole area only) for both periods. The best source is smaller, shallower and closer to the active crater than when using the whole dataset (Table 2.1; Data used: West of fumaroles). The residuals are small but again, not randomly distributed: the north area is underestimated and the south is overestimated (Figures 2.12b and 2.13b). This indicates that the model is not appropriate to explain the data.

We finally isolated an even smaller zone close to the anomaly previously defined by only using the data recording the magnetic anomaly to the north-east of the active crater. The best source explaining these data is located in the middle of the crater area at very shallow depth (Table 2.1; Data used: Anomaly only). The residuals are small and randomly distributed suggesting that the model is appropriate to explain the data (Figures 2.12c and 2.13c). We therefore favour this last inverted source as the most appropriate to explain the magnetic changes observed during the periods May 2011–March 2012 and March 2012–June 2012 on the White Island crater floor. The best source of the heating episode is bigger (almost twice the size) and located at greater depths and to the south-west than the source of the cooling episode. This could suggest different sources hence a non-reversible process where cooling occurred in a different area than the area previously heated. However, the differences in the characteristics of the two sources (heating and cooling respectively) are small and could also be due to errors in the measurements. We therefore can not be conclusive on whether the same shallow portion of the active crater was heated then cooled down by the same amount, or whether cooling occurred in a different area (e.g., smaller and/or adjacent) than that previously heated.

Period	Data used	Initial guess	Source x–offset (m)	Source y–offset (m)	Source depth (m)	Source radius (m)
May 2011–March 2012	Crater floor	1	-2060	-404	1596	932
		2	-1688	-321	1909	1396
	West of fumaroles	1	-304	-38	437	398
		2	-303	-38	436	397
	Anomaly only	1	-73	12	232	213
		2	-73	12	232	212
March 2012–June 2012	Crater floor	1	-333	-92	547	342
		2	-322	-89	539	335
	West of fumaroles	1	-178	15	368	267
		2	-179	15	369	268
	Anomaly only	1	54	48	168	112
		2	54	48	168	112

Table 2.1: Results from the inversions of the magnetic changes between May 2011 and March 2012. The horizontal locations are relative to the location of the Vent 2 (Figure 2.1). The location and radius are given in metres. Initial guess 1 is (0, 0, -250, 150), initial guess 2 is (100, 100, -350, 250).

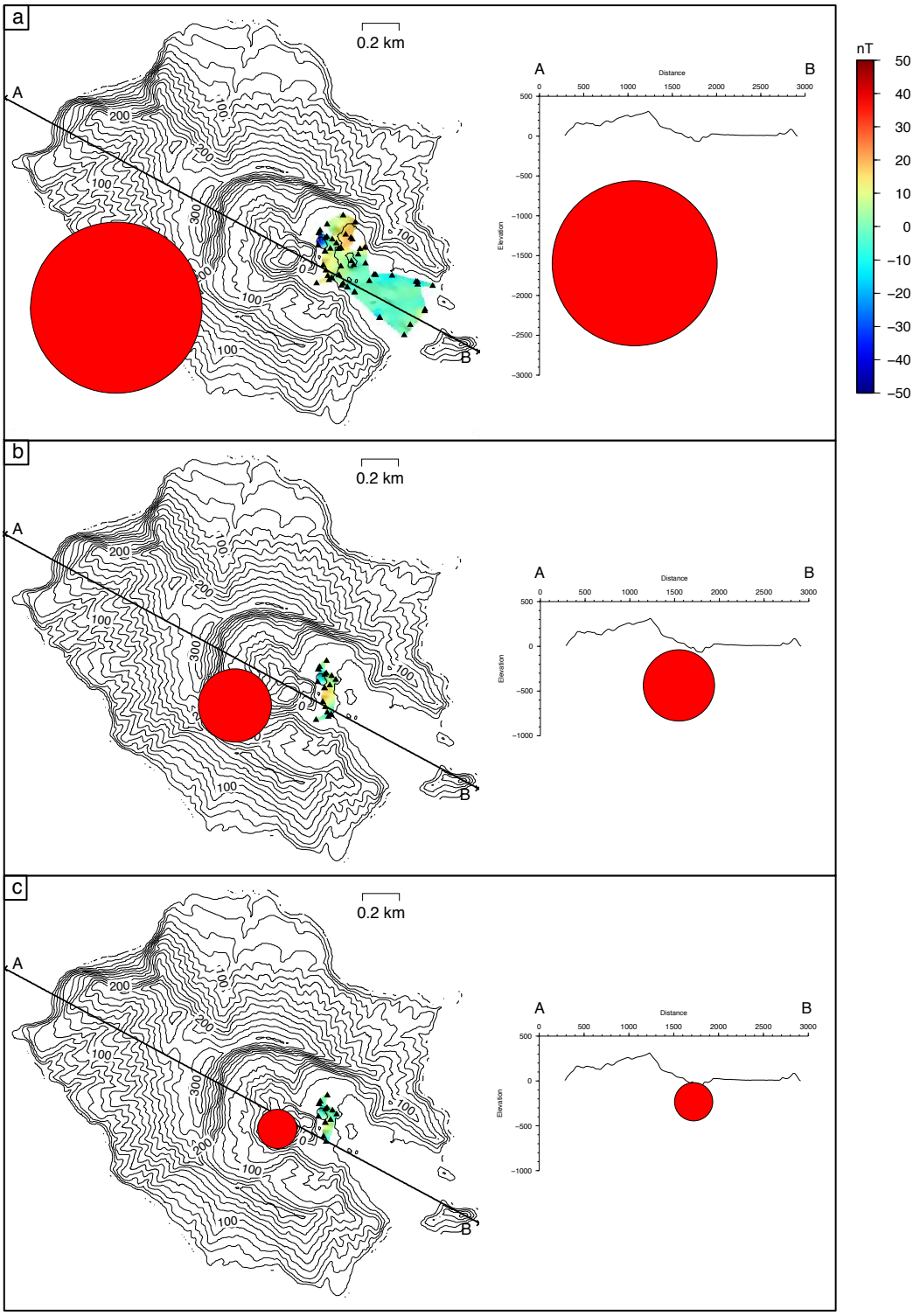

Figure 2.12: Results of the inversions of the magnetic changes between May 2011 and March 2012 for a dipole source being heated by 50 °C between 350 and 600 °C: a. using the whole dataset; b. using the sites west of the fumaroles only and c. using the sites local to the anomaly only. For each result are plotted a map of the residuals (difference between modelled and measured changes, in colours) with the horizontal location of the best source (red sphere) (left panel). The source is also projected along the profile A–B (right panel, axes are in metres).

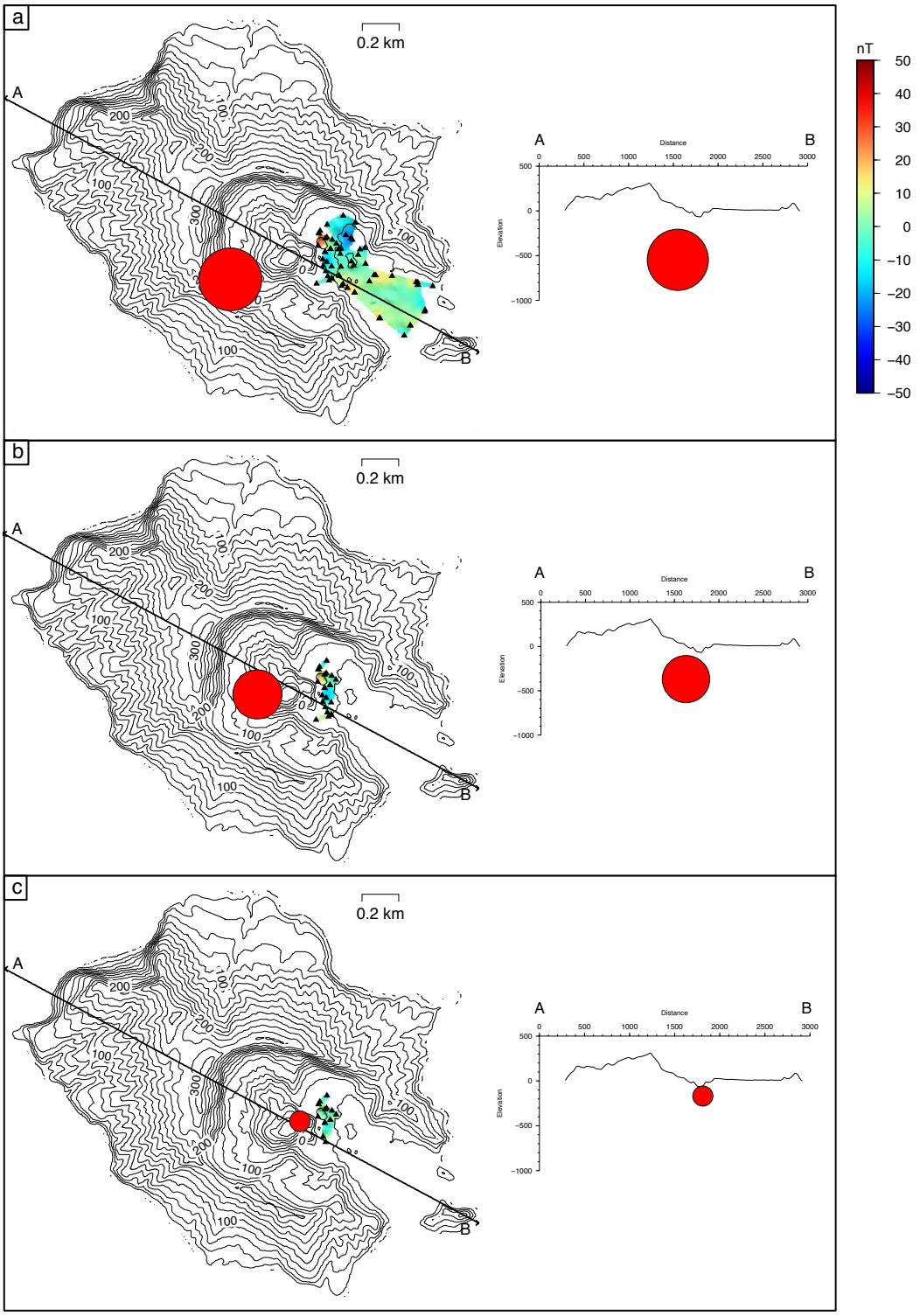

Figure 2.13: Results of the inversions of the magnetic changes between March and June 2012 for a dipole source being cooled by 50 °C between 350 and 600 °C: a. using the whole dataset; b. using the sites west of the fumaroles only and c. using the sites local to the anomaly only. For each result are plotted a map of the residuals (difference between modelled and measured changes, in colours) with the horizontal location of the best source (red sphere) (left panel). The source is also projected along the profile A–B (right panel, axes are in metres).

Our inversion results suggest that thermal changes (a change of 50°C between 350 and 600 °C) occurred at very shallow depth under the active crater area of White Island volcano. Heating in the upper 500 m below the crater lake between May 2011 and March 2012 is consistent with the lake level decrease. Our results also suggest that cooling at about the same location (the upper 500 m below the crater lake) occurred between March and June 2012, and this was accompanied by a small lake level decrease.

The source of these thermal changes can be constrained using the principle of energy conservation. Changing the temperature of a 200 m spherical body of rock by 50 °C requires an energy of 2.3 $\times$ 10^{15} J (assuming a rock density of 2000 kg m^3 and a rock specific heat capacity of 700 J kg^{-1} °C). Thermo–magnetic changes at White Island have been ascribed to circulation of hot/cold fluids within a permeable medium (Hurst and Christoffel, 1973; Christoffel, 1989; Hurst et al., 2004). Assuming that most of the energy/heat is carried by water, in the vapour phase for our range of temperature and depth, this energy can be provided by 6.5 $\times$ 10^8 kg of water vapour (with an enthalpy of 3500 kJ kg^{-1}). If all this vapour comes from a melt (degassing entirely), the corresponding melt has a mass of 1.1 $\times$ 10^{11} kg (given a water content of 0.6 wt% in the melt inclusions, Wardell et al., 2001). Taking a melt density of 2700 kg m^{-3} (consistent with a degassed magma not yet solidified, Fournier (2003) and references therein), this implies that 0.04 km^3 of melt entirely degassed its water content which heated the shallow part of the crater area.

This volume is large compared to the volume erupted during the 1976-82 period (0.001 km^3, Houghton and Nairn, 1989b). It is also large compared to the usual degassing magma volume (0.025 km^3 yr^{-1}, Giggenbach and Sheppard, 1989; Werner et al., 2008), calculated from the average SO_2 emission (350 t day^{-1}) and taking a sulphur content of 1000 mg kg^{-1} in the melt and a magma density of 2700 kg m^{-3}. The average SO_2 emission between May 2011 and March 2012 is 320 t day^{-1}, very close to the long–term emission suggested by Giggenbach and Sheppard (1989). This represents the degassing of 0.018 km^3 of melt, half of the volume calculated from heat calculation responsible for the magnetic changes. Several hypotheses can be put forward to explain why the estimate of magma volume from energy calculation is bigger than that from SO_2 emissions. First, we only considered the heat leading to the magnetic changes to be provided by water vapour degassing from an intrusion. It is likely that the water vapour might not have come only from the melt but also from convection within the hydrothermal system. This implies that a smaller intrusion would be required to produce the magnetic changes. Alternatively, the gas exsolving from the melt might not have reached the surface owing to scrubbing by the hydrothermal system, implying the possibility of a bigger intrusion than the

one calculated from SO_2 emissions.

We envisage the scenario of increased degassing to explain the heat source leading to magnetic changes. This increased amount of gas can come from different depths and magma bodies. Either it exsolves from the magma chamber at depth (likely due to deep recharge of this magma chamber) (i.e., deep degassing) (scenario 1). Alternatively, degassing can occur from the emplacement of a shallow intrusion (scenario 2). A combination of both scenarios (deep and shallow degassing) is another possibility. Additionally, there are likely interactions with the heated and convecting hydrothermal system which provides additional heat to the system. With this model, hot fluids first heated the system between May 2011 and March 2012 (to explain the magnetic anomaly) and pressurised the system. When they degassed at the surface from May 2012, they depressurised the system, allowing the inflow of colder water (cooling the system and explaining the magnetic changes between March and June 2012). The rise of an intrusion (scenario 2) would have likely led to other geophysical changes. Analysing these results while accounting for the lack of significant the gravity changes during the period of interest can therefore help constrain these different scenarios.

2.5.2 Forward gravity modelling

2.5.2.1 Modelling procedure

Our results and observations suggest that changes in mass and density might occurred at White Island between May 2011 and June 2012. First, the magnetic changes observed between May 2011 and March 2012 at White Island suggest the possibility of an intrusion but there are questions associated with the volume of this intrusion. Second, we observed an approximate 2–m crater lake level decrease between May 2011 and December 2011, which then remained constant or slightly decreasing until June 2012 (Figure 2.2). Third, this lake level decrease was likely associated to a groundwater level decrease. However, no significant gravity changes were observed during this period. We use a forward modelling approach to investigate the effect of the lake level decrease, of the groundwater level decrease and of the possible intrusion on gravity changes. The aim is to constrain the volume of the possible intrusion to help understand the nature of the thermal changes inferred from the magnetic changes.

We only have gravity data on June 2011, December 2011 and June 2012 to constrain the model. Because most of the hydrological changes seem to have occurred between May and December 2011 (and then remained constant, constrained by the lake level), we can directly compare the modelling results to the observed gravity changes between June 2011 and June 2012. Conversely,

we can not constrain the model involving an intrusion inferred between May 2011 and March 2012 because we do not have any gravity data in March 2012. However, assuming that the density of this intrusion remained constant between March and June 2012, we can also compare the modelling results to the gravity changes observed between June 2011 and June 2012.
We modelled the gravity changes using the 2.5D GRAVMG32 modelling software which computes gravity along profiles and accounts for topography. Our modelling procedure involved several assumptions. First, given the configuration of the network and the location of the source for the magnetic changes (under the crater), we only computed the gravity changes on one profile, crossing the crater floor radially from the active crater (profile C–D, Figure 2.9). This implies that we don not account for local topographic effect i.e., local spatial variations of topography relative to the profile chosen for the modelling. The topography within the crater floor is relatively smooth, mainly dominated by local mounds and gullies (maximum elevation of $\sim$ 20 m), with the gravity sites generally away from these features. This implies that local topography effects on gravity changes is small at the measured sites so that the chosen profile is a good representation of the crater floor topography. Second, the lake level decrease was visually observed and estimated implying an unconstrained potential large error in the estimates. Third, we did not perform groundwater level measurements but constrain its behaviour from observations made over the crater floor and at the crater lake, assuming that the groundwater level varies as a function of the crater lake level. These assumptions imply that we are interested in orders of magnitude for the gravity changes.

2.5.2.2 Hydrological effect on gravity changes

We modelled the 2–m lake level decrease as the effect of a prism following the topography, with a density 1000 kg m^{-3} lower than the surrounding medium. This is consistent with a model whereby air replaces water inside this prism. We observe that such a crater lake level decrease is not depicted by our gravity network, i.e., the gravity difference between the sites and the reference one is less than 13 μGals (Figure 2.14).

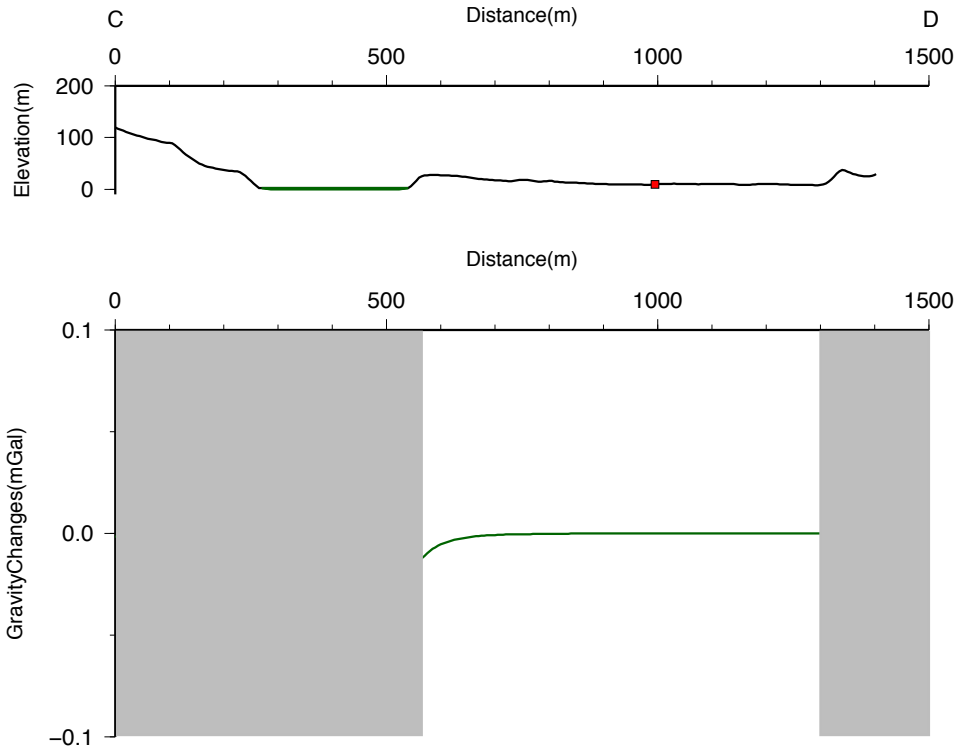

Figure 2.14: Gravity changes (bottom) at the surface along the profile C–D (top, see Figure 2.9 for location), relative to GR01 (red square), due to a 2–m lake level drop (dark green). The gray boxes delimit the coverage of the gravity network, i.e. the crater floor.

Observations indicate that the groundwater table is very shallow in the crater floor. Not having precise measurements of its level, we argue that it likely follows the topography, being higher close to the crater lake than close to the sea. Its level probably dropped close to the crater between May 2011 and June 2012, associated to the crater lake drop. The presence of springs flowing from the crater lake edge to the crater lake suggests that the groundwater table at the edge of the crater lake is higher than the crater lake level. Without any constraint on its geometry, we propose two scenarios for the groundwater level drop. In the first model, the level uniformly decreased by 2 m with the crater floor, and is represented by the effect of a change in density in a rectangular slab. The second model considers that the groundwater level dropped by a larger amount towards the lake than close to the sea. This is modelled as the effect of a density change in a wedge. In both scenarios, the medium within the geometry (either slab or wedge) has a density 400 kg m^{-3} lower than the surrounding medium. This is consistent with a model whereby unsaturated ash tuffs replaces saturated ash tuffs, the tuffs having a porosity of 0.4 (consistent with laboratory measurements from Heap et al. (2015)). The wedge geometry leads to more gravity changes at the surface relative to the reference station (Figure 2.15), but

neither of the two models lead to detectable changes by the gravity network (maximum of -30 μGals at the westernmost station), given our current assessment of the error at each site.

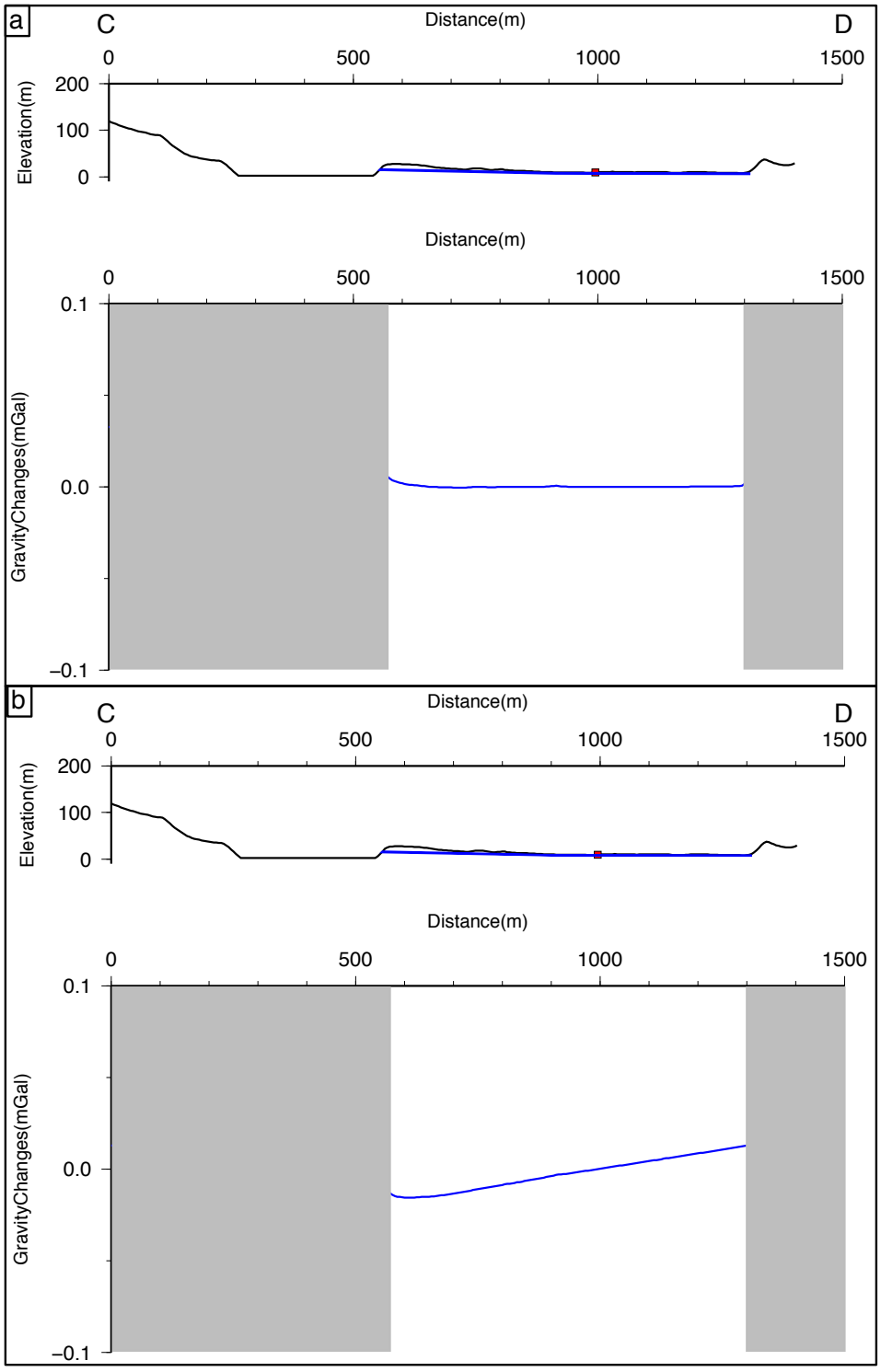

Figure 2.15: Gravity changes (bottom) at the surface along the profile C–D (top, see Figure 2.9 for location), relative to GR01 (red square), due to a 2–m groundwater level drop (blue), if represented by a slab (a) or by a wedge (b). The gray boxes delimit the coverage of the gravity network, i.e. the crater floor.

2.5.2.3 The possibility of a magmatic intrusion

We modelled the gravity changes within the crater floor due to an intrusion. From our previous results, the melt volume differs depending on whether it is computed from the magnetic changes (0.04 km^3) or from SO_2 emissions (0.018 km^3). We therefore tested both scenarios (Figure 2.16). We placed this intrusion below the magnetic anomaly, its top being therefore at 500 m depth. This depth corresponds to that of a storage zone inferred by deformation during the 1976–82 eruptive sequence (Clark and Otway, 1989). We modelled the effect of a prism with a density 700 kg m^{-3} higher than the surrounding medium. The density contrast is consistent with a model whereby an intrusion with a density of 2700 kg m^{-3} (i.e., a degassed magma not yet solidified, (Fournier (2003) and references therein) replaces a medium layered with old lavas and ash tuffs of density 2000 kg m^{-3} (using bulk densities within the crater floor from ambient noise interferometry (Fry et al., 2015) and laboratory measurements (Heap et al., 2015). We only considered the case whereby the intrusion has a conduit geometry. In order to observe no (or within noise) gravity changes at the surface relative to our reference point, the intrusion has to be comprised within a narrow conduit (cross sectional area of 100 m^2). To account for the inferred melt volume, the conduit needs to be 1800 m long (for a volume of 0.18 km^3 or 4000 m for a volume of 0.04 km^3). A narrower conduit, more consistent with the White Island system, would imply an even greater length which is unrealistic for the system. Whichever scenario we envisage for this conduit geometry, either it is unrealistic for the White Island system, or it leads to significant gravity changes that were not observed. The lack of gravity changes therefore implies that if there is emplacement of a shallow intrusion, the intrusion has to be comprised within a narrow conduit at shallow depth.

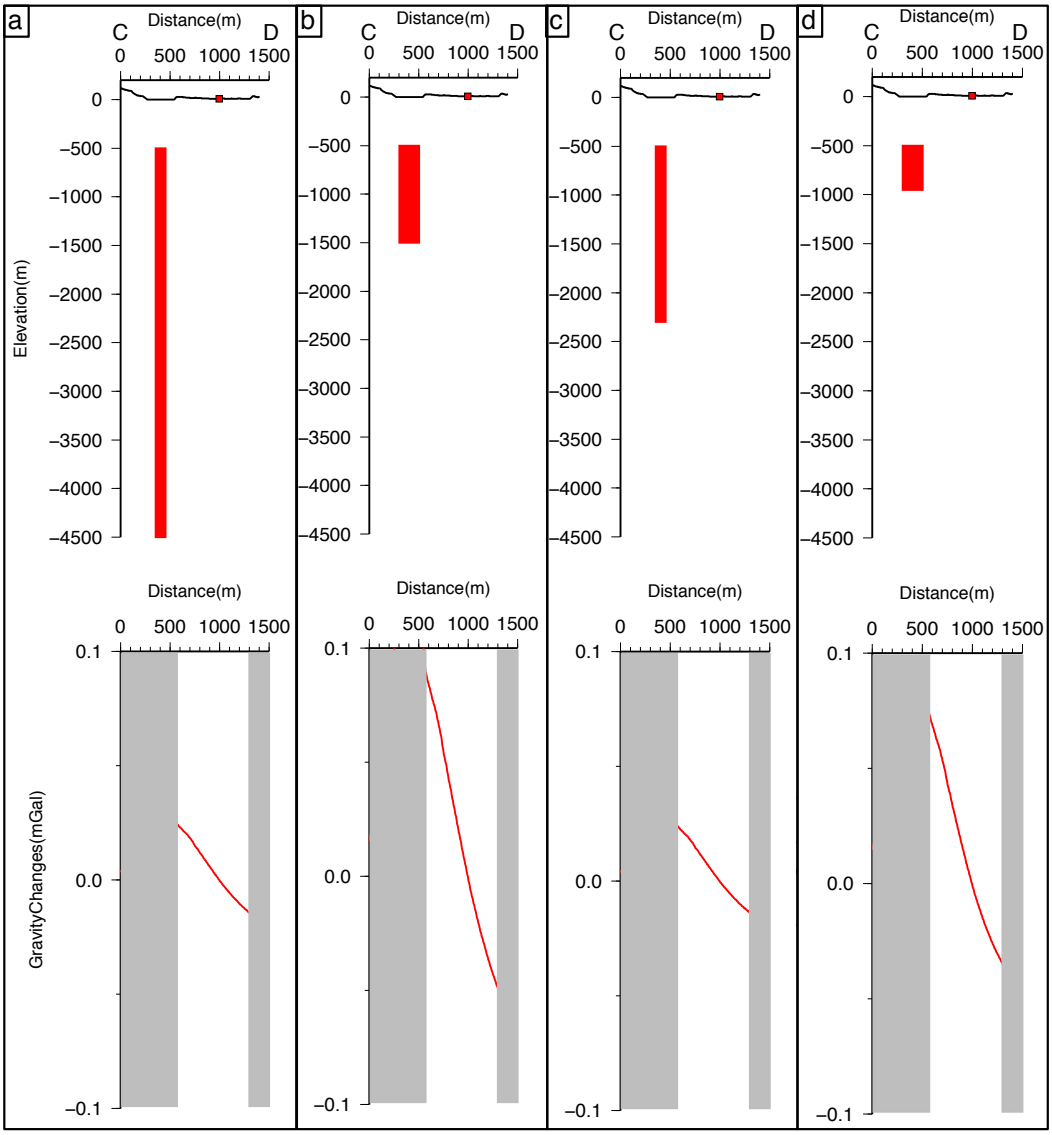

Figure 2.16: Gravity changes (bottom) at the surface along the profile C–D (top, see Figure 2.9 for location), relative to GR01 (red square), due to an intrusion (red): a. with a volume of 0.04 km^3 and dimensions $100 \times 100 \times 4000$ m, b. with a volume of 0.04 km^3 and dimensions $200 \times 200 \times 1000$ m, c. with a volume of 0.018 km^3 and dimensions $100 \times 100 \times 1800$ m, d. with a volume of 0.018 km^3 and dimensions $200 \times 200 \times 450$ m. The gray boxes delimit the coverage of the gravity network, i.e. the crater floor.

Other scenarios could lead to no significant gravity changes at the surface. First, a model whereby the intrusion is comprised within a shallow conduit at shallower depths which widens at greater depths would produce small gravity changes since gravity is more sensitive to shallow structures than deeper ones. Second, hydrothermal effects could allow the presence of a bigger intrusion. The gravity effect of the intrusion counteracts that of the groundwater level decrease.

It is possible that we underestimated the groundwater level decrease because we deduced its level from observations of the crater lake without measuring it directly. Additionally, the effect of a phase change (vaporisation) in the crater area due to the additional heat from the intrusion would cause a gravity decrease also counteracting the effect of an intrusion. This possible hydrothermal effect would allow the emplacement and degassing of a larger intrusion without leading to any gravity changes at the surface.

2.5.3 Signals of an impending eruption?

We propose that the observed magnetic changes are due to the rise of deep magmatic fluids interacting with the shallow hydrothermal system of the volcano. Numerical fluid flow models (e.g., Todesco et al., 2010) provide evidence that this model can explain the observed geophysical changes. Heating in the shallow 500 m below the crater, inferred from the magnetic changes observed between May 2011 and March 2012, is consistent with the expansion of the thermal front due to the injection of hot hydrothermal fluids in the hydrothermal system. Pore pressure and temperature changes are potential sources for ground deformation (Hurwitz et al., 2007; Hutnak et al., 2009; Fournier and Chardot, 2012; Todesco et al., 2010). Todesco et al. (2010) showed that the injection of hot fluids can lead to subsidence in highly permeable systems, where hot fluids propagate quickly to the surface relieving the pore pressure while the inflow of cold water lowers the temperature in the system. Such a model could explain the subsidence observed over the crater floor between June 2011 and December 2011 (Figure 2.9). The rise of hot gaseous hydrothermal fluids would lead to a gravity decrease especially at sites close to the hydrothermal plume (Todesco et al., 2010 and Chapter 3 of this thesis). We do not observe a significant gravity decrease but this could be due to the high level of noise in our data or to the counteracting effect of an intrusion. Volcanic gas emissions (mainly SO_2) increased from May 2012, suggesting that the volcanic fluids reached the surface. This likely caused a depressurisation of the system allowing the inflow of colder fluids as in the models by Todesco et al. (2010). This inflow of colder fluids could explain the cooling pattern inferred from our magnetic measurements between March and June 2012. Todesco et al. (2010) emphasises that strong gravity changes can be observed along the transitional boundary between single-phase liquid and two-phase vapour-liquid. It could be that the gravity sites where we currently have a large error are close to this zone. This implies that a combination of repeated magnetic and gravity campaigns, in addition to regular monitoring techniques, can enhance the volcano monitoring capabilities to better understand the state of the volcano.

The rise of these deep hydrothermal fluids preceded the eruptive phase which started on 4 August 2012 with an eruption containing some juvenile material. It is possible that these fluids represented the envelope surrounding a small magmatic intrusion above the reservoir, or that the increased degassing depressurised the magma chamber allowing the magma to rise. In both cases, this increased degassing appears to be precursory to the eruptive phase.

2.6 Conclusion

We analysed the source of the magnetic and gravity changes observed at White Island volcano between May 2011 and February 2015, which comprises the recent unrest/eruptive period, to assess the potential of these techniques for unrest characterisation. Inverse modelling of the magnetic changes suggest some thermal changes in the upper 500 m below the active crater. The lack of significant gravity changes during the same period was used to constrain the possibility of an intrusion degassing at shallow depth. We propose that the observed geophysical changes are consistent with a heating episode followed by a cooling episode that are interpreted in this study as resulting from the effect of a period of increased gas injection associated with the possible emplacement of an intrusion, preceding the eruptive phase. Heating stems from the rise of magmatic fluids that escaped the system and allowed inflow of colder water which subsequently cooled down the system at shallow depths. Magnetic and gravity campaigns are therefore useful tools to depict and characterise unrest at White Island.

We recommend that magnetic measurements be performed regularly on the White Island crater floor to depict any signs of volcano unrest, either in campaign mode or by installing continuous instruments at specific locations. Performing additional microgravity measurements can help understand the volcano state because they allow to discriminate between different models. In this study, the gravity changes observed during the period of interest were within or very close to the noise level, allowing to discard the scenario by which the magnetic changes were due to the rise of a large intrusion at $\sim$500 m depth. However, the effect of an intrusion can counteract that of hydrothermal activity (lake and groundwater level decrease, phase change). A better quantification of the noise at the gravity sites, along with precise measurements of the lake level and groundwater level would be useful to further constrain the models.

Preamble

The preceding chapter summarised the observables associated with the 2011-2013 unrest/eruptive episode at White Island. Modelling results suggested that a period of increased degassing and a possible intrusion are potential sources for the magnetic changes and the lack of significant gravity changes over the crater floor during the episode. However, the apparent lack of gravity changes could be due to the high level of noise in our data (especially at the site between the fumarole and the crater lake) or to a strong hydrothermal effect (vaporisation leading to a density decrease counteracting the gravity increase due to an intrusion). In this chapter, I investigate an episode of increased degassing within a fumarole (using parameters consistent with the main fumarole at White Island), and its effect on hydrothermal circulation and gravity changes. Previous studies inferred that the fumarole conduit might be inclined. I therefore perform some numerical simulations of hydrothermal circulation involving fumarole conduits with different inclinations. This chapter will answer the next research questions of this thesis (Table 1.1) in order to reach the second objective of this research set in the introduction chapter ("To describe the effect of an inclined fumarole on hydrothermal circulation and gravity changes to highlight the contribution of structural effects to the geophysical observables and help constraining the source of the observables").

Chapter 3

Modelling the effect of an inclined fumarole conduit on hydrothermal circulation and gravity changes

Abstract

Interpreting geophysical observables in volcano-hydrothermal environments is challenging because of the complexity of volcanic processes occurring in heterogeneous settings. Fluid migration is particularly affected by the distribution of permeable pathways. Better understanding this effect is key to assess the source of the observables. In this study, we focus on constraining the contribution of the inclination of a permeable conduit to hydrothermal circulation and associated gravity changes. We present results from numerical simulations of hydrothermal circulation driven by the release of heat and magmatic fluids at depth, within a heterogeneous domain containing a fumarole with varying inclinations from the vertical (0 and 7°). The fumarole has characteristics consistent with the fumarole 0 at White Island volcano (New Zealand). Its diameter (1.25 m^2) is consistent with dimensions of the fumarole outlet. It is ten times more permeable than the surrounding medium, consistent with laboratory measurements made on solfatara deposits and volcanic tuffs. We simulate hydrothermal circulation due to a varying source of magmatic fluids feeding the fumarole using TOUGH2, and compute the associated gravity changes at the surface. We investigate the effect of the fumarole inclination on 1. steady state conditions and 2. hydrothermal circulation and gravity changes at the surface associated with a one-year long episode of unrest. At steady state, the hydrothermal plume is comprised of dry-gas surrounded by a two-phase region. Regardless of the fumarole inclination, the hydrothermal plume is centred above the injection area, i.e., around the fumarole outlet for the vertical fumarole only. Most density changes associated with the following unrest occur at the edge of the two-phase hydrothermal plume, which expands during the unrest phase due to the excess

gas, and returns to steady state conditions after the unrest ceases. This leads to a gravity decrease around the fumarole during the unrest period and the following 3 months due to inertia, followed by a gravity increase. Outside a 100 m radius from the outlet, the gravity changes at the surface mainly reflect density changes within the top layer of the domain, and are characterised by a gravity increase during the unrest period, followed by a gravity decrease as liquid water condenses and vaporises respectively. Because the two-phase plume is located above the injection area for both fumarole inclinations, the effect of the fumarole inclination is to shift the gravity anomaly from the fumarole outlet towards the injection area. The fumarole acts as a preferential pathway for fluid ascent and therefore narrows the hydrothermal plume compared to a homogeneous domain. However, the difference in gravity changes is within usual measurement error (2 μGal). This implies that the gravity changes from our simulations including a fumarole are similar to those expected for a homogeneous medium where the injection source has different locations. If the injection area of the fumarole 0 at White Island is a few hundred metres away from the outlet (as suggested by surface deformation), we could therefore expect the gravity anomaly to be offset by the same amount from the fumarole outlet. We conclude that an inclined fumarole conduit can shift the location of geophysical anomalies away from their surface manifestation. The location of these geophysical anomalies can therefore provide clues to the location of the deeper origin of the fluids.

3.1 Introduction

Depicting and interpreting signs of volcanic unrest in hydrothermal environments is challenging because of the different potential sources. First, these signals can be of magmatic nature, and they can also be affected by hydrothermal circulation (e.g., Gottsmann et al., 2005; Todesco, 2009). Second, the heterogeneous nature of volcanic systems and the limited knowledge on the volcanic structures at depth adds complexity to the interpretation of the signals (e.g., Todesco, 2009). It is therefore of paramount importance to discriminate between these effects to improve the interpretation of observables depicting volcanic unrest.

Modeling of magmatic hydrothermal systems involves solving numerically coupled and non-linear multiphase flow equations, heat transport, and mechanical response of the system (Ingebritsen et al., 2010). The effect of a varying injection of magmatic fluids within a hydrothermal system has been extensively investigated to explain passive degasing, deformation, gravity and electrical changes at Campi Felgrei (e.g., Todesco et al., 2003; Todesco et al., 2004; Todesco and Berrino, 2005; Rinaldi et al., 2010; Rinaldi et al., 2011), and to explain cyclic heating events beneath Ruapehu Crater Lake (Christenson et al., 2010). In a more general case, hydrothermal unrest is a possible source for the uplift observed at large calderas (Hurwitz et al., 2007; Hutnak

et al., 2009). Several studies demonstrated the effect of the rock properties on hydrothermal circulation and associated geophysical changes (e.g., Todesco et al., 2003; Todesco et al., 2010). In particular, Todesco et al. (2010) highlighted that the distribution of porosity and permeability affects degassing, deformation and gravity, controlling the timing and amplitude of their changes through space and time. These studies considered vertical permeable channels. However, because these permeable structures usually follow discontinuities within volcanoes, such as crater boundaries, inclined conduits are worth considering. Here, we present the first study of the effect of an inclined fumarole conduit on fluid circulation and gravity changes.

The fumarole 0 area at White Island (New Zealand) is a case in point where geophysical signals are affected by hydrothermal circulation and where an inclined conduit was inferred by previous studies. Earlier work by Giggenbach (1987) on Donald Mound to the North of the area (used as a proxy for this study) highlighted two components in the fumarolic discharge at White Island: a magmatic component (high in SO_2) and a hydrothermal component rising slowly at the surface from a two-phase brine surrounding the magmatic system. During the period 1972-85, the fumarole discharge was subject to cyclic changes in response to corresponding variations in the rate of gas release from the underlying magma affecting the deep hydrological regime (Giggenbach and Sheppard, 1989). Recent deformation patterns observed in the proximity of this fumarole have been ascribed to hydrothermal processes (Peltier et al., 2009; Fournier and Chardot, 2012). Fournier and Chardot (2012) suggested that the two recent uplift episodes were due to pore pressure changes within the feeding system of the fumarole. The sources of deformation were not directly underneath the fumarole outlet, and the authors inferred an inclined conduit to explain these. This suggests the need to account for structural features when interpreting geophysical observables at White Island.

In this study, we focus on a first ever assessment of the effect of inclined fumarole conduits on geophysical parameters. We analyse how inclined conduits affect hydrothermal circulation and gravity changes, at steady state and associated with an episode of unrest. We first describe our numerical modelling strategy and the physical model based on the settings from fumarole 0. We then present results from several simulations when varying the fumarole inclination, to highlight the role of the conduit geometry on the hydrothermal plume at steady state and during a simulation of a year of unrest followed by a quiet period. For these unrest simulations, we also characterise the role of the conduit geometry on gravity changes at the surface. We then discuss how our results can help the interpretation of geophysical changes for volcano monitoring.

3.2 Methods

Simulations of hydrothermal circulation were performed using the TOUGH2 code, a multi-component and multiphase simulator describing the coupled flow of heat and mass through a porous medium (Pruess et al., 1999). We accounted for the presence of water and CO_2 (EOS2 module) where the dissolution of CO_2 in water is described by Henry's law (i.e., at a constant temperature, the amount of CO_2 that dissolves in water is directly proportional to the partial pressure of CO_2 in equilibrium with water). We used Corey's type relative permeability functions with irreducible saturations of 0.333 and 0.05 for the liquid and gas phase, respectively. Capillary pressure decreases linearly from 0.1 to 0 MPa for liquid saturations between 0.333 and 1. PyTOUGH (Croucher, 2011) was used to assist running the simulations, visualising TOUGH2 results, and computing gravity changes at the surface.

We constrained our model using parameters consistent with the fumarole 0 area at White Island volcano. The 3-D heterogeneous domain has dimensions 600×600×200 m and comprises a permeable fumarole embedded in a less permeable medium. Rock properties for the different media are given in Table 3.1. Permeability and porosity are consistent with measurements made on solfatara deposits sampled from fumarole 0 (proxy for rock type of the fumarole) and on coarse ash tuff (proxy for the rock type of the surrounding medium) (Letham-Brake, 2013; Heap et al., 2015). Density was estimated from bulk density obtained from ambient noise interferometry (Fry et al., 2015) and measured porosity (assuming that all pores are connected, i.e., connected porosity equals total porosity) (Heap et al., 2015). The other rock properties are unknown for White Island. Because the shallow material within the main crater is likely composed of tuffs mainly (Letham-Brake, 2013; Heap et al., 2015), we used values used by (Todesco et al., 2010) for Campi Flegrei tuffs.

	Rock	Fumarole
Density (kg m^{-3})	2700	2000
Permeability (m^2)	10^{-13}	10^{-12}
Porosity	0.4	0.2
Conductivity (W m^{-1} °C^{-1})	1.15	1.15
Specific heat (J kg^{-1} °C^{-1})	900	900

Table 3.1: Rock properties for the different media, kept constant during the TOUGH2 simulations.

To assess the effect of the fumarole inclination on hydrothermal circulation and gravity changes,

we performed two sets of simulations with one simulation for the vertical case, and one for an inclination of 7° from the vertical. This inclination is arbitrary and was chosen in order to maintain the same mesh for both sets of simulations. The mesh is composed of rectangular and triangular prisms and contains 21980 blocks. The layers have a constant thickness of 10 m. Conversely, the horizontal dimensions of the blocks vary, and the mesh is refined around the fumarole (Figures 3.1 a and b). For both sets of simulations, the fumarole outlet is at the centre of the model (Figure 3.2 c) with an area of 1.25 m^2. This area is consistent with the area of the fumarole 0 conduit at the surface. The vertical fumarole has a constant diameter (4 blocks in each layer) and extends from the top to the bottom of the domain (Figure 3.2 a). The inclined fumarole also has an injection and outlet area of 1.25 m^2. We kept the same vertical connection area along the fumarole. In each layer in between the top and bottom layers, the fumarole consists of 8 blocks. The inclination is obtained by shifting these blocks by 1.25 m^2 stepwise to the left edge of the model (decreasing x, constant y), when moving to the layer underneath (Figure 3.2 b). The inlet of the inclined fumarole is 22.5 m away (to the left of the domain) from the outlet.

We assessed the effect of the fumarole on hydrothermal circulation by modelling the same scenario within a homogeneous domain with the rock properties of the surrounding medium (i.e., with no fumarole). We also tested the effect of the mesh on the results by performing an additional simulation with the same vertical fumarole but with the mesh symmetrically refined around it (Figures 3.1 c and d).

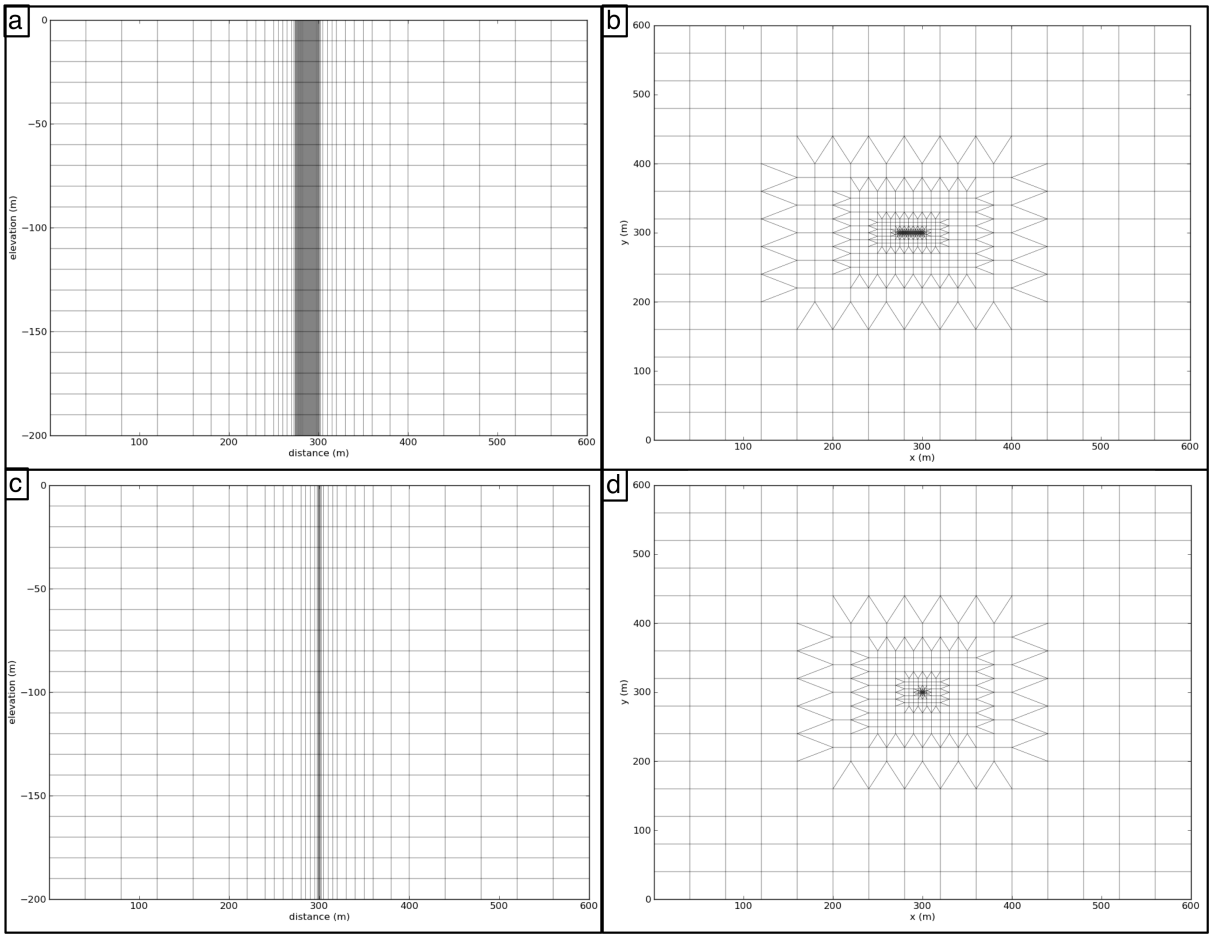

Figure 3.1: Meshes used for the TOUGH2 simulations (a) reference mesh in cross section, (b) reference mesh in map view, (c) simple mesh in cross section and (d) simple mesh in map view.

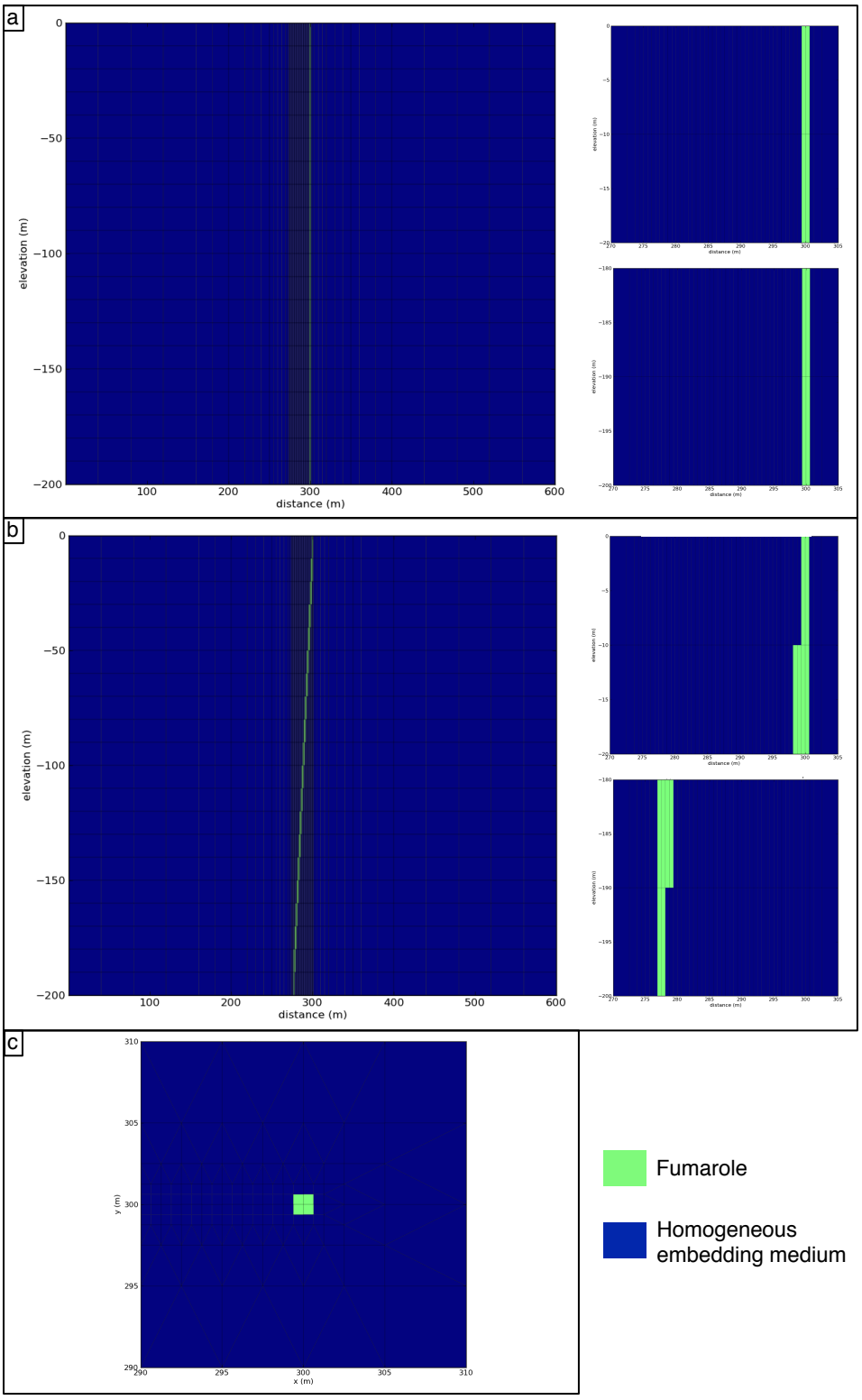

Figure 3.2: Computational domain and rock properties used for the TOUGH2 simulations in cross section for (a) the vertical fumarole, (b) the inclined fumarole and (c) in map view for both fumarole inclinations. The right panels for (a) and (b) are close-ups on the central top and bottom part of the domain to show the implementation of the fumarole.

The top boundary condition is open to fluid and heat flow, fixed at atmospheric conditions and single-phase gas (Tatm = 15 °C, Patm = 1.0132 bar, PCO2 = 1 bar (∼ Patm)). Several options exist for the implementation of this boundary condition in TOUGH2. To represent the atmosphere, we chose to create a block with a huge volume and specific heat capacity (1×10^{25} m^3 and 1×10^5 J kg^{-1} $°C^{-1}$) in order not to affect the heat and mass balance. This block is then linked to the centre of each block of the top layer. This implies that our top boundary condition is applied at at 5 m depth. The side and bottom boundaries of the model are impermeable and adiabatic (default boundary type for TOUGH2), except at the base of the fumarole where hot fluids (H_2O and CO_2) are injected. The fluid temperature (Table 3.2) is defined by their enthalpy, using the NIST web-based thermophysical properties of fluid system calculator (http://webbook.nist.gov/chemistry/fluid/).

For each domain, defined by a different fumarole inclination, we first simulated a quiet period and used the steady conditions of this simulation as initial conditions for a second simulation representing unrest. During the first simulation (quiet), hot fluids were injecting at constant rate at the bottom of the fumarole. The initial conditions for this simulation were: hydrostatic pressure and thermal gradient (225 °C km^{-1}). The thermal gradient is unknown for White Island so we chose this relatively high thermal gradient consistent with Campi Flegrei (Todesco et al., 2003). During the second simulation (unrest), fluids were injected at a higher rate (+50% H_2O) with an increased CO_2/H_2O ratio (×2) and temperature (+50 deg°) for 1 year, then set back to the values of the quiet period. The temperatures were arbitrarily chosen, along with the injection rates but the CO_2/H_2O ratios are consistent with those measured prior and during the 2011-2013 eruptive period at White Island volcano (Chardot et al., 2013) (Table 3.2).

	Quiet	Unrest
Fluid temperature (°C)	300	350
H_2O injection rate (ton day^{-1})	166	207.5
CO_2 injection rate (ton day^{-1})	10	24.9
CO_2/H_2O	0.06	0.12

Table 3.2: Characteristics of the quiet and unrest periods of the simulations.

Gravity changes associated with the unrest simulation are computed at the surface by adding the contribution of the density changes through time within each block of the domain, following the formulation by Todesco and Berrino (2005). The average density change in a block k of the domain between t and $t0$ ($dD^1_{t-t_0}$) is given by Equation 3.2.

$$dD^k_{t-t_0} = (SG^k_t \times DG^k_t + (1 - SG^k_t) \times DW^k_t) - (SG^k_{t0} \times DG^k_{t0} + (1 - SG^k_{t0}) \times DW^k_{t0} \quad (3.1)$$

with SG the gas saturation, DG the density of the gas phase and DW the density of the aqueous phase). The contribution of block k to the vertical component of the gravity change at an observation point at the surface of the domain ($dg^k_{t-t_0}$) is given by Equation 3.2.

$$dg^k_{t-t_0} = \frac{\phi^1 V^k dD^k_{t-t_0} z^1 G}{L^{1^3}} \quad (3.2)$$

with L the distance between the block k and the observation point, ϕ the porosity, V the block volume, z the block depth and G the universal gravitational constant (6.67384×10^{-11} $m^3kg^{-1}s^{-2}$). The vertical component of the gravity changes due to each block of the domain (dg_{t-t_0}, N blocks in total in the domain) is the sum of the gravity changes due to each block (Equation 3.2).

$$dg_{t-t_0} = \sum_{k=1}^{N} dg^k_{t-t_0} \quad (3.3)$$

3.3 Results

3.3.1 Steady state conditions

The effect of the fumarole inclination on steady state conditions is shown on Figure 3.3. Regardless of the fumarole inclination, the hydrothermal plume comprises a dry-gas region surrounded by a two-phase region and develops above the injection area at depth. The hydrothermal plume is therefore symmetric around the fumarole outlet in the case of a vertical fumarole only.

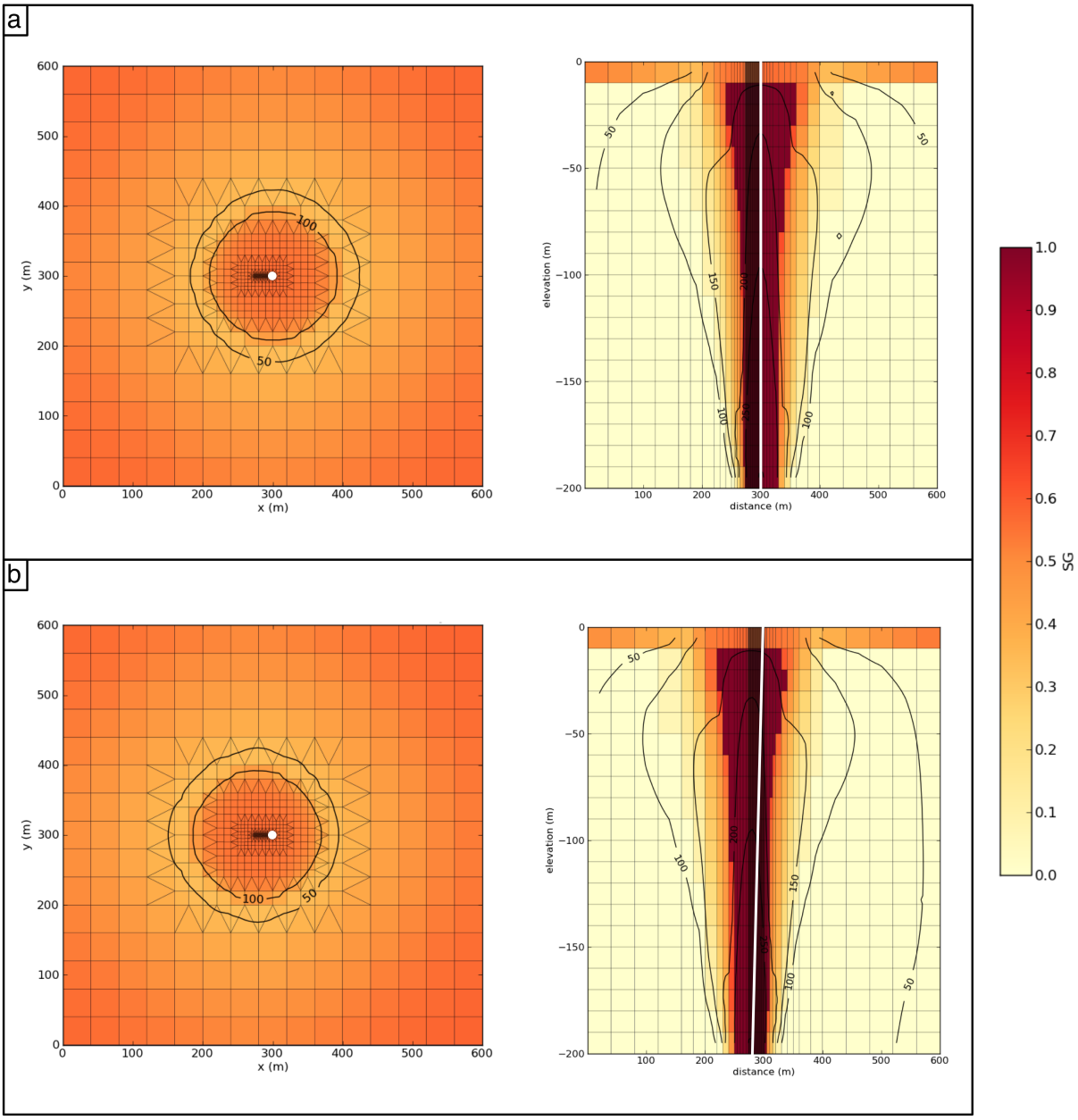

Figure 3.3: Gas saturation (colours) and temperature (contours) at steady state in cross section (left) and map view (right) for two fumarole inclinations from the vertical (a) 0°, (b) 7°. The white dot and white line in the map views and cross sections, respectively, indicate the location of the fumarole.

The fumarole affects the hydrothermal plume compared to a similar simulation within a homogeneous domain. Figure 3.4) shows a greater gas saturation and temperature at the edges of the hydrothermal plume for the homogeneous case, implying that the effect of the fumarole is to narrow the hydrothermal plume, consistent with previous studies (e.g., Todesco et al., 2010). The centre of the hydrothermal plume has a smaller temperature in the homogeneous case, indicating that the effect of the fumarole is also to increase the temperature within the conduit.

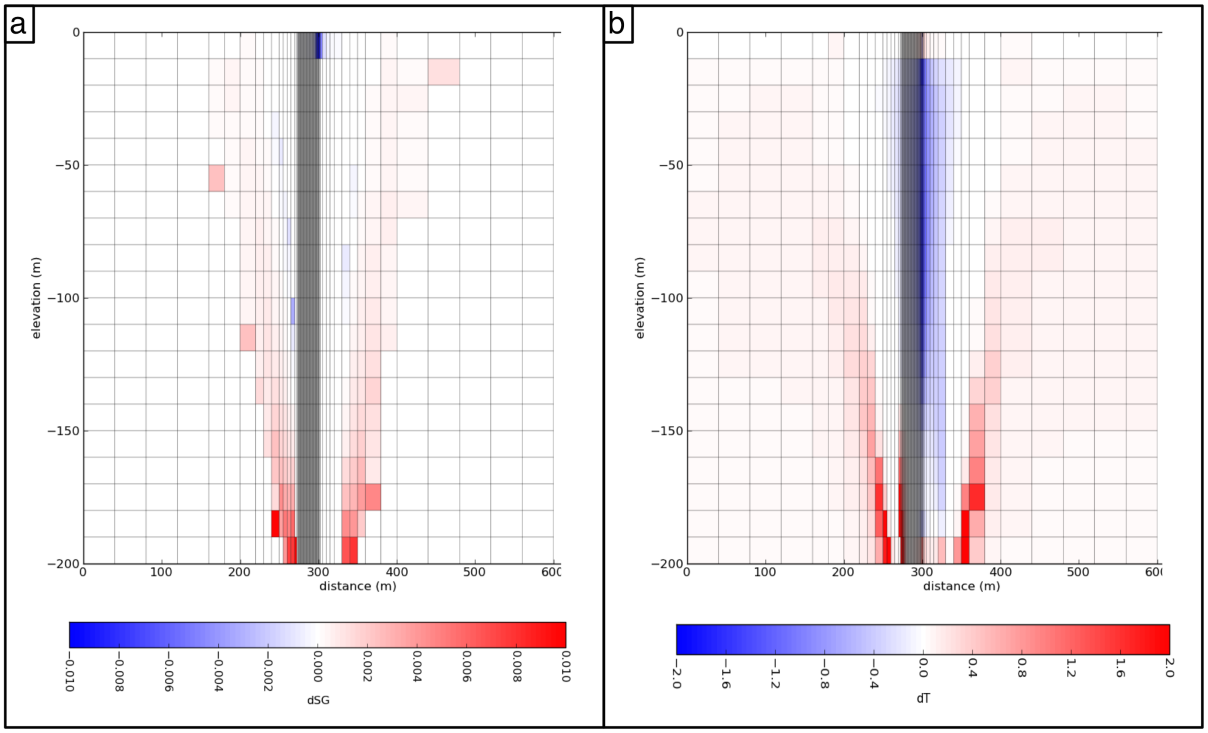

Figure 3.4: (a) Gas saturation difference and (b) temperature difference, at steady state, between the homogeneous and heterogeneous simulation (with a vertical fumarole).

3.3.2 Evolution of hydrothermal circulation and gravity associated with an unrest period

Here, we describe the results for a vertical and an inclined fumarole conduit that are subject to a 1-year long period of unrest (with increased injection rate, temperature, and CO_2/H_2O ratio) followed by a quiet period until the system returns to steady state conditions (refer to Table 3.2 for the characteristics of each period).

The general evolution of gravity changes with time and the amplitude of the changes are not strongly affected by the inclination of the fumarole. First, in the vicinity of the fumarole outlet (within a 200 m radius) and regardless of the fumarole inclination, gravity decreases almost linearly during the unrest period and the 3 months following the end of this unrest, and increases during the quiet period to reach back steady state conditions (Figure 3.5). Conversely, at the edges of the domain (e.g., x = 100 m and x = 500 m), the unrest period is characterised by a general gravity increase during the unrest, and the quiet period by a gravity decrease. Second, the maximum gravity decrease is not observed at the fumarole outlet, consistent with previous studies (e.g., Todesco et al., 2010), and the gravity recovery slows down with time with most

of the changes occurring within 2 years of the end of the unrest period. Finally, the amplitude of the observed gravity changes are similar regardless of the fumarole inclination: maximum gravity decrease of ∼60 μGal, maximum gravity increase of ∼180 μGal.

The fumarole inclination affects the spatial distribution of the gravity anomaly. First, the gravity changes are symmetric from the fumarole outlet for the simulation with a vertical fumarole only i.e., a similar gravity evolution is observed on both sides of the fumarole outlet (Figure 3.5 a). Second, on the right of the fumarole outlet (x > 300 m), the fumarole inclination shifts the location of the maximum gravity decrease to x = 350 m (instead of x = 400 m when the fumarole is vertical). Third, the gravity increases throughout the whole unrest episode for locations right of the outlet for the inclined fumarole only. Conversely, gravity starts to decrease slightly 2 months before the end of the unrest for the vertical fumarole (-2 μGal). This gravity decrease is stronger for the sites left of the outlet of the inclined fumarole (-14 μGal) and starts earlier (5 months before the end of the unrest).

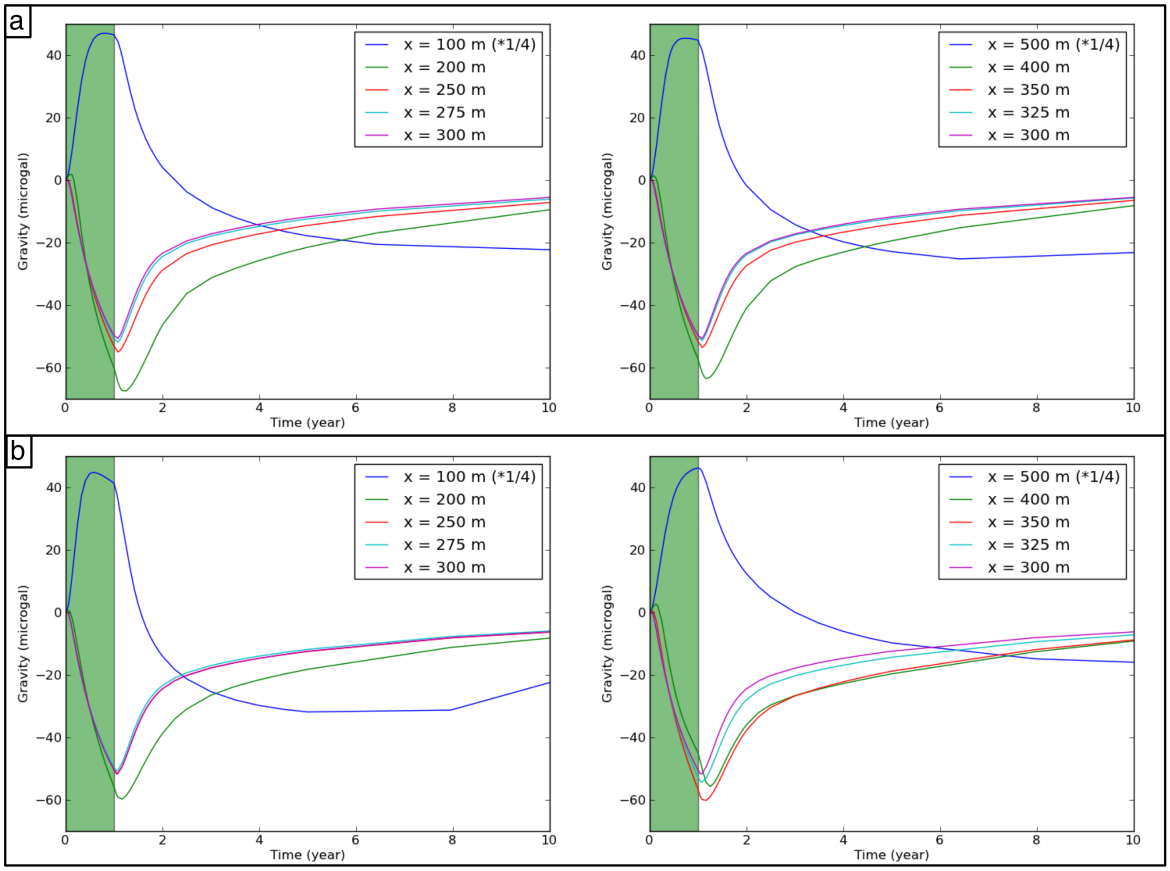

Figure 3.5: Temporal evolution of gravity changes at the surface for different distances along the profile y = 300 m, corresponding to the sequence of unrest and quiet periods described in Table 3.2; for the simulations with different fumarole inclinations (a) 0°, (b) 7°. The green area defines the timing of the unrest period. Left and right panels correspond to observations at x $<$ 300 m and x $>$ 300 m respectively. Note the symmetry of the gravity change from the outlet (x = 300 m) in the case of a vertical fumarole only.

During the unrest phase, more gas enters the domain and pushes the liquid water outwards and upwards (Figure 3.6), consistent with previous studies (e.g., Todesco et al., 2010; Christenson et al., 2010). This enlargement of the two-phase hydrothermal plume leads to a gravity decrease close to the fumarole (within a 100 m radius, where gas replaces liquid), and to a gravity increase further away (where more liquid water is present at shallow depth). Most of the density changes occur in the shallowest layer of the domain (10 m) and at the edge of the two-phase hydrothermal plume. The gravity decrease is due to the gas saturation increase (and a density decrease) at the edge of the two-phase hydrothermal plume. Because gravity is more sensitive to density changes close to the observation location, the maximum gravity decrease ($\sim$60 μGal) is observed at the location where the two-phase hydrothermal plume reach (or is very close

to) the surface (∼100 m away from the fumarole injection area). The top layer of the domain further away from the fumarole injection area (outside the >100 m radius) is initially close to be gas saturated (Figure 3.3). The inflow of liquid water towards this region therefore leads to a gas saturation decrease (and a density increase), explaining the observed gravity increase at the surface. Because the density changes occur mainly at the edge of the two-phase hydrothermal plume which is centred around the injection area, the gravity field is also centred around the fumarole injection area, and not the fumarole outlet.

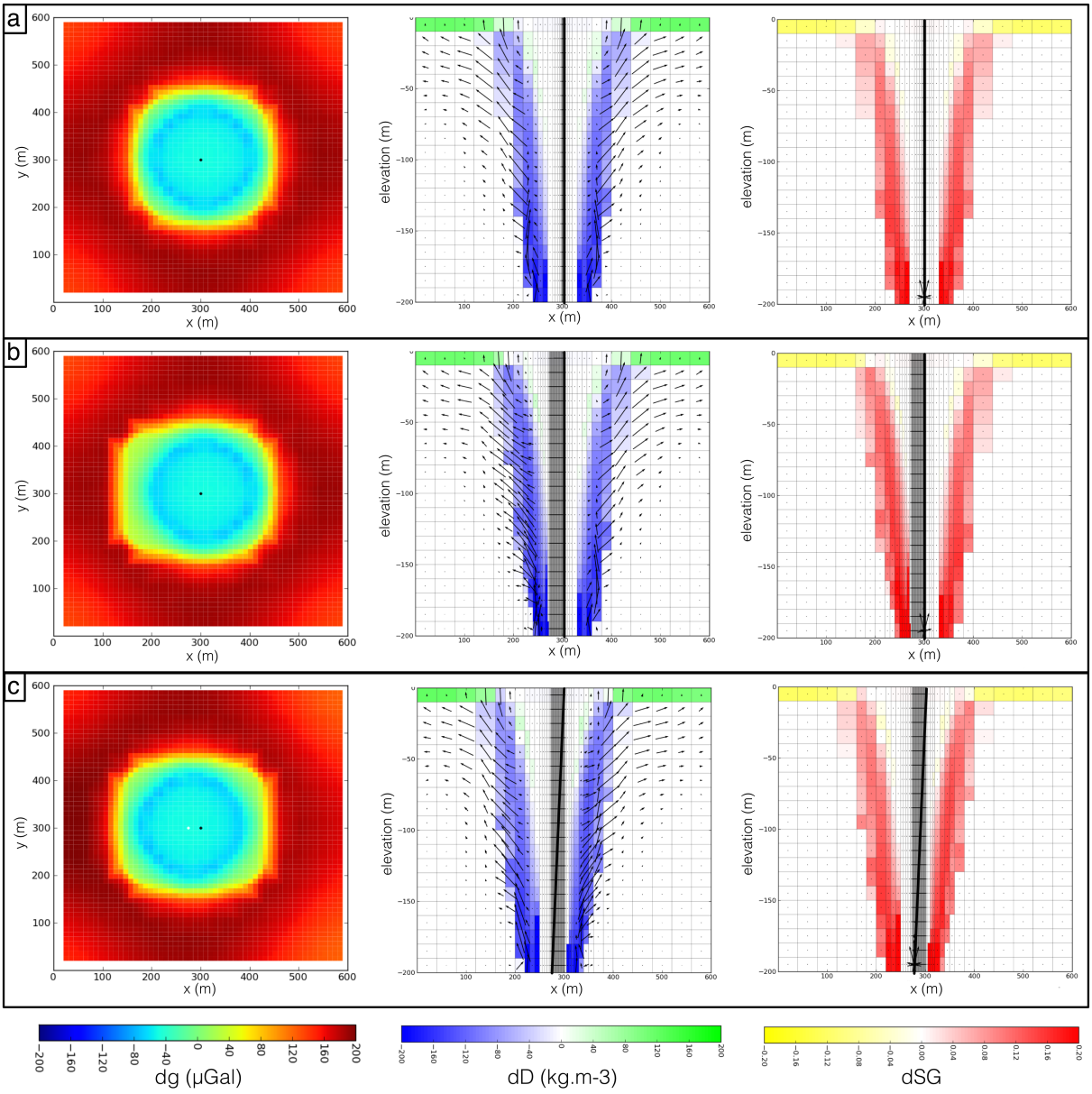

Figure 3.6: Changes in several parameters between the initial conditions and 1 year of the simulation (end of the unrest period) for three simulations with different meshes and fumarole inclinations from the vertical (a) 0° with a simple mesh, (b) 0° with the reference mesh, (c) 7° with the reference mesh. Each panel shows: a map view of the gravity changes, linearly interpolated on a 10-m regular grid (left), a cross section of the density changes with the liquid flow pattern (centre), a cross section of the gas saturation changes with the gas flow pattern (right). Flows are extracted at the middle of the period i.e., after 6 months of simulation. On the gravity maps, the black dot shows the location of the fumarole outlet, the white dot for the simulation with an inclined fumarole shows the location of the injection source. On the cross-sections, the black line indicates the location of the fumarole conduit.

Gravity at the surface continues to decrease close to the fumarole outlet for the 3 months following the end of the unrest because the injection rate decrease only affects the deep part of the domain during that period (Figure 3.7). Liquid water is driven towards the fumarole close to the injection source while the excess gas injected during the unrest keeps expanding at shallow depths. Because gravity at the surface is more sensitive to shallow density changes, the shallow effect of the gas pocket overprint the changes at the source close to the fumarole outlet.

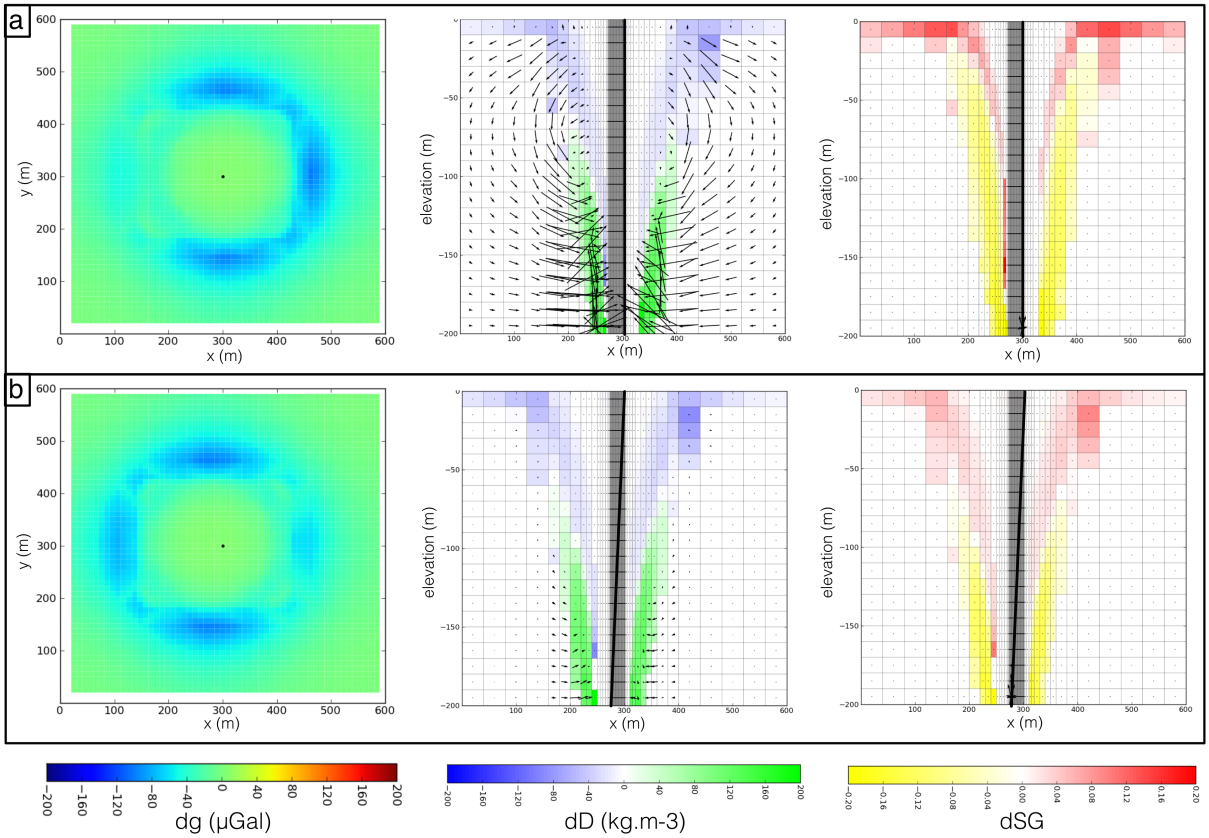

Figure 3.7: Changes in several parameters between 1 year (end of the unrest) and 1.25 years for two simulations with different fumarole inclinations from the vertical (a) 0°, (b) 7°. Each panel shows: a map view of the gravity changes, linearly interpolated on a 10-m regular grid (left), a cross section of the density changes with the liquid flow pattern (centre), a cross section of the gas saturation changes with the gas flow pattern (right). Flows are extracted at the middle of the period i.e., after 1.125 months of simulation and are not plotted on the same scale for better visualisation. On the gravity maps, the black dot shows the location of the fumarole outlet, the white dot for the simulation with an inclined fumarole shows the location of the injection source. On the cross-sections, the black line indicates the location of the fumarole conduit.

From 3 months after the end of the unrest onwards, the amplitude of the gravity changes gradu-

ally returns to zero, reflecting the evolution of the gas saturation and density within the domain towards steady state (Figure 3.8; 3.9 and 3.10). The gravity changes between 1.25 and 2 years of simulation (just after the unrest, Figure 3.8) show a reverse trend from those observed during the unrest episode: the gravity increases slightly around the fumarole and decreases further away. Again, most of the gas saturation and density changes occur within the top layer and at the edge of the two-phase hydrothermal plume. However, the deep part of the plume is more affected by these changes than the shallow part. The pressure drop due to the injection rate decrease drives liquid water towards the fumarole, decreasing the gas saturation at the edge of the two-phase hydrothermal plume. The excess gas injected during the unrest ascends towards the surface and is responsible for the gas saturation increase observed at shallow depths around the fumarole. The heat plume ascending with the gas plume likely contributes to the increased gas saturation at shallow depths, whereby heat is transferred onto the rock, and then released with ongoing convection (the convective sweep process in Christenson et al. (2010)). The gravity increase at the surface around the fumarole indicates that the shallow density decrease at the inner edge of the plume has little effect on the gravity compared to the more widespread density increase due to the inflow of liquid water. A convection cell develops in the upper part of the domain (top 100 m), whereby liquid water flows from the surface towards the fumarole. As for the unrest period, the gravity field at the surface is off-centred from the fumarole outlet when the fumarole is inclined, whereas it is symmetric around the outlet when the fumarole is vertical.

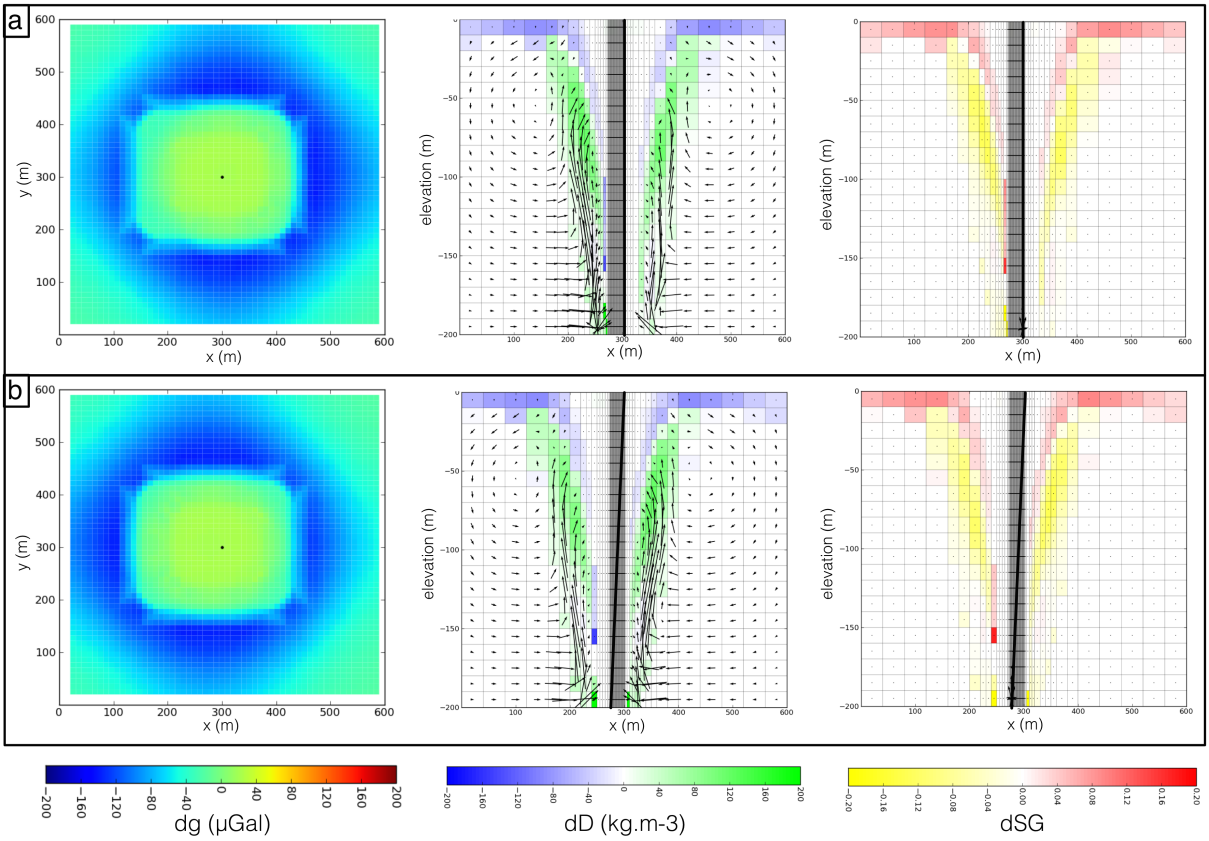

Figure 3.8: Changes in several parameters between 1.25 and 2 years for two simulations with different fumarole inclinations from the vertical (a) 0°, (b) 7°. Each panel shows: a map view of the gravity changes, linearly interpolated on a 10-m regular grid (left), a cross section of the density changes with the liquid flow pattern (centre), a cross section of the gas saturation changes with the gas flow pattern (right). Flows are extracted at the middle of the period i.e., after 1.625 months of simulation. On the gravity maps, the black dot shows the location of the fumarole outlet, the white dot for the simulation with an inclined fumarole shows the location of the injection source. On the cross-sections, the black line indicates the location of the fumarole conduit.

The subsequent gravity changes follow the same pattern but are of smaller amplitude, reflecting the smaller gas saturation and density changes within the domain, as the excess gas slowly escapes the system. Large convection cells develop (e.g., Figure 3.9), with liquid water pushed upwards and outwards of the fumarole area at shallow depths (top 125 m), with recharge at greater depths. We observe a gravity increase around the fumarole, delineating the edge of the two-phase hydrothermal plume, whereas minor changes occur inside that plume. In contrast to what was observed during the previous period (between 1.25 and 2 years of simulation), the shallow part of the two-edge plume is more affected by the changes than the deep part between

2 and 5 years of simulation, reflecting the location of the gas pocket injected during the unrest. The subsequent changes are of smaller amplitude (Figure 3.10) reflecting the re-establishment of the steady state conditions.

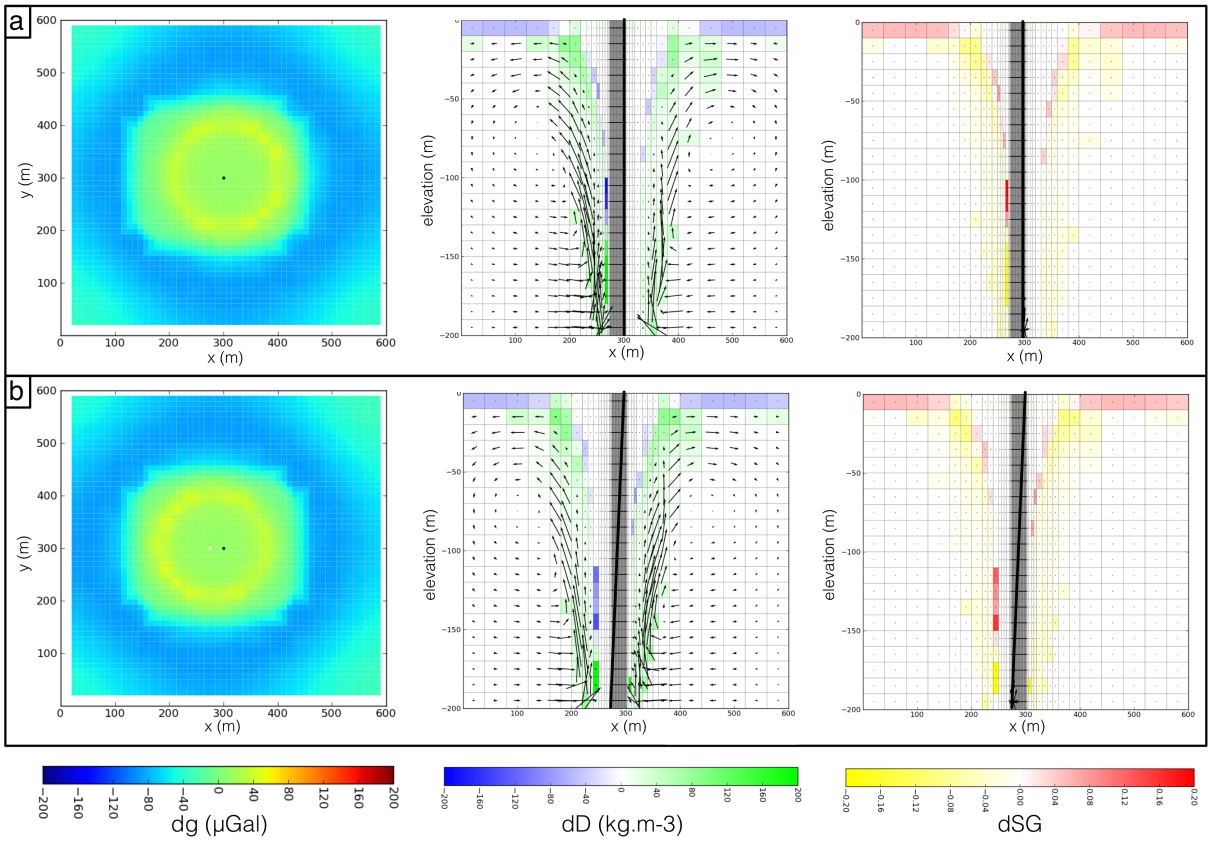

Figure 3.9: Changes in several parameters between 2 and 5 years for two simulations with different fumarole inclinations from the vertical (a) 0°, (b) 7°. Each panel shows: a map view of the gravity changes, linearly interpolated on a 10-m regular grid (left), a cross section of the density changes with the liquid flow pattern (centre), a cross section of the gas saturation changes with the gas flow pattern (right). Flows are extracted at the middle of the period i.e., after 3.5 years of simulation. On the gravity maps, the black dot shows the location of the fumarole outlet, the white dot for the simulation with an inclined fumarole shows the location of the injection source. On the cross-sections, the black line indicates the location of the fumarole conduit.

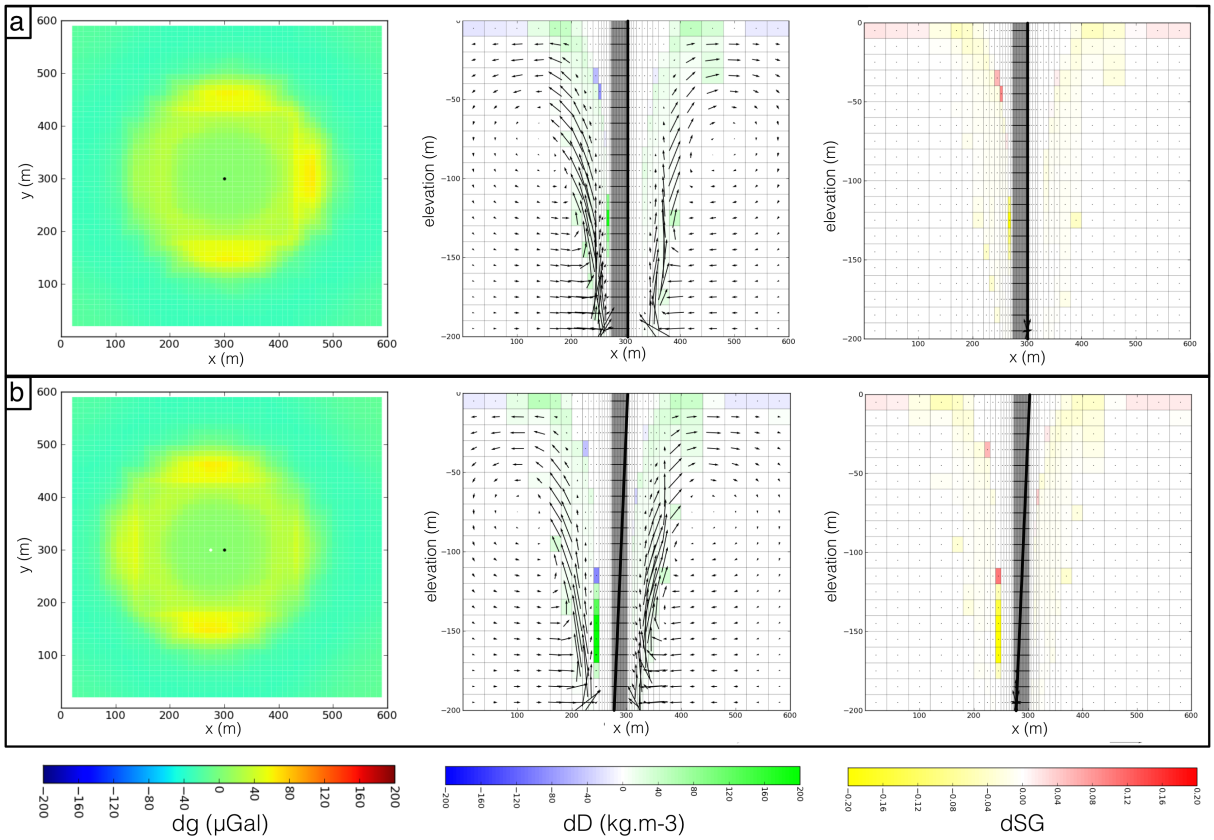

Figure 3.10: Changes in several parameters between 5 and 10 years for two simulations with different fumarole inclinations from the vertical (a) 0°, (b) 7°. Each panel shows: a map view of the gravity changes, linearly interpolated on a 10-m regular grid (left), a cross section of the density changes with the liquid flow pattern (centre), a cross section of the gas saturation changes with the gas flow pattern (right). Flows are extracted at the middle of the period i.e., after 7.5 years of simulation. On the gravity maps, the black dot shows the location of the fumarole outlet, the white dot for the simulation with an inclined fumarole shows the location of the injection source. On the cross-sections, the black line indicates the location of the fumarole conduit.

In summary, the effect of the fumarole inclination on gravity changes at the surface is clearly visible on Figure 3.11 where the difference between two gravity maps (each characterising a fumarole inclination, $g_{inclined}$ - $g_{vertical}$) is plotted for different periods. The gravity to the left of the fumarole outlet is opposite to the gravity to the right of the outlet, suggesting a translation of the gravity anomaly towards the left side of the domain when the fumarole is inclined. During the unrest and to the left of the fumarole outlet, the inclined fumarole leads to a greater gravity increase close to the fumarole (100 m radius, +15 μGal maximum), a strong gravity decrease (< -50 μGal) further away, and a smaller gravity increase at the edge of the

domain. An opposite pattern is observed to the right of the fumarole. Just after the unrest and again to the left of the fumarole, the difference in gravity changes (+25 μGal when the fumarole is inclined) is more diffuse close to the fumarole and might reflect the fact that the density changes occur mainly in the deeper part of the domain (Figure 3.8). Conversely, the difference further away is very sharp and might reflect the fact that the gravity changes in this area are controlled by the density changes in the top layer (10 m thick). Between 2 and 5 years of simulation, the opposite is observed with a less diffuse difference in gravity changes close to the fumarole and a more diffuse one further away, reflecting the fact that most of the density changes occur at shallow depth around the fumarole with minor changes in the top layer further away (Figure 3.9). Between 5 and 10 years of simulation, small gravity differences are observed within 100 m of the fumarole outlet as the system reaches steady state conditions. For the same period, a strong difference in gravity changes ($>$ 50 μGal) is present in a 100 m-wide shell 150 m away from the fumarole reflecting density changes in the top layer of the domain (Figure 3.10).

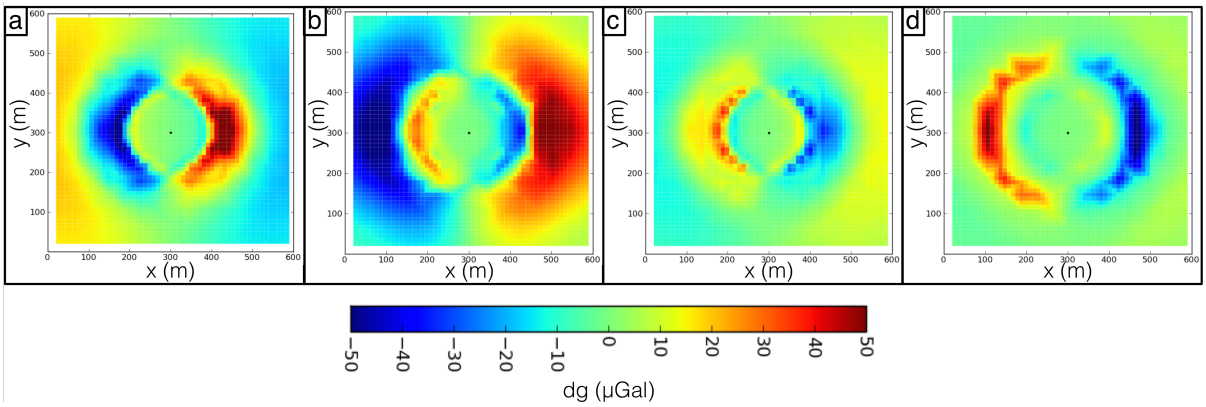

Figure 3.11: Gravity changes difference between the simulations with an inclined and a vertical fumarole, for different periods (a) between initial conditions and 1 year (end of the unrest), (b) between 1 and 2 years, (c) between 2 and 5 years, (d) between 5 and 10 years. The black dot shows the location of the fumarole outlet.

3.3.3 Model limitations

The apparent lateral extension of the gravity anomaly towards the left edge of the domain seems to be related to a mesh effect. Figures 3.6a and b present results from the same physical model with a vertical fumarole, but using different meshes. For the reference mesh which is refined towards the left of the fumarole outlet (Figures 3.1 a and b), the gravity anomaly extends towards this direction (e.g., Figure 3.6b) whereas it is symmetric around the outlet when the mesh is simpler and more regular (Figures 3.1 c and d). The reference mesh is thinner to the

left of the fumarole so the observables will be averaged over a smaller volume, explaining the sharper gravity changes on this side of the fumarole. This suggests that the elongation of the anomaly towards the left edge of the domain is related to the mesh.

This effect is more important at locations outside a 100 m radius from the fumarole outlet where the mesh becomes coarser. Closer to the outlet, we observe the same circular gravity patterns, regardless of the mesh used for the simulation. We are therefore confident that the changes closer to the fumarole (within a 100 m radius) are less affected by the choice of the mesh used for the simulation so that they can be interpreted quantitatively. Conversely, caution must be used when interpreting the changes further away from the outlet.

We finally observe that, for our scenario, the effect of the fumarole on gravity at the surface does not produce a difference of sufficiently high magnitude to be measured in the field, compared to the homogeneous case where no fumarole is present within the domain. For example, Figure 3.12 shows that there is only a maximum of 2 μGal difference for the period associated with the unrest. This demonstrates that the shift of the gravity anomaly towards the injection area in the case of an inclined fumarole is mainly due to the different location of the injection area, and that there is only a minor effect of the fumarole on hydrothermal circulation. A greater permeability contrast between the fumarole and the surrounding medium would likely magnify the effects of an inclined fumarole conduit.

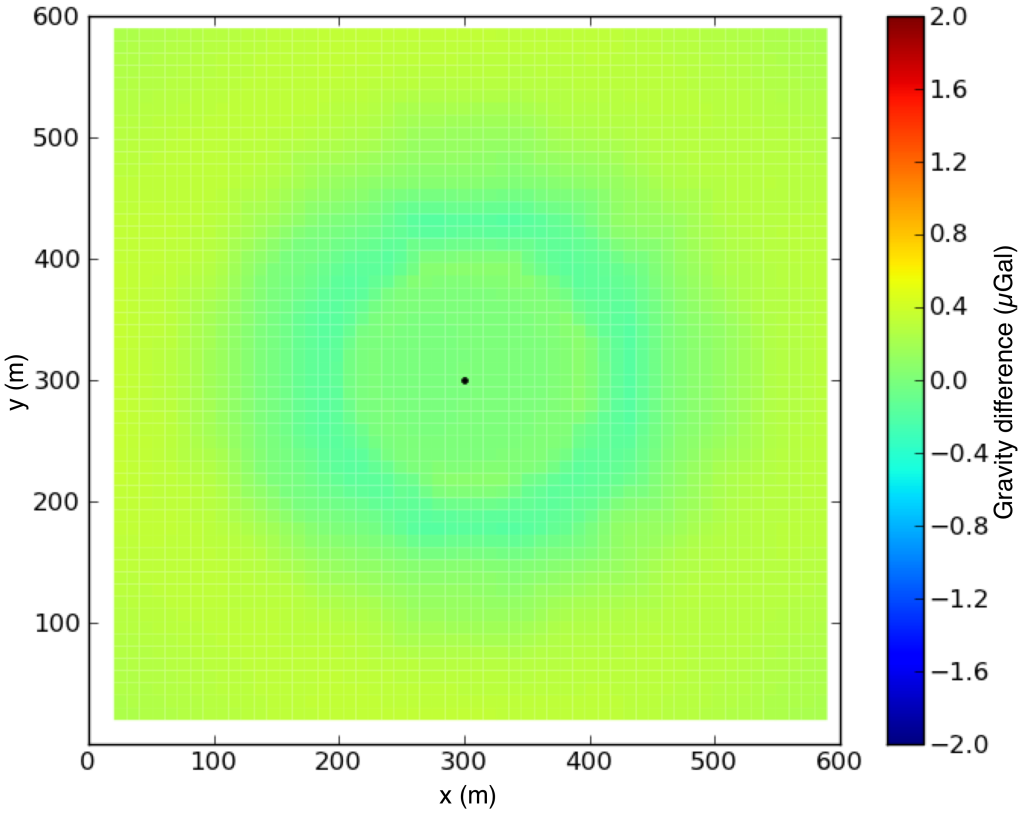

Figure 3.12: Difference in gravity changes (between the end and the unrest and initial conditions), between the homogeneous and heterogeneous simulation (with a vertical fumarole). The black dot shows the location of the fumarole outlet.

3.4 Discussion and Conclusions

We performed several numerical simulations of hydrothermal circulation to investigate the effect of the fumarole inclination on steady state conditions and associated with an episode of unrest. Our model is constrained using parameters consistent with the fumarole 0 area at White Island volcano. We showed that the hydrothermal plume (dry-gas surrounded by a two-phase region) is centred around the fumarole outlet only if the fumarole is vertical. In the case of an inclined fumarole, the hydrothermal plume shifts towards the fumarole injection area at depth. Most of the density changes associated with the unrest episode occur in the two-phase region of the hydrothermal plume (Figures 3.6, 3.7, 3.8, 3.9, 3.10), as shown in earlier studies (Todesco and Berrino, 2005; Todesco et al., 2010), because this region is very sensitive to the amount of gas entering the system i.e., the hydrothermal plume enlarges or shrinks depending on the gas injection rate. When the fumarole is inclined, the edge of this two-phase hydrothermal plume is

not at the fumarole outlet and is off-centre. This implies that gravity measurements can inform the location of the injection source, providing that they are performed in a wide area around the fumarole outlet to capture the two-phase hydrothermal plume surrounding the fumarole conduit.

A gravity decrease is observed at the surface during the unrest period in the vicinity of the fumarole outlet due to the expansion of the dry-gas region. It is of maximum amplitude where the two-phase hydrothermal plume reaches (or is close to) the surface. After the unrest, gravity continues to decrease close to the fumarole during the following 3 months because surface gravity is more sensitive to shallow changes (still reflecting the effect of the excess injected gas and of the thermal plume) than to deep changes (part of the domain first affected by the decreased injection rate). The amplitude of the gravity changes then gradually decrease as the system returns to steady state conditions. The general behaviour of the gravity changes close to the fumarole outlet (gravity decrease during unrest and gravity increase during quiet) are similar to those observed for the most permeable model by Todesco et al. (2010). In our model, the strong gravity changes are observed during the 1 year long period of unrest and during the following year of quiet. This is likely due to the high permeability of the domain which therefore reacts quickly to any change at the source. These results highlight the importance of performing regular gravity measurements (e.g., once a year) or installing continuously recording gravitymeters to capture the rapid evolution of the system.

We emphasised the effect of the mesh refinement around the fumarole on the results. As for any numerical modelling exercise, it is therefore recommended that the mesh effect be thoroughly assessed before interpreting any results.

The results of this study are likely linked to the characteristics of our simulations where the fumarole conduit has a small diameter with a permeability only an order of magnitude higher than the surrounding medium. Moreover, due to computational constraints, we only studied the effect of a small fumarole inclination. This high permeable conduit therefore does not affect the flow strongly and most of the observed changes are similar to those expected in the homogeneous case, where the plume is located above the injection source. More simulations with (1) different permeability contrasts between the fumarole zone and the embedding medium, (2) more inclined fumaroles and (3) larger fumarole conduits are recommended to further constrain the effect of the fumaroles on monitoring observables.

Our results could help the interpretation of gravity changes observed at volcanoes with active fumarolic activity. Several studies emphasise hydrothermal processes as likely sources for the recorded gravity changes (e.g., Solfatara (Bruno et al., 2007); Nisyros (Gottsmann et al., 2005;

Gottsmann et al., 2007), Tenerife (Gottsmann et al., 2006); White Island (see Chapter 2 of this thesis), Campi Flegrei (Battaglia et al., 2006; Berrino, 1994). Gravity changes in such settings can be of several tens of μGal over a range of timescales (from minutes to years). For example, significant short-term gravity variations (tens of μGal over tens of minutes) were observed at Nisyros (Gottsmann et al., 2005; Gottsmann et al., 2007) and were attributed to degassing instabilities. Together with the potential complex processes at play, the limited constraint on the properties and geometries of permeable pathways and fluid dynamics in volcanic areas makes the interpretation of gravity changes challenging. The fault zones -acting as preferential pathways for fluid migration- can be numerous and complex (e.g., Solfatara (Bruno et al., 2007); Tenerife (Gottsmann et al., 2008)). It is unlikely that fumarole conduits are vertical because these permeable structures usually follow discontinuities within volcanoes, such as crater boundaries. We showed that the gravity anomaly is not necessarily centred around the fumarole outlet, and mainly reflects changes close to the location of the magmatic fluids injection, depending on the fumarole characteristics (dimensions, rock properties). This suggests the need to better account for the potential contribution of the inclination of fumarole conduits to the location of gravity anomalies.

For the fumarole zero area at White Island, we conclude that a conduit of small diameter (as observed at the surface) with a permeability one order of magnitude higher than the surrounding medium (consistent with laboratory measurements) would narrow the two-phase hydrothermal plume but would not lead to measurable gravity changes at the surface compared to an homogeneous medium. The effect of an inclined conduit where the injection source is shifted from the fumarole outlet is similar to that where no conduit is present with the injection source shifted from the outlet. The location of the gravity anomaly would therefore be centred around the injection source. Deformation measurements suggest that the injection area of fumarole zero is a few hundred of metres away from the fumarole outlet (Fournier and Chardot, 2012). If our model is indeed representative of the fumarole zero conditions, we would therefore expect the gravity anomaly to be off-centre from the fumarole outlet by the same amount.

Preamble

Chapters 2 and 3 focused on the source of magnetic and gravity changes to help constrain an unrest period (2011-2012) at White Island. Chapter 2 demonstrated that magnetic changes and the lack of significant gravity changes at the surface are consistent with an episode of increased degassing possibly associated with the rise of small intrusion. An episode of increased degassing was then modelled in Chapter 3 to assess the effect of the fumarole conduit inclination on gravity changes at the surface. Understanding the effect of structural features on geophysical changes is indeed necessary close to the fumarole to shed light on the unrest source. These two previous chapters therefore constrained the source of the 2011-2012 unrest. However, they did not integrate seismicity into the interpretation nor inform on the likelihood of an eruption. This will be tackled in the next chapter. I will analyse whether increasing levels of volcanic tremor can be precursory for the eruptions recorded in 2012 and 2013 at White Island, so that they can be used for eruption forecasting. This chapter will therefore answer the final three research questions of this thesis (Table 1.1) in order to reach the final objective of this research set in the introduction chapter ("To assess the potential of using increasing levels of volcanic tremor to forecast eruptions at White Island to determine the tremor characteristics that are precursory for eruptions at the volcano"). This chapter has been published in a peer-reviewed journal: **Chardot, L.**, Jolly, A. D., Kennedy B.M., Fournier, N., Sherburn, S. 2015. *Journal of Volcanology and Geothermal Research*, 302(C), 11-23. doi:10.1016/j.jvolgeores.2015.06.001.

Chapter 4

Using volcanic tremor for eruption forecasting at White Island volcano (Whakaari), New Zealand

Abstract

Eruption forecasting is a challenging task because of the inherent complexity of volcanic systems. Despite remarkable efforts to develop complex models in order to explain volcanic processes prior to eruptions, the material Failure Forecast Method (FFM) is one of the very few techniques that can provide a forecast time for an eruption. However, the method requires testing and automation before being used as a real–time eruption forecasting tool at a volcano. We developed an automatic algorithm to issue forecasts from volcanic tremor increase episodes recorded by Real–time Seismic Amplitude Measurement (RSAM) at one station and optimised this algorithm for the period August 2011–January 2014 which comprises the recent unrest period at White Island volcano (Whakaari), New Zealand. A detailed residual analysis was paramount to select the most appropriate model explaining the RSAM time evolutions. In a hindsight simulation, four out of the five small eruptions reported during this period occurred within a failure window forecast by our optimised algorithm and the probability of an eruption on a day within a failure window was 0.21, which is 37 times higher than the probability of having an eruption on any day during the same period (0.0057). Moreover, the forecasts were issued prior to the eruptions by a few hours which is important from an emergency management point of view. Whereas the RSAM time evolutions preceding these four eruptions have a similar goodness–of–fit with the FFM, their spectral characteristics are different. The duration–amplitude distributions of the precursory tremor episodes support the hypothesis that several processes were likely occurring prior to these eruptions. We propose that slow rock failure and fluid flow processes are plausible candidates for the tremor source of these episodes. This hindsight exercise can be useful for

future real–time implementation of the FFM at White Island. A similar methodology could also be tested at other volcanoes even if only a limited network is available.

4.1 Introduction

One of the ultimate goals of most volcanological studies is to forecast volcanic eruptions. However, only a few quantitative methods have been developed so far to do so. The material Failure Forecast Method (FFM), based on a general law of material failure proposed for volcanoes by Voight (1988) allows forecasting of a failure time from precursory activity. It is derived from previous studies on slope stability (Fukuzono, 1985 and Fukuzono and Terashima, 1985) where accelerating displacement of inclined soil layers due to constant loading (from rainfall) was observed prior to slope failure. According to Voight (1988); the approach can be extended to volcanic eruptions where material failure is due to magma pressurisation. If the evolution of a geophysical parameter Ω is a precursor for failure, an empirical power law links the rate of change of Ω $\left(\frac{d\Omega}{dt}\right)$ to its acceleration $\left(\frac{d^2\Omega}{dt^2}\right)$ (Equation 4.1).

$$\frac{d^2\Omega}{dt^2} = A\left(\frac{d\Omega}{dt}\right)^{\alpha} \tag{4.1}$$

where A and α are constants. Because an eruption starts when there is no longer resistance to magma ascent, predicting the loss of resistance to magma ascent informs on the likelihood of an eruption. This loss of resistance corresponds to an uncontrolled rate of change (i.e., when $\left(\frac{d\Omega}{dt}\right)$ becomes infinite). Studying how the rate of change approaches this condition is the key principle behind the FFM.

The complexity of precursory activity prior to eruptions makes eruption forecasting often challenging. As such, only a few successful forecasts have been made in foresight with the FFM (e.g., Colima (De la Cruz-Reyna and Reyes-Davila, 2001; Reyes-Davila and De la Cruz-Reyna, 2002), Villarrica (Ortiz et al., 2003); Tungurahua (Tarraga et al., 2004); El Hierro (Garcia et al., 2014)). The FFM has also been applied successfully in hindsight at numerous volcanoes (e.g., Mount St Helens (Voight and Cornelius, 1991); Redoubt (Cornelius and Voight, 1994); Pinatubo (Cornelius and Voight, 1996); Montserrat (Kilburn and Voight, 1998)). Tarraga et al. (2008) pointed out that the geophysical observable used in the FFM is an indirect measure of the state of the system, which results from the interaction of magma with the superficial system of fractures and/or the hydrothermal system. The forecast event may therefore not always be an eruption, but a change in state, such as tectonic faulting or gas flux or composition. Because of these complex interactions, forecasts are often inaccurate (Bell et al., 2013). They also very often rely on the visual pattern recognition by experienced scientists (e.g., Cornelius and

Voight, 1994; Kilburn and Voight, 1998) which can potentially lead to bias in the forecasts. It is therefore preferable to express these forecasts in probabilistic terms to take into account the inherent uncertainties (Sparks, 2003).

Several studies demonstrated the importance of isolating a part of the signal to produce reliable forecasts. Kilburn (2003) proposed that the main pathway for magma ascent is formed by multiscale fracturing allowing the coalescence of pre-existing cracks in the volcanic conduit and demonstrated that this mechanism obeys Equation 4.1 with $\alpha = 2$. This model implies that the acceleration of the geophysical parameter is composed of shorter accelerating trends, whose detectability depends on the seismic network. The author recommends studying the peak event rate to depict the propagation of the main fracture, instead of the whole dataset. Hammer and Neuberg (2009) demonstrated that the the average low-frequency event rate per swarm followed the material failure law (Equation 4.1) allowing the estimation of the 1997 dome collapse at Montserrat volcano. Boue et al. (2015) also showed that the automatic seismic event classification may allow the timely assessment of accelerating seismicity. They obtained reliable forecasts for the 2005 eruptions at Colima from a single phase acceleration of low frequency seismic events.

Volcanic tremor can be used as a geophysical precursor to forecast eruptions. It is a continuous seismic signal of volcanic origin (Carniel, 2010). Changes in tremor amplitude and frequency content can characterise several regimes (e.g., Ripepe et al., 2002; Harris et al., 2005; Carniel, 2014), and their detectability depends on the seismic network. Volcanic tremor often precedes and / or accompanies volcanic eruptions (Konstantinou and Schlindwein, 2002 and references therein), with the size of the eruption usually related to the tremor amplitude (McNutt, 1992). As such, tremor amplitude alarm systems were developed (e.g., Qamar et al., 2008; D'Agostino et al., 2013), emitting an alarm when the tremor amplitude exceeds a certain threshold. However, these methods don not provide an eruption time which is one of the benefits of the FFM. In this paper, we focus on the predictability of eruptions using volcanic tremor at White Island volcano (New Zealand) by optimising the automation of the FFM on volcanic tremor recorded during the August 2011–January 2014 period, which comprises the recent unrest / eruptive phase. Building on previous efforts to automate the FFM (Tarraga et al., 2006) to remove any subjectivity in the forecast procedure, we use the entire period between 1 August 2011 and 1 January 2014 to optimise our detection algorithm and attempt to reconcile the FFM with tremor models at White Island volcano. We first give an overview of the volcanic activity during the period of interest. Next, we introduce our method to issue automatic eruption forecasts from volcanic tremor amplitude increases and describe how the method is optimised using volcanic

tremor (2–5 Hz RSAM) recorded during the same period. We then summarise the performance of the method within a robust statistical framework. Finally, we integrate results from classical methods of tremor source characterisation and consider appropriate tremor source models that may explain our observations.

4.1.1 White Island volcano

White Island volcano (Figure 4.1) has a complex volcano-hydrothermal system that produces a wide variety of signals. The stratovolcano is composed of coherent fractured lava flows, breccias, agglomerates and variably consolidated beds of ash lapilli and blocks (Black, 1970; Heap et al., 2015). In a recent seismic study, Jolly et al. (2012) showed that the shallow part of the crater floor has low seismic velocities ($\sim$ 1300 m/s) and is very attenuating ($Q < 5$), suggesting the presence of unconsolidated material below the crater floor, while the crater walls have a higher velocity ($>$ 2200 m/s). A well–developed volcano–hydrothermal system (Giggenbach and Glasby, 1977) is located in the upper kilometer of the edifice under the Main Crater (Nishi et al., 1996). It is expressed at the surface by fumaroles, hot springs, and an acidic crater lake with fluctuating level and temperature that has persisted since 2003 (Scott et al., 2004). The volcano has a history of long periods of fumarolic and hydrothermal activity, with a major magmatic episode occurring between 1976 and 1982 (Houghton and Nairn, 1989a). This activity has also been punctuated by phreatic and phreatomagmatic eruptions (Cole and Nairn, 1975) and by strombolian eruptions as in 1979, 1980 and 2000. Magma feeding these eruptions is thought to originate from different reservoirs located at 500 m, 1–2 km and 2–7 km depth (Clark and Otway, 1989; Houghton and Nairn, 1989a; Cole et al., 2000). During quiescent activity (Figure 4.1; photo), a variety of parameters are monitored, including persistent degassing of CO_2 and SO_2 (Werner et al., 2008; Bloomberg et al., 2014), low level seismicity with spasmodic volcano-tectonic earthquakes (Nishi et al., 1996); a few low–frequency earthquakes per day and episodes of harmonic and non–harmonic tremor (Sherburn et al., 1998); and localised ground surface deformation reflecting shallow interactions between hot magmatic fluids and the hydrothermal system (Peltier et al., 2009; Fournier and Chardot, 2012). Periods of magmatic unrest are often preceded and / or accompanied by increased emissions of magmatic gas (Giggenbach and Sheppard, 1989); elevated seismicity (Latter et al., 1989; Sherburn et al., 1996; Sherburn et al., 1998) and local uplift episodes (Clark and Otway, 1989). The volcano is continuously monitored by GeoNet / GNS Science. While it is uninhabited, it is a major tourist attraction in New Zealand with over 13,000 visitors per year. Enhanced eruption forecasting capabilities are therefore of

paramount importance to reduce the risk of injury or death.

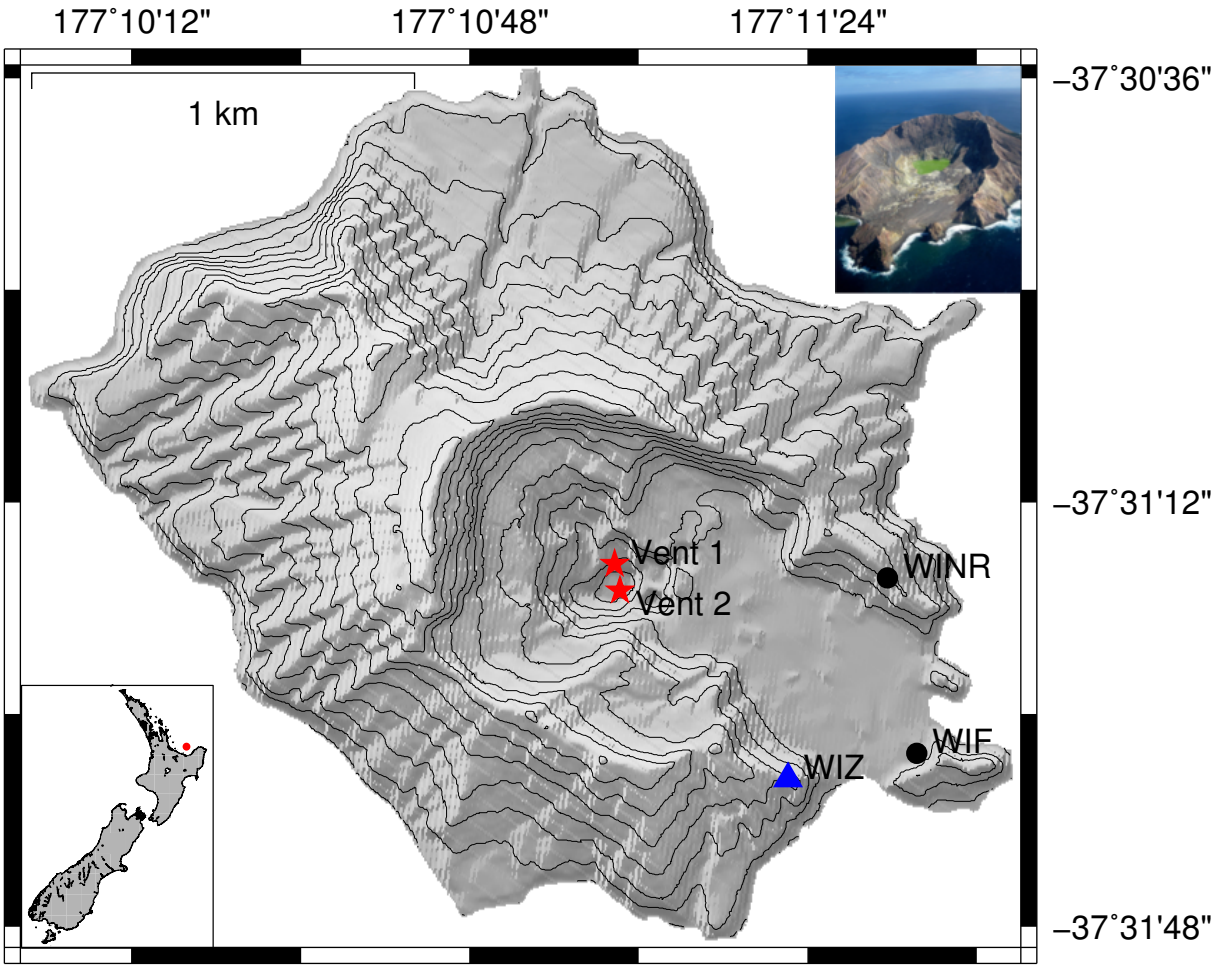

Figure 4.1: Map of White Island volcano with the location of: the WIZ continuous seismic station (blue triangle) whose RSAM data are analyzed in this study, the two continuously recording webcams (black circles) used to constrain surface activity, the active vents of the studied unrest episode between 1 August 2011 and 1 January 2014 (red stars). The bottom left corner insert shows the location of White Island (red dot) relative to New Zealand. The top right corner insert shows the volcano during quiescent period (photo: Lauriane Chardot, GNS Science / EQC). The green area is the crater lake.

Increasing levels of volcanic tremor have often been linked to eruptive activity at White Island (Sherburn et al., 1998). During the 1976–82 eruptive sequence, strong tremor episodes were thought to result from the interaction between magma and groundwater (Latter et al., 1989). In 1991, a period of strong harmonic tremor was followed by non–harmonic tremor, the latter being associated with shock waves at the surface. Sherburn et al. (1996) proposed that the har-

monic part was due to the vibration of a gas-saturated magma conduit during magma ascent whereas the non–harmonic part reflected bubble bursting when the magma reached the surface. Harmonic tremor would then be related to sub–surface processes and non–harmonic tremor to very shallow and / or superficial processes (Sherburn et al., 1998); the latter further supported by the fact that non–harmonic tremor is also observed during periods of crater lake formation (Werner et al., 2008). The recent unrest / eruptive period provides another example of tremor activity associated with surface changes. For example, an eruption on 4 August 2012 was preceded by several days of increased tremor. Testing the FFM on volcanic tremor is therefore justified by its frequent occurrence.

4.2 Seismic and visual observations: White Island, August 2011-January 2014

Seismic data presented in this study are 10–min averaged velocity RSAM (Real-time Amplitude Measurement (Endo and Murray, 1991)) from a continuous GeoNet seismic broadband station (WIZ) located on the crater rim of White Island volcano (Figure 4.1). The WIZ station was installed in 1976 and has recorded numerous episodes of volcano seismicity (Sherburn et al., 1996; Sherburn et al., 1998). It is currently equipped with a three–component Guralp CMG-3ESP broadband sensor recording at 100 Hz and telemetered to the mainland, with a flat velocity response between 0.033 and 50 Hz. The vertical component only is used for computing the RSAM and is bandpass–filtered between 2 and 5 Hz which is well within the flat response of the sensor. The same processing could therefore be applied to seismic data from short-period instruments. The bandpass filter was chosen based on experience from past activity at White Island to reflect tremor activity rather than microseisms (frequencies < 2 Hz) or weather effects (broad spectrum with frequencies up to 20 Hz). The seismic record is then given in velocity units by deconvolving the instrument response. Finally, the RSAM is computed by averaging the absolute velocity amplitude over a 10–min time window (Endo and Murray, 1991). Whereas filtered RSAM is commonly referred to as SSAM (Rogers and Stephens, 1995); we will use 2–5 Hz RSAM when mentioning our data in this manuscript.

We constrain surface activity using acoustic data from the same WIZ location, supplemented by visual observations (webcams and field team visits). Acoustic data are recorded by a Setra pressure transducer model 270 at 100 Hz which has operated since 2002. Visual observations are made by three webcams recording at 1 Hz, two located on the island (WIF, WINR, Figure

4.1) and one on the mainland about 50 km away. A fourth webcam was installed on the western rim of the crater early December 2013 and is not used in this study. Additional routine monitoring visits included site visits to maintain instruments and conduct visual observations to complement information from the webcams.

Seismic and visual observations between 1 August 2011 and 1 January 2014 (UTC as in the rest of the manuscript) at White Island are summarised in Figure 4.2. In hindsight, signs of unrest can be recognised from around 15 August 2011 with some low level tremor activity followed by a lake level drop reported in September 2011. A strong tremor increase occurred on 20–21 June 2012 ($\sim$ 1500 nm/s in about 6 hours) but was not associated with any reported surface activity. Tremor prior to July 2012 occurred during the crater lake level drop. Conversely, a strong tremor episode on 27–28 July 2012 ($\sim$ 1500 nm/s in about 2 hours) was recorded only a few hours before the report of a $\sim$ 5–m rise of crater lake level. An episode of first increasing, then constant, tremor preceded the first eruption of the eruptive phase, on 4 August 2012 at 16:52. This eruption was well recorded by the seismic and acoustic sensors as well as the local webcam (Figure 4.2c) and ejected ash and blocks on the crater floor. Elevated tremor and vigorous ash venting events characterised the activity the following days, evolving to small mud eruptions by the end of August (from Vent 1, Figure 4.1). During this period, the tremor level was strongly varying ($\sim$ 600–2500 nm/s) and the acoustic data were characterised by pulse–like signals typical of explosive activity. Between September and December 2012, volcanic tremor was elevated but showed less variations than in August ($\sim$ 300–1500 nm/s). Strong degassing prevented a direct view of the crater and it is only at the end of November 2012 that a small lava dome was first noticed in Vent 1. From January 2013, the area of the remaining lake (Vent 2, Figure 4.1) became more active. Geysering and bubbling episodes associated with strong variations in volcanic tremor ($\sim$ 40–4500 nm/s) and acoustic activity characterised the activity until early April 2013 (Figure 4.2d). The lake level then rose and the overall volcanic activity decreased slightly until July 2013 when episodes of strong tremor ($\sim$ 80–4000 nm/s) and geysering activity resumed. Four short–lived eruptions were reported on 19 August 22:23 (steam and mud eruption, Figure 4.2e), 4 October 03:35 (steam venting event), 8 October 02:05 (minor steam and mud eruption) and 11 October 07:09 (moderate explosive eruption), during periods of elevated tremor. The deposits of that last eruption blanketed the whole crater floor. The tremor activity finally slowly decreased while the lake level increased. The reader is directed to the GeoNet website for more details on the volcanic activity during this period (www.geonet.org.nz).

The five reported eruptions occurred during elevated tremor, but not at the end of a tremor

increase. Before the 4 August 2012 eruption, tremor increased (to reach $\sim$ 3500 nm/s) from 1 to 3 August 2012 23:40 and remained almost constant for 16 hours. The 19 August 2013 eruption occurred during the decrease in tremor energy following a 1–hour long strong increase ($\sim$ 7000 nm/s) the previous day. A strong tremor increase between 29 September and 3 October ($\sim$ 4300 nm/s) preceded the 4 October eruption but the eruption itself occurred when the tremor level was $\sim$ 1000 nm/s. The 8 October 2013 eruption followed about 3 days of increasing tremor (5–7 October, $\sim$ 3900 nm/s), 1 day of slightly decreasing tremor ($\sim$ 1900 nm/s) then 10 minutes of quiescence (tremor level at $\sim$ 200 nm/s). Finally, the 11 October 2013 eruption occurred during the decrease following a strong tremor increase on 10 October ($\sim$ 1800 nm/s in 5 hours).
Another important observation is that the tremor increases preceding the 4 August 2012, 4 and 8 October 2013 eruptions were composed of shorter increasing then slightly decreasing tremor episodes. This is shown for the 4 August 2012 eruption on Figure 4.2b.

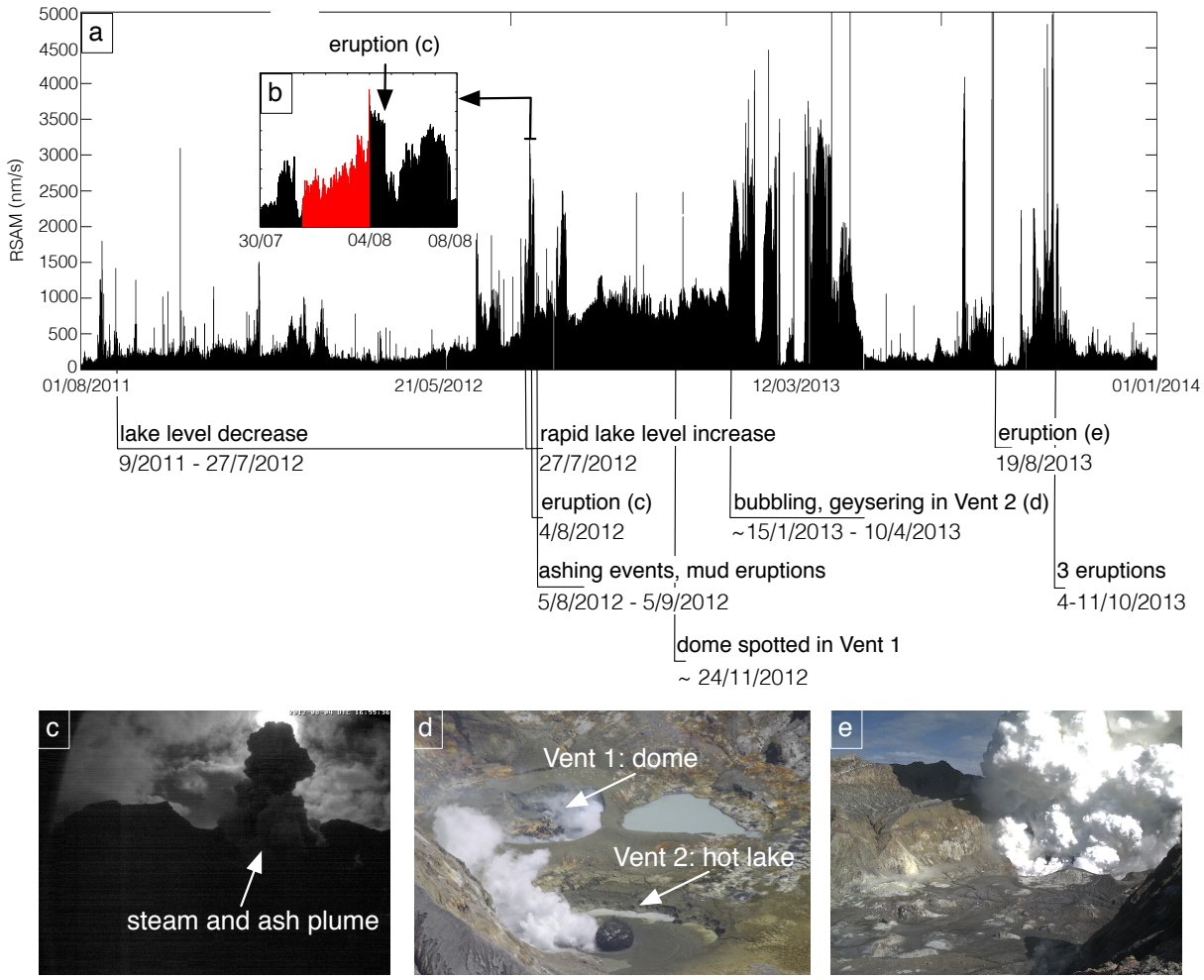

Figure 4.2: RSAM data recorded at WIZ between 1 August 2011 and 1 January 2014 (a) (maximum set to 5000 nm/s for visibility) with timeline of the volcanic activity during the period (date is UTC). The insert (b) is a close–up on the tremor increase preceding the 4 August 2012 eruption: note the several accelerating tremor increases composing the main accelerating trend. The pictures illustrate some examples of volcanic activity that occurred during this period: (c) Overnight eruption on 4 August 2012 showing the ash and steam plume recorded by the WIF webcam, (d) Example of bubbling activity in Vent 2 (black sphere below the arrow) that occurred between January and April 2013 along with the degassing dome area (Vent 1) (photo: Karen Britten, GNS Science / EQC), (e) Strong steam and mud eruption recorded on 19 August 2013 by the WINR webcam (the mud remained confined within the crater).

4.3 Volcanic tremor analysis

We implemented an automated process to first select the RSAM increase episodes to be considered by the FFM, then issue eruption forecasts when the episode bears specific characteristics. Velocity RSAM can be used as a proxy for $\frac{d\Omega}{dt}$ in Equation 4.1 (Tarraga et al., 2008). Although α can be determined for each case study (Cornelius and Voight, 1994); we consistently fixed $\alpha = 2$ for our automated procedure because it is usually close to 2 for volcanic eruptions (Voight, 1988). According to Kilburn (2003); this is consistent with a model where an eruption is the result of the uncontrolled propagation of a crack creating a pathway for magma ascent.
This particular value for α allows a simplification of Equation 4.1 in the way that the forecast time of failure is at the intersection of the time axis and the best–fit linear model explaining the inverse–rate of the precursor (Equation 4.2):

$$\left(\frac{d\Omega}{dt}\right)^{-1} = \left(\frac{d\Omega}{dt}\right)_0^{-1} - A(t - t_0) \tag{4.2}$$

where t is time and $(d\Omega/dt)_0$ is the value of $(d\Omega/dt)$ when $t = t_0$.
Following Tarraga et al. (2006), the algorithm looks for linear descending inverse–RSAM trends and computes both a forecast failure time and a forecast failure window when the data are well explained by the FFM and fulfill specific criteria. The selection process is described in Figure 4.3. A moving time window of duration *dh* (with no overlap) is applied to the inverse–RSAM timeseries: in each time window, the time of the maximum inverse–RSAM is identified (*t_start_possible*). A least–squares linear regression of the inverse–RSAM timeseries is undertaken for data in the period from *t_start_possible* to *t_start_possible + min_dur*; where *min_dur* is the minimum duration for precursory activity in hours. If the linear fit (correlation coefficient *R*) is greater than a threshold *min_fit* and the relationship is significant (*p–level* < 0.05), the test period is increased stepwise by *dh2* (increase timestep duration, in hours). This last step is repeated iteratively until the linear fit is smaller than the threshold value or the relationship becomes less significant (*p–level* ≥ 0.05). The end of the tremor episode is defined in this way. Two additional conditions can be applied: a minimum relative amplitude for the RSAM increase (*min_a*) and a minimum duration between the time of the forecast issue and the forecast failure (*min_dt*). The latter can be useful for emergency management purposes. Once a potential precursory tremor episode is identified, an eruption is flagged. Its forecast time is the intersection of the best-fit linear model with the time axis. A failure window is then computed from the 97.5% prediction intervals extrapolated to the time axis. These intervals account for the standard deviation of the error in predicting future observations. In our case, there is a probability of 0.975 that failure occurs during the failure window. This automatic selection method is

applied to the entire seismic dataset (1 August 2011–1 January 2014) and prevents as much as possible subjectivity in the choice of the RSAM increase episodes and in the forecasting process.

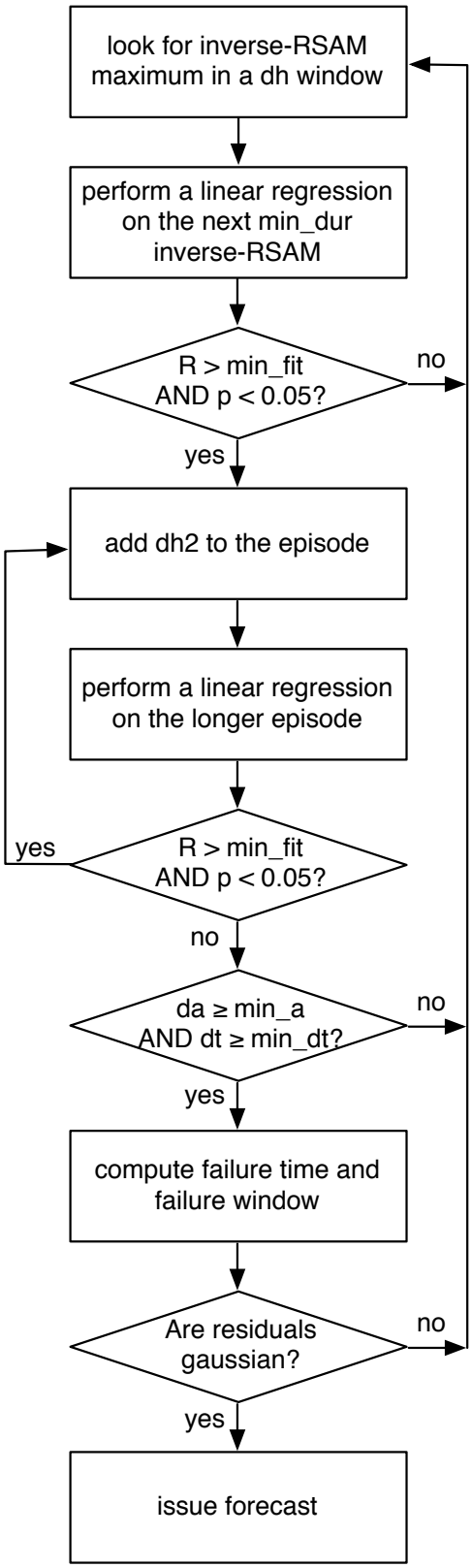

Figure 4.3: Flowchart representing the forecast issue process. See Table 4.1 for the definition of the threshold parameters (*dh, min_dur, min_fit, dh2, min_a, min_dt*). R is the correlation coefficient, p is the significance of the linear relationship, da and dt are the amplitude of the selected tremor episode and the duration between the forecast issue and a potential eruption, respectively.

Whether RSAM increases are flagged as potentially leading to an eruption depends on the input model parameters (*dh, min_dur, min_fit, dh2, min_a, min_dt*). We optimised the model through calibration with the 1 August 2011–1 January 2014 RSAM dataset. The range of tested input parameters is presented in Table 4.1. The algorithm was run for each combination of parameters on the entire RSAM dataset recorded during the period of interest. For each run, we counted the number of episodes detected and the number of well forecast eruptions. We also tested the effect of the definition of a well forecast eruption: the eruption is within 1 day of the forecast failure time (as in Tarraga et al. (2006)) (Case 1), and the eruption is within the failure window (Case 2). For each of these two cases, we compared the results from the detection algorithm when success is defined by two criteria.

Criterion 1 aims at minimising the number of false alarms by using the input parameters that maximise the forecast gain defined in Tarraga et al. (2006). Based on the Bayes theorem, the latter evaluates whether we benefit from issuing a forecast. If Hypothesis H is defined as a "day with at least an eruption" and Evidence E is defined as a "day with at least an issued forecast", the forecast gain is defined by P(E/H)/P(E) where P(E/H) is the conditional probability of having a forecast knowing that there was an eruption and P(E) is the probability of having at least one forecast issued. We benefit from issuing a forecast if the forecast gain is greater than 1, and the higher the forecast gain, the greater the benefit. More details on the forecast gain can be found in Tarraga et al. (2006). For this criterion, the best combination of input parameters was the one which gave the maximum forecast gain.

Criterion 2 aims at detecting the maximum number of forecast eruptions while keeping a forecast gain as great as possible. This criterion likely implies that more false alarms will be generated but that more eruptions will be forecast. If the forecast gain is greater than 1 (i.e., we still benefit from issuing a forecast), this criterion is a good compromise to minimise the number of false alarms and missed eruptions. For this criterion, the best combination of input parameters was the one which, among the combinations forecasting the maximum number of eruptions, gave the maximum forecast gain.

Several methods can be employed to fit the data (Cornelius and Voight, 1995; Tarraga et al., 2008). The choice of the method though, depends on the error distribution of the dataset (Bell et al., 2011). If the dataset error has a Gaussian distribution, a least–squares linear regression may be used. Conversely, if the dataset error distribution follows a Poisson distribution (e.g., earthquake occurrence (Greenhough and Main, 2008)), the alternative Generalised Linear Models should be used (Bell et al., 2011). For this study, we used a least–squares linear regression for our automated procedure and tested the assumptions of using such a method before issuing

a forecast.

Parameter	Definition	Tested value						
dh	duration of moving time window for maxima identification (hours)	2	4	6	12	18	24	36
min_dur	minimum duration of a tremor episode (hours)	6	12	18	24	48	72	96
min_fit	correlation coefficient threshold	0.5	0.6	0.7	0.75	0.8	0.85	0.9
dh2	increase timestep duration (hours)	1	2	4	6	12	18	24
min_a	minimum RSAM difference between the end and the beginning of a tremor increase (nm/s)	0	250	500	750	1000	1500	2000
min_dt	minimum duration between the time of the forecast issue and an eruption (hours)	0	3	6	9	12	18	24

Table 4.1: Range of tested input parameters for the automatic selection of the RSAM increases.

We performed a visual residual analysis on the episodes selected by the best input parameter combination. Residuals, defined as the difference between the observed inverse–RSAM and the best–fit model ($y_{observed}$ - y_{model}) were computed through time and as a function of the fitted value for each tremor increase episode to verify the linearity, independence and equal variance assumptions when using a least–squares linear regression. A histogram was then produced with the Rice rule defining the number of bins (number of bins = $2n^{1/3}$ where n is the number of samples) to verify the normality of the residual distribution. The model was considered to be appropriate to explain the data if: 1. the residuals did not follow a trend (otherwise, a more complex model should be fitted to the data), 2. the residuals did not increase or decrease as a function of the inverse-RSAM (hence had equal variance) and 3. the residuals distribution (on the histogram) was close to normal (i.e., bell–shaped, symmetric around its mean).

Because the FFM characterises the evolution of precursors to failure, it is useful to reconcile the results obtained from the FFM with a plausible tremor source process. To interpret the source of the seismic signal, spectral analyses are commonly performed (Konstantinou and Schlindwein, 2002; Carniel, 2014). Having only one seismic station for our period of interest, we can not discriminate between source, path and site effects. We are therefore unable to pinpoint a source process from our results only. However, we can compare the spectral characteristics through

time and assess how they relate to volcanic activity. For example, we analysed whether the tremor increase is due to an intensification of one or more specific frequencies, whether there is appearance / disappearance of some frequency bands and whether there are frequency shifts. To perform such an analysis, we split each of our RSAM episodes in 90-min time windows and analysed the spectra of the first 20s of each window. We normalised each spectrum to its maximum value, independently of each time window. We therefore lose the information regarding the amplitude time variations but highlight the time evolution of the relative importance of each frequency bands (Carniel, 2014).

Finally, we conducted a tremor scaling analysis (Benoit et al., 2003) to shed light on the number and potential nature of the processes involved. Aki and Koyanagi (1981) proposed that the duration–amplitude of deep tremor at Kilauea follows an exponential model implying a unique length scale for the tremor generating process which could be the average size of the conduit. This observation was later extended to other volcanoes and tremor types (Benoit et al., 2003). The last study also highlighted the possible change in slope of the duration-amplitude distribution or a change to a power law distribution if brittle fracture occurs, and the observation of several slopes in the distribution when several tremor generating processes are present. To further constrain the source of the tremor episodes preceding the White Island eruptions, we calculated the duration–amplitude distribution of each selected 2–5 Hz RSAM episode (i.e., the duration for which the tremor was above a certain amplitude). We then assessed whether the tremor source was scale-bound (exponential model) or scale invariant (power law) and whether several processes were occurring (if different slopes are present in the distributions).

4.4 Results

The optimum combination of input parameters for the RSAM detection algorithm is presented in Table 4.2 along with other combinations and their respective forecast gain. We determined the optimum input parameters by comparing the performance of the detection algorithm for different combinations of criteria (defining success: maximum forecast gain (Criterion 1) or maximum number of eruptions (Criterion 2)) and cases (defining a successful forecast: within a day of the forecast (Case 1) or within the forecast time window (Case 2)).

Criterion	Case	Forecast eruptions	Forecast gain	dh	min_dur	min_fit	dh2	min_a	min_dt
1	1	2	176.8	34 different combinations					
	2	2	88.4	89 different combinations					
2	1	5	22.1	2	18	0.5	12	1000	9
									12
		4	27.2	2	18	0.5	24	1500	0
	2	5	8.0	2	6	0.5	24	1500	0
									3
		4	**37.2**	**24**	**48**	**0.5**	**18**	**2000**	18
									24

Table 4.2: Results from the selection of RSAM increase. Please see text for details on cases, criteria and forecast gain. The preferred parameter combination (bold) maximises the number of eruption forecast within the failure window while keeping a forecast gain as great as possible.

When Criterion 1 is considered (maximum forecast gain), the best input parameters combination is obtained for Case 1 (eruption within a day of a forecast). Criterion 1–Case 1 has indeed a much higher forecast gain than Criterion 1–Case 2 (eruption within the failure window). However, only two out of the five reported eruptions are forecast.

Criterion 2 allows the setting of the number of detected eruptions while aiming for a forecast gain as great as possible. When the criterion is set to five eruptions, the maximum forecast gain is again for Case 1 (eruption within a day of the forecast). Two combinations of input parameters share this forecast gain and select the same RSAM dataset. However, for these particular combinations, an analysis of the residuals between the best–fit model and the inverse–RSAM indicates that the model is not appropriate to explain the RSAM increase preceding the 19 August 2013. Figure 4.4a shows a trend in the residuals with time, strongly suggesting a more complex model to explain this RSAM increase. The same conclusion can be drawn when Case 2 (eruption within a failure window) is considered (Figure 4.4b).

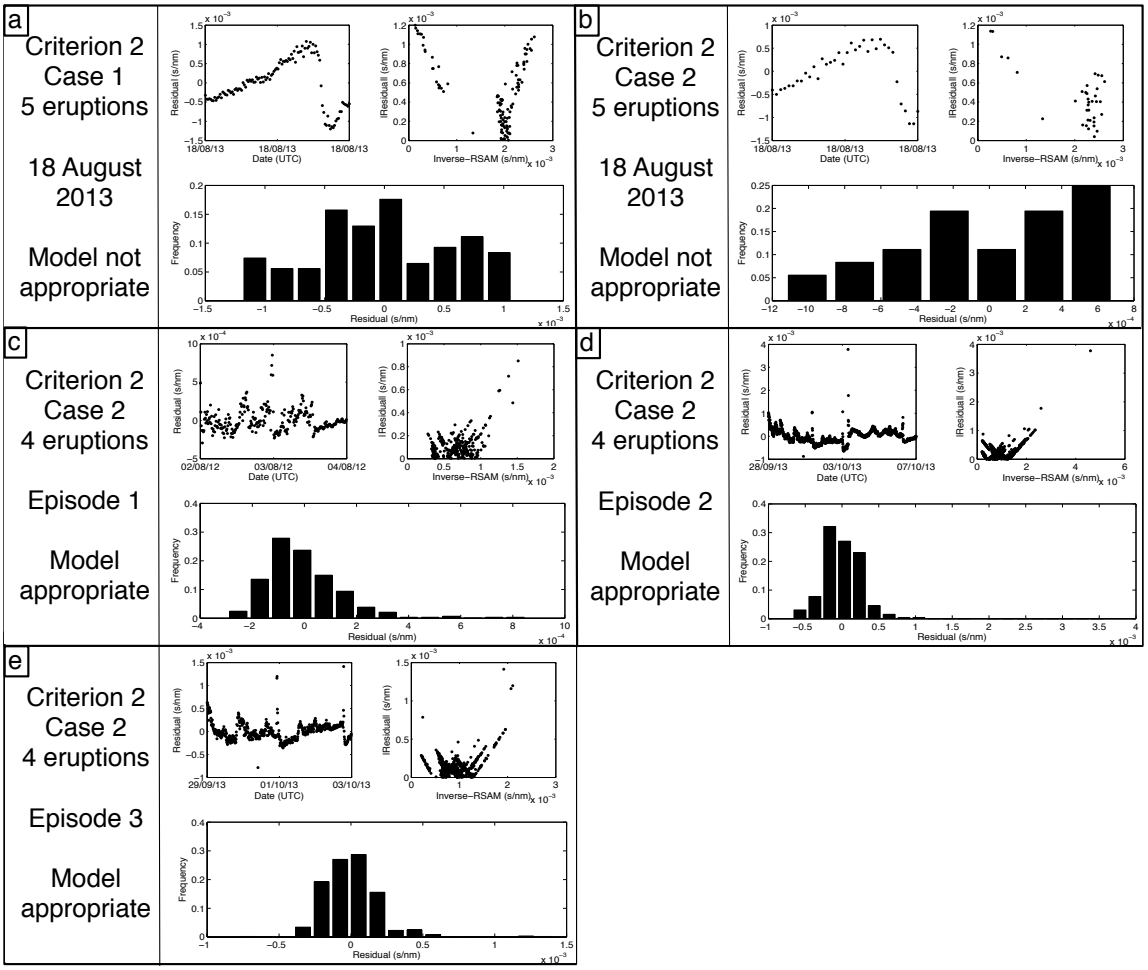

Figure 4.4: Results from the residual analysis performed on 4 tremor episodes: (a) On the tremor increase preceding the 19 August 2013 eruption selected by the algorithm for Criterion 2–Case 1 and when imposing 5 forecast eruptions (the 2 combinations of parameters (Table 4.2) select the same dataset); (b) On the tremor increase preceding the 19 August 2013 eruption selected by the algorithm for Criterion 2–Case 2 and imposing 5 forecast eruptions (the 2 combinations of parameters (Table 4.2) select the same dataset); (c) On Episode 1 selected from the optimised algorithm (Criterion 2–Case 2); (d) On Episode 2 selected from the optimised algorithm (Criterion 2–Case 2); (e) On Episode 3 selected from the optimised algorithm (Criterion 2–Case 2). For each tremor episode are plotted 2 scatter plots of the residuals (difference between best–fit model and data) versus time (top left), and versus inverse–RSAM (top right), and a histogram of the residuals (bottom). For (a) and (b), a trend in the scatter plots and a non–gaussian distribution of the residuals suggests the model is not appropriate to explain the data. In contrast, the model is appropriate to explain Episode 1, 2 and 3 (c, d, e). Note the different scales for the figure axes.

Due to the results on the residuals, we evaluated the value of issuing a forecast when imposing the detection of the four other eruptions only. In that situation, Case 2 gives a higher forecast gain than Case 1. Two combinations of input parameters give the same forecast gain for this particular Criterion / Case. Because the only difference between the two combinations is the duration between the forecast issue and forecast failure time (parameter *min_dt*; 18 or 24 hours, Table 4.2), we chose the one maximising this duration (24 hours). This arbitrary choice is for emergency management purposes as it provides the maximum warning time.

The residual analysis of Criterion 2–Case 2 and four forecast eruptions shows that the model is appropriate to explain the tremor increases preceding these eruptions (Figure 4.4c, d and e): no trend is observed in the scatter plots and the residuals distribution is close to Gaussian. To support the appropriateness of the Gaussian distribution, we performed a linear regression on the selected inverse–RSAM episodes assuming either a Poisson or a Gaussian distribution. The deviance from a linear model is smaller when assuming a Gaussian distribution. Although this is not a formal test, this leads us to prefer the Gaussian distribution and confirms that a least–squares linear regression is appropriate.

These results suggest that the combination of input parameters from Criterion 2–Case 2 and four forecast eruptions may be optimum (Table 4.2). The detected RSAM increases are therefore of 48–hour duration and 2000 nm/s amplitude at least, and the forecast is issued at least 24 hours prior to the forecast time. Practically, the beginning of an episode is sought in every 24–hour window, the correlation coefficient R between the best–fit model and the inverse–RSAM is at least 0.5 and the episode is increased stepwise by 18–hour windows until the fit becomes lower than 0.5.

The RSAM episodes detected with this optimised detection algorithm are shown in Figure 4.5 and their characteristics are summarised in Table 4.3. Three RSAM episodes are selected and four out of the five eruptions reported during the studied period are within the three forecast failure windows (i.e., our optimised algorithm produces no false alarms, defined as a failure window with no eruption, which is potentially linked to the limited statistics). For each episode, the model is appropriate to explain the data and the correlation coefficient R is higher than 0.7 (Table 4.4), implying a coefficient of determination R^2 higher than 0.5 (i.e., at least 50% of the variation in the dataset can be explained by the model). We are therefore satisfied that the material failure law with $\alpha = 2$ in Equation 4.1 is a reasonable approximation for the tremor increases preceding the 4 August 2012, and the 4, 8 and 11 October 2013 eruptions at White Island and that these tremor episodes can be considered as precursors to failure.

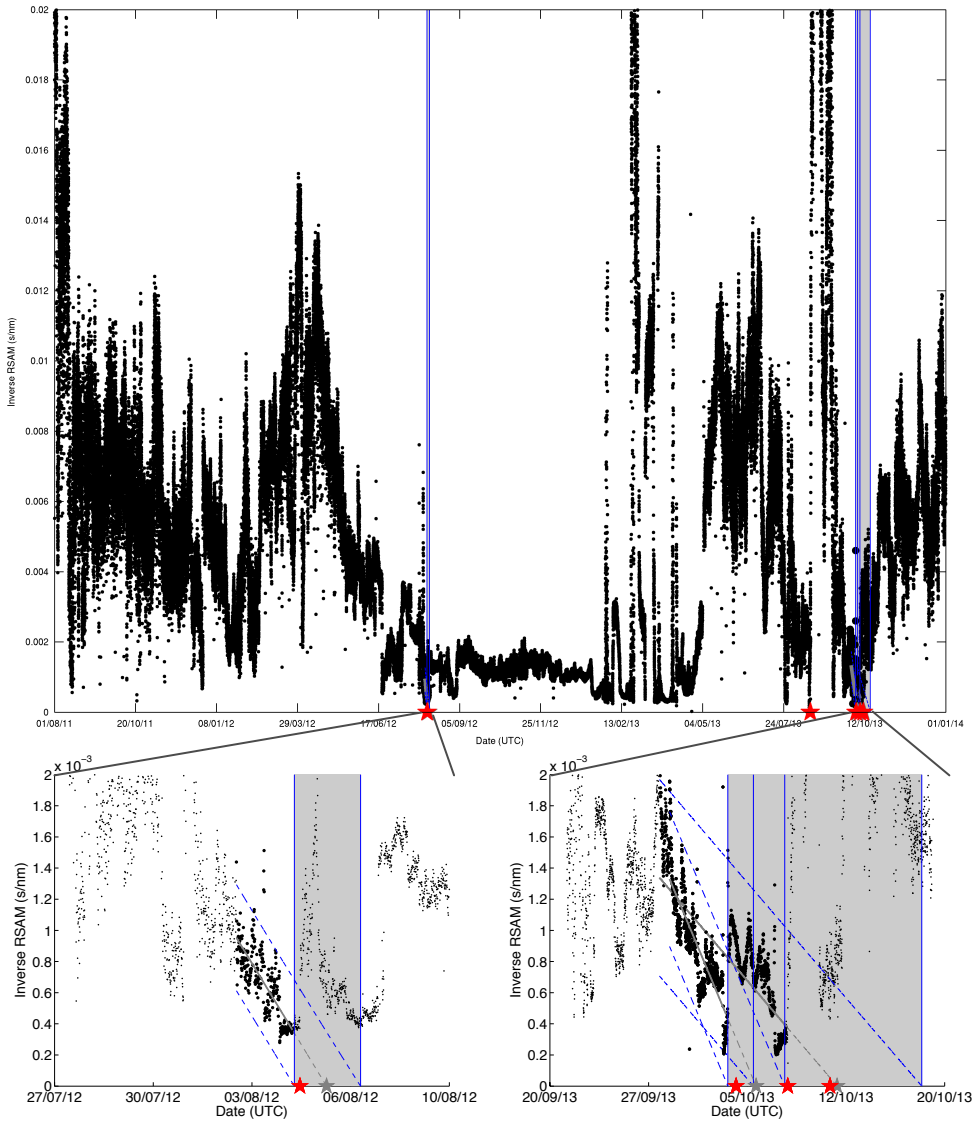

Figure 4.5: Inverse-RSAM data recorded at WIZ between 1 August 2011 and 1 January 2014 with the failure windows forecast by our automated and optimised FFM algorithm (grey patches) and the eruptions reported during this period (red stars). Below are close-ups around these failure windows computed from the 97.5% prediction interval (dotted blue line) with the data chosen for fitting the FFM (grey line) and the forecast failure time (grey star) obtained from the extrapolation of the best–fit model (dotted grey line). Note the successive shorter-scale linear trends composing the main trend.

Ep. #	Start episode	End episode	Start failure window	End failure window	Forecast failure
1	02/08/2012 10:50	04/08/2012 10:30	04/08/2012 12:10	06/08/2012 20:30	05/08/2012 15:33
2	28/09/2013 07:50	07/10/2013 22:30	05/10/2013 11:10	18/10/2013 06:20	11/10/2013 19:56
3	29/09/2013 02:20	03/10/2013 09:20	03/10/2013 12:40	07/10/2013 20:30	05/10/2013 16:06

Table 4.3: Dates and times characterising the selected RSAM episodes.

Ep. #	Fit with FFM	Fit with power law model	Fit with exponential model
1	0.75	0.847	0.925
2	0.70	0.871	0.950
3	0.80	0.956	0.958

Table 4.4: Correlation coefficient R between the selected inverse–RSAM episodes and different models.

The spectral content of each detected RSAM episode is presented in Figure 4.6. First, the tremor episodes are non–harmonic with most of the seismic energy below 3.5 Hz. Second, the 3.0–3.5 Hz band is dominant during Episode 1 (preceding the 4 August 2012 eruption) whereas it is the 2.0–2.5 Hz band which contains the most energy from the start of Episode 2 to the end of the Episode 3 (episodes preceding the October 2013 eruptions). Then, the seismic energy is well partitioned between 2.0 and 3.5 Hz until the end of Episode 2 (i.e., there is no dominant frequency band). It is worth noting that the first eruption came from the dome area, whereas the other eruptions originated from the active lake area with the dome still strongly degassing.

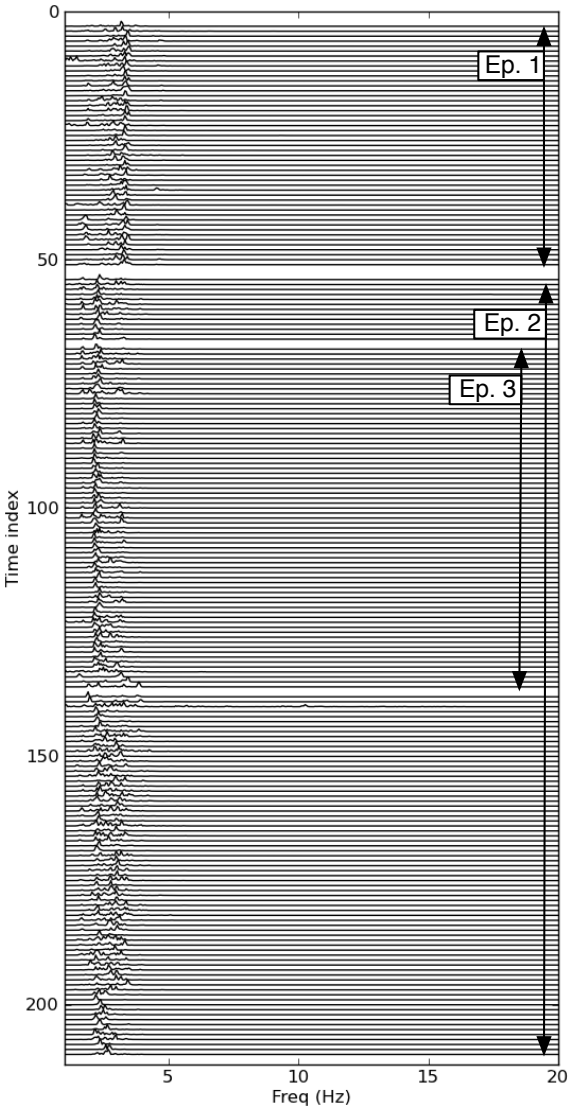

Figure 4.6: Spectra on 20-sec seismic waveforms every 90 minutes recorded at WIZ for each selected tremor increase detected versus time. Note that Episode 3 is within Episode 2. Also, the 3–3.5 Hz band is dominant during Episode 1 whereas it is the 2–2.5 Hz band the beginning of Episode 2 and Episode 3. The end of Episode 2 has seismic energy well partitioned between 2 and 3.5 Hz.

Finally, the results from the tremor scaling analysis are presented in Figure 4.7. Because the duration–amplitude distributions of the selected tremor episodes are not linear on the log–log plot (Figure 4.7a), they do not follow a power law model. Instead, these distributions better fit

an exponential model (Figure 4.7b, Table 4.4), as predicted by Benoit et al. (2003). They still present some non–linearity, with a generally steeper slope at high amplitudes. Data clipping could be one explanation for this phenomenon but we are confident that our 2–5 Hz RSAM data were not computed on clipped waveforms. We therefore attribute these departures in slope to the presence of a second tremor–generating process, following Benoit et al. (2003).

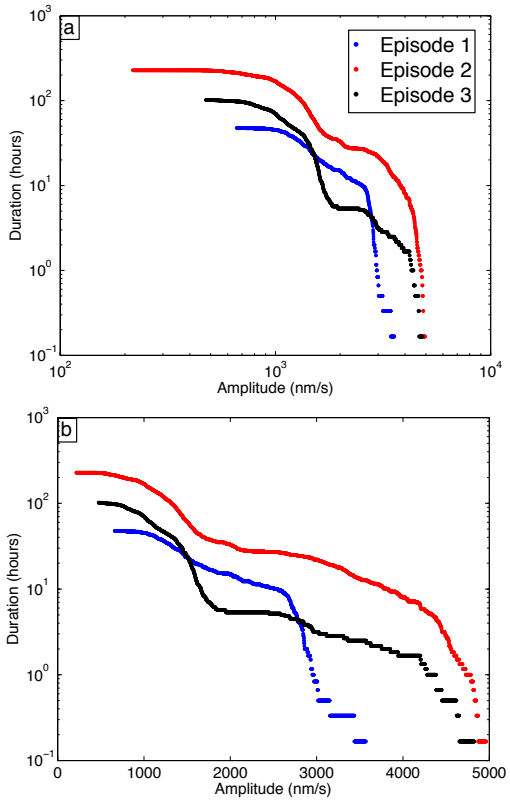

Figure 4.7: Results from the tremor scaling analysis on each selected tremor increase by plotting the duration for which the tremor is above a certain amplitude. The linearity of the duration–amplitude distribution in a log–log plot (a) and in log–linear plot (b) determines the fit with a power law and an exponential model respectively. An exponential model always fits the data better than a power law model (see Table 4.4) but the distributions are non–linear for both models implying the presence of several tremor generating processes.

4.5 Discussion

Four out of the five eruptions that occurred during the recent unrest period at White Island were forecast in hindsight using our optimised automatic implementation of the FFM on volcanic tremor recorded by 2-5 Hz RSAM data. Despite having a similar goodness–of–fit with the model

and similar duration–amplitude distributions, the tremor increases preceding the eruptions do not share the same spectral characteristics. Here we discuss the source of these tremor increases in light of our results and how these may improve eruption forecasting at White Island.

4.5.1 Insights into the tremor source

Our findings demonstrate that the FFM with $\alpha = 2$ (Equation 4.2) appropriately models the tremor increases preceding four out of the five eruptions reported during the recent unrest period at White Island volcano. This implies that these tremor increases were likely precursors to failure. Due to the lack of stations, we can not ascertain whether the distinct observed frequency peaks were due to a volcanic source effect. However, Sherburn et al. (1998) showed that seismic energy between 1 and 4 Hz at White Island mostly represents a source effect. Also, although the presence of a single frequency peak in a spectrum cannot be ascribed to source, path or site effects, a change in frequency peaks can be more easily explained as source, although there are examples where path effects can be also important. Site effects cannot usually explain frequency changes. Therefore, an increase in seismic energy in this frequency band likely reflects some changes at the source (at least its strength).

Because several shorter accelerating trends compose the detected tremor increases (Figures 4.2b and 4.5), as expected by the multiscale fracturing model (Kilburn, 2003); a similar process might have occurred at White Island prior to the four forecast eruptions. We therefore surmise that the observed short RSAM accelerating trends likely represent the growth and coalescence of small cracks during the propagation of a main fracture acting as the pathway for magma ascent. Particularly, the increase of the peak rate depicts the connection between subvertical fractures and obeys the Voight's relation (Equation 4.1) for $\alpha = 2$.

Even though fracturing is usually associated with high–frequency seismic events, we argue that the low–frequency signal (2–5 Hz) recorded prior to the eruptions can be a proxy for fracturing. The fracturing process can, for example, be depleted in high–frequency energy. Such a process can explain the low–frequency signature of seismicity during hydraulic fracturing experiments (Das and Zoback, 2013); during non–volcanic tremor episodes associated with slow–slip events (Shelly et al., 2007) or in the unconsolidated shallow part of the volcanic edifice (Bean et al., 2014). In the first two cases, the high–pressure environments can lead to slip under low shear stress, hence resulting in relatively slow slip velocity and a corresponding deficit in high–frequency energy (Shelly et al., 2007). This could also be the case at White Island where the direct involvement of hydrothermal fluids to shear failure processes is a possible source of the long–period short–duration events (Sherburn and Scott, 1993).

In the Bean et al. (2014) model, slow–rupture is due to the low angle of internal friction of a material close to the brittle–ductile transition. The seismic events are recorded as short–duration long–period pulses close to the source and as long–period events further away (from 500–800 m at their studied volcanoes) because of some resonant effects in the source–receiver path. Weak tuffs sampled from the crater floor at White Island have a low angle of internal friction and can produce continuous low amplitude acoustic emissions during laboratory scale failure around the brittle–ductile transition (Heap et al., 2015). Moreover, the seismic station used in this study is > 600 m from the source (assuming the source is located under the vent), and because the shallow portion of the edifice is strongly attenuating ($Q < 5$, Jolly et al., 2012), we are probably recording strong path effects. These characteristics also imply that even if the fracturing process produces high–frequency energy, these high-frequencies may not reach the station because of a path or site attenuation effect. A particle motion analysis and a detailed study of source / path / site effect is required to discriminate between the different hypotheses. However, if tremor is a repetition of these low–frequency events or if the source mechanism is similar for both tremor and low–frequency events resulting from the models above, tremor directly relates to failure. Studying low–frequency tremor can therefore inform on the fracturing process. According to the multiscale fracturing process (Kilburn, 2003); the detected tremor increases preceding the eruptions at White Island can therefore mainly reflect the propagation of a main fracture acting as a pathway for the erupted material.

The 19 August 2013 eruption is not forecast by our optimised algorithm. It was dominated by steam (Figure 4.2e) whereas the other eruptions seemed more ash–dominated (at least the 4 August 2012 and the 11 October 2013 ejected ash and blocks onto the crater floor). It might be that the 19 August event was produced by a gas slug rather than by magma. If the former, the lower viscosity of the gas slug might have passed without much resistance (or stress concentration) on the system. Conversely, the 4 August 2012 eruption had substantial magmatic component and so did the October events (Geoff Kilgour, pers. comm., 2013). In order to reach the surface, the volcanic material associated with these eruptions likely pressurised the system before reaching the surface. This could explain why the precursory volcanic tremor is reasonably well–modelled by the FFM for these eruptions and not for the 19 August 2013 one. There is however, one particular behaviour of precursory activity predicted by the FFM that our results can't explain. The failure model implies that the seismic energy release increases until the eruption. This is not observed before the four forecast eruptions reported in this study. One reason for this might be the layer cake stratigraphy of White Island rocks. Pressurised fluids propagate through a particular layer via brittle–ductile failure over a few days.

When they reach another rock type (e.g., a clay layer of different strength), they accumulate and pressure increases until failure. A quieter period before eruptions has also been observed at other volcanoes (e.g., Redoubt 1989-90 (Chouet et al., 1994); Villarrica (Ortiz et al., 2003)). In the case of a resonant model, Chouet et al. (1994) proposed that a fluid flow reduction occurred in the resonator. This could happen, for example, because of the opening of new pathways, and could explain the decrease in the intensity of low–frequency seismicity.

This last point leads us to consider other models for the tremor source (Table 4.5). Many of these models or combination of these models may be consistent with our data and they are important to outline. However, the lack of multiple seismic stations makes distinction between these different models very difficult and beyond the scope of this study. The low–frequency content of the signal points towards fluid involvement (Chouet, 1996). However, to the best of our knowledge, no published literature demonstrates how tremor resulting from the models involving fluids can follow the material failure law. Peaked spectra may be created by a range of processes including the fluid flow oscillations model (Julian, 1994); the container resonance model (Chouet, 1996; Neuberg et al., 2000), the magma wagging model (Jellinek and Bercovici, 2011) and hydrothermal boiling in a channel (Leet, 1988). Gliding frequencies have been observed prior to eruptions (e.g., Neuberg et al., 2000) and are explained as changes in the triggering frequency of the source rather than changes in the source itself. Non–harmonic spectra can also be recorded in these cases by the seismic station as a result of site or path effect (Chouet, 1996; Neuberg et al., 2000). Whether the two main spectral bands (2.0–2.5Hz and 3.0–3.5 Hz) result from two different fluids (Kumagai and Chouet, 2000) or geometries (Kumagai and Chouet, 2001) at the same source or from two distinct sources (e.g., Arenal, Lesage et al., 2006) can not be constrained by the results of this study. It is interesting to note though that the dome area was the most active vent in August 2012 when the 3.0–3.5 Hz was the dominant spectral band whereas the 2.0–2.5 Hz band was more important in October 2013 when the eruptions came from the hot lake area. This observation suggests a potential link between the active vent location and the dominant frequency peak but is not sufficient to determine the tremor source. If tremor preceding the eruptions resulted from a fluid flow model, we can reconcile the tremor source with the FFM results when considering that tremor represents pressurisation under a plug that fails when fluid pressure exceeded its yield strength. This model was proposed to explain the tremor increases preceding the July 2000 eruptions at Villarrica (Ortiz et al., 2003).

Tremor models		Spectral content	Link to failure	Reference
Fluid flow oscillations	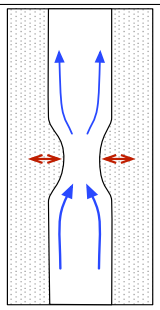	Harmonic spectrum Subharmonics if pressure increase	If pressure $\geq$ $P_{threshold}$	Julian (1994)
Resonance	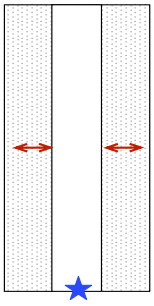	Peaked spectrum Different frequencies if different modes of resonance Gliding frequencies if source change	If pressure $\geq$ $P_{threshold}$	Chouet (1996) Neuberg et al. (2000)
Magma wagging	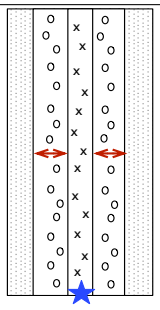	Peaked spectrum Gliding frequencies if pressure increase	If pressure $\geq$ $P_{threshold}$ (fragmentation)	Jellinek and Bercovici (2011)
Hydrothermal boiling	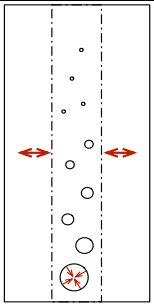	Broadband spectrum or harmonic if in a channel	No	Leet (1988)

Table 4.5: Features of the main characteristics of the tremor generating processes involving fluids discussed in this study to explain the observed tremor increases. For each model diagram are shown: the trigger (blue) and the mechanism (red) of the tremor generating process. The trigger can be a pressure disturbance (star) or a fluid flow (arrow) whereas the mechanism involves some oscillations (double–arrow). The diagram patterns are: fluid (white) with magma (crosses), surrounding medium (dotted), bubbles (empty circles).

Finally, our current procedure assumes a constant model with time (i.e., α in Equation 4.1 is always 2) which has been debated by Kilburn (2003) and Kilburn (2012). The difficulty in

discriminating exponential and power laws when fitting datasets, because much of the difference between the two models appears close to the ends of the sequence, has also recently been emphasised by Bell et al. (2011). In addition, the same authors highlight the presence of complex interactions that inherently occur in volcanic systems and which can lead to strong deviations from the mean rate. Our residual analysis indicates that a general linear trend is a good approximation to explain the inverse–RSAM preceding four out of the five reported eruptions of our period of interest. This supports the hypothesis of using a constant $\alpha = 2$. However, this parameter might be slightly different or slightly time–varying, which would result in a different forecast failure time. Also, the different slopes that we observe in the duration–amplitude distributions of volcanic tremor preceding the four forecast eruptions point towards the presence of several tremor generating processes. These effects could potentially explain the difference between the forecast failure time and the actual eruption. However, overall, our results using $\alpha = 2$ and corresponding prediction intervals give satisfactory results.

4.5.2 Implications for eruption forecasting

Even though this forecast exercise was performed in hindsight, our results demonstrate that our capability in eruption forecasting could be enhanced by using the material Failure Forecast Method on volcanic tremor (2–5 Hz RSAM) at White Island. First, we showed that RSAM increases with particular characteristics can be considered as precursors for eruptions at White Island, for the 1 August 2011–1 January 2014 period which comprises the recent unrest period. These episodes usually started from an elevated tremor level, lasted for only a few days and ended from a few hours to a few days before the eruptions. Second, issuing a forecast using our method is reasonable from a probabilistic point of view. The prior probability to have an eruption on any day during the unrest episode was 0.0057 (number of eruptions (5) / number of days within the episode (884)). The posterior probability of having an eruption given that we issued a forecast is obtained by multiplying the forecast gain calculated above by this prior probability (Tarraga et al., 2006). Using the optimum combination of input parameters for the RSAM detection algorithm (Table 4.2), this posterior probability is 0.21 meaning that we have slightly more than 1 in 5 chances to have an eruption on a given day if it is within a forecast failure window. This result is based on RSAM evolution only and could feed probabilistic models for eruption (Hincks et al., 2014; Aspinall and Woo, 2014) which also integrate other datasets. Finally, recent studies highlight a growing interest for real-time eruption forecasting using the FFM (Garcia et al. 2008, Boue et al. 2015). Our work is a contribution towards this international effort. Apart from the residual analysis, our procedure is entirely automatic

and can easily be implemented in real–time at White Island using our optimised parameter combination as a starting point. Our optimised algorithm provides the best forecasts according to our criteria (maximum number of forecast eruptions with one algorithm). At this stage, our algorithm is limited to issue a forecast after 48 hours of precursory activity, with an update every 18 hours if the activity continues. Parameters should be adjusted should more frequent forecasts be wanted. If needed, the model can be easily optimised with more constraints on the input parameters. Also, several algorithms could be run in parallel, which could allow to forecast eruptions with precursory activity having different characteristics. In a broader context and because 2–5 Hz data from only one seismic station were used for this study, the algorithm could easily be tested at other volcanoes where a limited network (even of short-period instruments) is available and where tremor (or any other seismic signal responsible for the observed RSAM evolution) is a good candidate for eruption precursors (i.e., if some RSAM increases have been observed prior to some eruptions).

4.6 Conclusions

We tested an automated and optimised implementation of the FFM on volcanic tremor from the recent eruptive period at White Island to assess the potential for eruption forecasting at the volcano and to constrain the tremor source.

We have shown that, in hindsight, the optimised algorithm forecasts four out of the five eruptions reported during this period (i.e., the eruptions occurred within the predicted failure windows). Equally important is the high forecast gain which implies that the probability to have an eruption within a failure window is 0.21 based on RSAM only, 37 times higher than the probability to have an eruption on any day during the same period (0.0057). Performing a detailed residual analysis rather than using the correlation coefficient alone allowed to fine–tune the results.

A reasonable goodness–of–fit between the FFM and the data implies that the tremor increases preceding the eruptions can be considered as precursors for failure. Also, $\alpha = 2$ is a suitable approximation in our case to explain the tremor episodes evolution for four out of the five eruptions reported during this unrest period. The spectra of these episodes is non–harmonic and each episode bears particular spectral characteristics with different dominant frequency bands. Because we used seismic data from one seismic station only, we can't pinpoint a source process for the tremor increases preceding these eruptions. However, the low–frequency content of the signal suggests that multiscale fracturing involving slow rock failure or fluid flow processes are plausible candidates for the tremor source model. The duration–amplitude distributions support our preferred model with several source processes occurring during these episodes. As

such, we don not claim that we capture the complexity of the processes that occurred prior to the eruptions but we argue that the use of the FFM while accounting for uncertainties can enhance forecasting capabilities even at a volcano where only a limited monitoring network is available.

Chapter 5

Conclusions

Abstract

In this chapter, I will first summarise and discuss the findings of this thesis and provide answers to the objectives and research questions raised in the introduction chapter. I will then present the implications and limitations of this research. Finally, I will propose some recommendations for future research in the topic area of this thesis.

5.1 Findings of this research

Geophysical signals are expected to change during increased volcanic unrest and preceding eruptions. If detected, understanding the source of these changes is one of the key challenges in current volcano research (Acocella, 2014). In this study, I demonstrated that a comprehensive analysis of magnetic, gravity and seismic data can enhance our understanding of increased unrest and eruption precursors.

I first analysed magnetic and gravity changes measured between 2011 and 2015, a period which comprises the recent unrest/eruptive episode at White Island. I modelled the potential source(s) for the observed changes and proposed a scenario to demonstrate that these techniques can be useful to interpret increased unrest at White Island (Chapter 2). I then performed numerical simulations to assess the effect of an inclined conduit on hydrothermal circulation and gravity changes at the surface, to highlight the effect of structural geology on the interpretation of geophysical signals (Chapter 3). Finally, I implemented an algorithm to automatically issue eruption forecasts from increasing level of volcanic tremor at White Island (Chapter 4).

I showed that at White Island, magnetic changes occurred from the beginning of the 2011-2013 unrest, and are attributed to temperature changes at shallow depths in the active crater area (Chapter 2). These changes were associated with varying levels of tremor and the disappear-

ance of the crater lake. By constraining the magnetic results using the lack of significant gravity changes during the same period, I showed that the heat needed for the magnetic changes can stem from the emplacement and degassing of a shallow magmatic intrusion, if the intrusion is comprised within a narrow conduit at $\sim$ 500 m depth (Chapter 2). I proposed that the following cooling period likely reflects the inflow of colder fluids from the existing hydrothermal system, as the excess gas reaches the surface and depressurises the system. A combination of gravity and magnetics at White Island can therefore bring valuable information into the state of the volcano and help characterise increased unrest.

The measured gravity data are very noisy for unknown reasons at the time of writing, especially at the site between the main fumarole outlet and the crater lake, which is also the locus of strong deformation. Previous studies suggested an inclined fumarole conduit to explain the recent deformation. I therefore tested the effect of such an inclined conduit on hydrothermal circulation and gravity changes and showed that a conduit of small diameter with rock properties consistent with laboratory measurements on White Island samples would mainly shift the gravity anomaly towards the injection area (Chapter 3). In the case of an inclined fumarole, this implies that the gravity anomaly is not centred around the fumarole outlet. The gravity anomaly is of maximum amplitude at the edge of the two-phase hydrothermal plume, which is very sensitive to the injection rate at the source. Microgravity measurements could therefore inform on the location of the injection source and of the two-phase hydrothermal plume if performed at regular intervals. The numerical simulations involved modelling of steady state conditions and of a one-year long unrest episode. Because of the high permeability of the domain, the fluids quickly propagate towards the surface. In such settings, yearly (or more regular) microgravity campaigns are therefore recommended. The measured gravity data mentioned above (Chapter 2) don't show a circular anomaly but this could be due to the high level of noise in the data, to the inappropriate location of the gravity sites or to a more complex geometry of the fumarole conduit (e.g., involving branching of several conduits).

No magnetic and gravity changes occurred after the eruptive activity started in August 2012. However, strong variations of volcanic tremor were associated with various types of volcanic activity during this period, such as eruption and geysering (Chapter 4). Increasing levels of tremor with particular characteristics can be used for reliable eruption forecasting at White Island. Four out of the five eruptions which occurred in 2012–2013 were within failure windows forecast by our procedure. A robust residual analysis indicates that the tremor increases preceding these eruptions are well explained by a model whereby an eruption is a case of material failure caused by loading of a magma column. Moreover, the probability to have an eruption

within an eruption window is 0.21, 37 times higher than the probability to have an eruption on any day during the same period (1 August 2011–1 January 2014).

This thesis leads to a better understanding of unrest signals and eruption precursors at White Island. First, I showed that regular magnetic and gravity measurements can help characterise the unrest source. Second, I demonstrated that volcanic tremor with particular characteristics were precursory to the eruptions in 2012 and 2013. These results are only based on one specific unrest/eruptive period but they provide clues to changes to monitor during a future renewal of volcanic activity at the volcano.

5.2 Answers to research questions

The findings of this research allow to answer the research questions raised in Chapter 1 and demonstrate that I reached the objectives set for this study (Table 5.1).

Objective	Question	Answers provided	Chapter
Characterise the sources of the gravity and magnetic changes at White Island	What are the sources of the magnetic changes associated with the 2011-2013 unrest/eruptive episode?	The magnetic changes preceding the 2012 eruption are consistent with a model whereby temperature changes occurred at shallow depths below the active crater	2
	What is the evolution of gravity changes observed prior to the eruptions?	No significant gravity changes were recorded within the crater floor but there is a high level of noise in the data	2
	Can the observed geophysical changes inform on the state of the volcano?	Yes, the observed changes are consistent with an unrest scenario involving deep degassing and a possible small magmatic intrusion	2

Describe the effect of an inclined fumarole on hydrothermal circulation and gravity changes	How does the fumarole inclination affect hydrothermal circulation?	The fumarole inclination shifts the two-phase hydrothermal plume above the injection area	3
	What are the effects of an inclined fumarole on gravity changes at the surface?	The fumarole inclination shifts the gravity anomaly around the injection area, i.e., the gravity anomaly is centred around the fumarole outlet only when the fumarole is vertical	3
Assess the potential of using volcanic tremor for eruption forecasting at White Island	Can the evolution of volcanic tremor be precursory for eruptions?	Yes, tremor increases preceding four out of the five eruptions which occurred between 2011 and 2013 are well explained by a model whereby an eruption is a material failure due to magma loading	4
	How can volcanic tremor increases be used for eruption forecasting?	By implementing an automated process of eruption forecasts using the material Failure Forecast method and a robust residual analysis	4
	Can the source of volcanic tremor be reconciled with current models?	Yes, I propose that multi-scale fracturing involving fluid flow processes and/or slow failure is a likely process for the tremor increases preceding the eruptions	4

Table 5.1: Objectives and research questions raised in the introduction and answers provided by this thesis.

5.3 Implications and limitations of the research

The results from this research are only based on the most recent unrest/eruptive episode (2011-2013) at White Island but they give insights into what parameters to monitor should there be a renewal of activity at this volcano. The type of signals analysed are commonly recorded at volcanoes worldwide (magnetics: e.g., Bonaccorso et al., 2013; Johnston, 1997; Zlotnicki and Bof, 1998; gravity: e.g., Berrino, 1994; Gottsmann et al., 2005; Williams-Jones et al., 2008; volcanic tremor: e.g., McNutt, 1992) so a similar approach than the one undertaken in this study could be developed at other volcanoes.

I demonstrated that regular magnetics and gravity measurements are useful techniques to characterise increased unrest at White Island (Chapter 2). The magnetic anomaly is on the edge of the network and is therefore not very well constrained but enough sites recorded the anomaly to run some inversions and get a location and size for the source of the observed changes. Limited constraints on the hydrothermal effect on gravity changes (groundwater level and phase change within the system) lead to uncertainties in the volume of a possible intrusion. Another limitation of our dataset is the high level of noise in the gravity data. Despite these constraints, a combination of the two techniques (magnetics and microgravity) allowed a better understanding of the possible heating source during the recent unrest period at White Island. In such settings where the crater lake (direct representation of the changes within the conduit system) is difficult to instrument, getting insights from changes within this conduit system from other techniques performed on the crater floor is therefore very relevant.

The numerical model of hydrothermal circulation presented in this thesis (Chapter 3) is constrained using parameters consistent for the settings of fumarole zero at White Island. It therefore considers a specific scenario of unrest and a small fumarole conduit one order of magnitude more permeable than the surrounding medium. I highlighted the importance of monitoring gravity changes in a wide area around the fumarole outlet to capture the evolution of the two-phase hydrothermal plume and to constrain the location of the injection source. The same conclusions could by drawn for other volcanoes with similar settings. Ultimately, a better understanding of the conditions at the source of the fumarole could inform on the state of the volcano, which is useful in settings where the active crater (and possible crater lake) are challenging to instrument.

Volcanic tremor can be used for eruption forecasting using the material Failure Forecast Method at White Island (Chapter 4). Our process is however not entirely automatic (e.g., residual analysis) implying that a scientist still needs to make the final decision as to whether issue a forecast or not (according to the visual assessment of the gaussian residuals). The algorithm is also cur-

rently calibrated on four eruptions out of the five eruptions that occurred between 2011 and 2013. Even though the probability of the occurrence of an eruption within a failure window is much greater than that of an eruption on any day, the algorithm is not forecasting one eruption of the sequence (19 August 2013). This needs to be further investigated by calibrating another algorithm on this eruption for example. Despite these limitations, eruption forecasting capabilities can be enhanced in New Zealand where there is currently no eruption forecasting process. A similar approach could also be developed at other volcanoes where increasing level of seismicity is observed prior to eruptions. Our process being specific to a volcano and an eruption sequence at the time of writing, it would need to be calibrated before being used on other volcanoes and eruption sequences.

5.4 Recommendations for future research

The findings of this research suggest several aspects that would benefit from future research effort.

I demonstrated the usefulness of magnetic and gravity measurements to constrain the source of the 2011-2012 increased unrest at White Island. I therefore recommend pursuing this monitoring effort, either in campaign mode, or by installing continuously recording instruments in specific areas. The latter option would be preferred to also better constrain the timescales of the processes. For example, Gottsmann et al. (2007) observed changes of a few tens of μGal over periods of tens of minutes that they attributed to degassing instabilities at Nisyros caldera. The same amplitude of gravity changes over a period of a few months could have been wrongly interpreted as magmatic intrusion or other long term processes. Other short–term processes have been reported at Mount Etna during the 2002-2003 eruption and at Masaya volcano during short continuous experiments (Williams-Jones et al. (2008) and references therein). A similar assessment for White Island is necessary to due the presence of active geothermal features.

Studies should be performed to constrain the reason of the high level of noise in the gravity measurements. If short-term processes are responsible for this noise, then continuously recording instruments would depict them. These measurements would need to be completed by deformation measurements to assess the effect of elevation changes to the recorded gravity signal. In this thesis, I consistently used the common free-air gradient value of 0.3086 mGal m^{-1} to correct for elevation changes. Several studies showed that this value might change depending on the sites (e.g., Rymer, 1996; Williams-Jones et al., 2003). I therefore recommend an assessment of this value for each gravity site at White Island. The maximum noise level was observed at the site located between the active fumarole area and the crater lake, which is also the site showing

the strongest deformation (Fournier and Chardot, 2012). Particular effort towards constraining the effect of deformation on gravity changes at this site should therefore be undertaken. With the current monitoring strategy (i.e., campaign type measurements), this implies installing a levelling peg at this site.

In order to better constrain the source of the gravity changes, a better quantification of of hydrothermal processes is recommended. Because this effect counteracts that of an intrusion, it is important to better monitor the groundwater level and the phase changes within the system. From the numerical simulations of hydrothermal circulation due to an episode of increased degassing, I showed that the maximum gravity anomaly is observed above the edge of the shallow two-phase hydrothermal plume. The spatial extent of this plume strongly depends on the injection source (i.e., the injection rate of volcanic fluids). I therefore encourage studies aiming at constraining the location of this two-phase plume, so that information can be gained on the source of the fluids. Repeated gravity measurements (or continuous gravimeters) made above the edge of this two-phase plume would contribute to this effort.

Further investigation of the relationship between hydrothermal circulation and geophysical observables would bring some valuable insights into unrest scenarios at White Island and other volcanoes. For example, more numerical modelling of hydrothermal circulation affected by fumarole conduits with varying permeabilities, fumarole conduit diameters and fumarole inclinations would allow to generalise the results of this research which are currently representative of the fumarole zero at White Island. In the White Island context, the model could also be improved by for example comparing the steady state conditions (or unrest conditions) of the model with field data such as measurements made at the fumarole outlet (e.g., temperature, flow, CO_2/H_2O ratio). Another line of research could be to compute magnetic changes from hydrothermal circulation, in a similar approach than the one undertaken for computing gravity changes. Magnetic changes due to thermal effect mainly occur within 300 and 600 °C, which is out of the temperature range for TOUGH2/EOS2. Using another modelling code for hydrothermal circulation (e.g., Christenson et al., 2010; Afanasyev et al., 2015) would circumvent this issue.

The eruption forecasting algorithm presented in this research could help forecast future eruptions at White Island if implemented in near real-time. Some adjustments need to be made to the code beforehand e.g., automation of the residual analysis, conversion from a hindsight to a foresight approach. Also, testing the algorithm on independent datasets such as historical tremor data would help constrain the behaviour of the algorithm on future datasets. This approach is similar to that undertaken for earthquake forecasting (e.g., Gerstenberger and Rhoades, 2010).

Some modifications of this algorithm could allow better forecasts at White Island and other volcanoes. This algorithm could for example be adjusted to forecast the eruptions that were missed by the current algorithm (e.g., 19 August 2013) and run in parallel to the existing one. The method used in this research to forecast eruption is indeed not dependent on a single type of data, as long as the evolution of the dataset follows that of a precursor for eruption following the material failure law (Voight, 1988). If some eruptions are preceded by accelerating rates of some monitoring parameter(s) at White Island or other volcanoes, the same method as the one used in this research could therefore be developed. Ultimately, integrating the forecasts into a Bayesian Belief network (e.g., Aspinall and Woo, 2014; Hincks et al., 2014) would allow forecasts to be issued while accounting for different datasets.

Several models for the tremor source were discussed in Chapter 4 and some suggestions were made on the most likely model to explain the tremor increases preceding the White Island eruptions (multiscale fracturing, fluid flow processes, slow failure). These hypotheses would need to be tested by modelling the source of these tremor increases. Modelling of the tremor source is at the forefront of volcano seismological research and more work in this area of research should be pursued on White Island tremor.

Finally, investigating other unrest/eruptive episodes (e.g., the 1976-82 and 2000 periods) at White Island for similar unrest and eruption precursors than the ones characterised in this research would allow a generalisation of our results. However, this thesis demonstrated that valuable information on the state of the volcano can be gained using a multi-parameter monitoring strategy and a robust modelling approach. I provided evidence that the eruptions which occurred in 2012 and 2013 at White Island were preceded by measurable increased unrest (as measured by magnetic measurements and other parameters) and short-term precursory activity that can be used for eruption forecasting.

Appendix A

Correction of the gravity survey from tides using the local gPhone

The gravity survey data need to be corrected for the earth tides and ocean loading before further processing. Several softwares allow the computation of Earth tides (e.g., TSoft). The closest tidal gauge to White Island ($\sim$ 50 km south) could allow the correction for ocean loading. However, we noted that the continuous gravity station located on the island showed a phase delay (varying between surveys) with these tidal gauge data. We therefore chose to use this local continuous gravity station to correct for the Earth tides and ocean loading.

This process assumes that the gPhone only records the tides and its instrumental drift, and no volcanic signal. We checked this assumption by: 1. removing the theoretical earth tides at the gPhone location; 2. removing the ocean loading recorded at the closest tide gauge. After correction for the tides (Earth and ocean), the residuals are small during the surveys (+/-10 μGals around a linear trend ascribed to the drift of the instrument). This confirms that our assumption (the gPhone only records the tides and its drift) is reasonable for our periods of interest and that we can use the local gPhone (drift removed) to correct our survey data for Earth tides and ocean loading.

We computed the drift of the gPhone by 1. removing the Earth tides and 2. finding the best linear trend during our period of interest. We removed the drift from the gPhone without correcting for the ocean loading (correcting for them gives a very similar drift). The gPhone data at each survey occupation time with drift removed was then substracted to each survey gravity value.

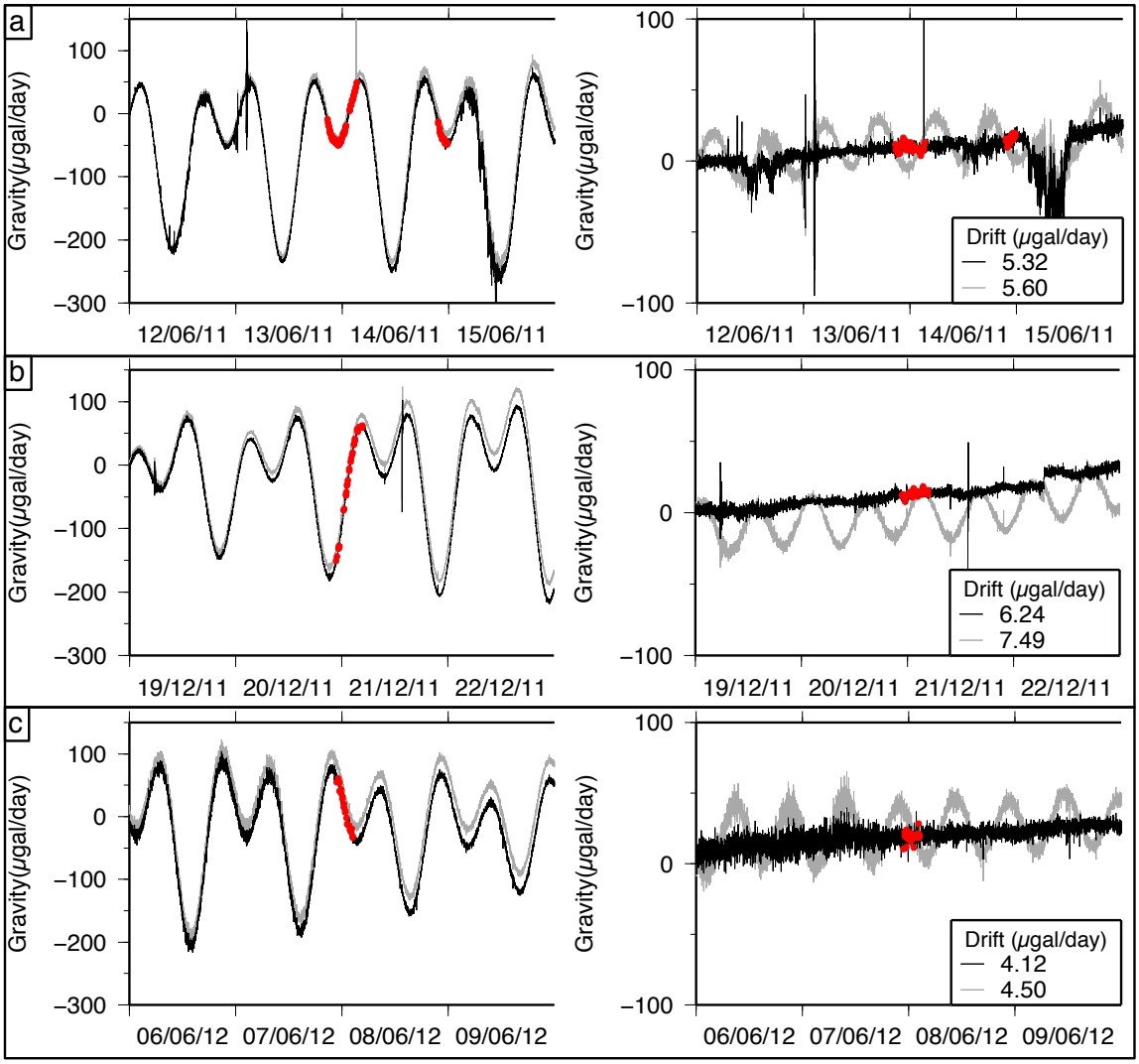

Figure A.1: Tide correction for the gravity data of a. the 6 June 2011 survey; b. the 11 December 2011 survey and c. the 6 June 2012 survey. The left panel shows the raw gPhone (grey) and dedrifted gPhone (black) used for correcting the gravity survey values from the tides, the right panel shows the raw gPhone corrected for Earth tides (grey) and raw gPhone corrected for earth tides and ocean loading (black). The red dots indicate the occupation times during the surveys. Note that the corrected gPhone (from Earth tides and ocean loading) shows little variation around a linear trend during our periods of interest suggesting that the gPhone only records the tides and its intrumental drift.

Appendix B

Data

B.1 Magnetic

Table B.1: Magnetic pegs location (WGS84).

Latitude	Longitude	Site
-37.52333	177.19228	Ma
-37.52333	177.19230	Ma2
-37.52333	177.19227	Map
-37.52340	177.19321	Mb
-37.52321	177.19228	Mc
-37.52319	177.19217	Md
-37.52289	177.19069	Me
-37.52286	177.18968	Mf
-37.52285	177.18958	Mg
-37.52315	177.18929	Mh
-37.52230	177.18906	Mi
-37.52153	177.18901	Mj
-37.52158	177.18872	Mk
-37.52185	177.18861	Ml
-37.52155	177.18756	Mm
-37.52157	177.18739	Mn1
-37.52158	177.18739	Mn2
-37.52158	177.18738	Mn3
-37.52131	177.18726	Mo

Magnetic pegs location (WGS84) (continued).

Latitude	Longitude	Site
-37.52088	177.18784	Mp
-37.52112	177.18700	Mq
-37.52099	177.18666	Mr
-37.52105	177.18657	Ms
-37.52080	177.18617	Mt1
-37.52080	177.18618	Mt2
-37.52067	177.18625	Mu
-37.52141	177.18614	Mv
-37.52157	177.18689	Mw
-37.52157	177.18691	Mw2
-37.52171	177.18656	Mx1
-37.52171	177.18657	Mx2
-37.52238	177.18646	My
-37.52264	177.18661	Mz
-37.52266	177.18661	Mz2
-37.52290	177.18672	MaA
-37.52287	177.18742	MaB1
-37.52288	177.18742	MaB2
-37.52244	177.18753	MaC
-37.52328	177.18767	MaD
-37.52338	177.18758	MaE
-37.52347	177.18794	MaF1
-37.52347	177.18794	MaF2
-37.52371	177.18839	MaG1
-37.52371	177.18838	MaG2
-37.52497	177.18993	MaH1
-37.52497	177.18992	MaH2
-37.52497	177.18994	MaH3
-37.52581	177.19144	VIII
-37.52531	177.19180	MaI1
-37.52531	177.19181	MaI2

Magnetic pegs location (WGS84) (continued).

Latitude	Longitude	Site
-37.52532	177.19181	MaI3
-37.52463	177.19270	AJp
-37.52456	177.19273	Aj
-37.52237	177.18832	MaJ
-37.52219	177.18819	MaK
-37.52038	177.18668	MaL
-37.52002	177.18596	MaM
-37.51994	177.18767	MaN
-37.52028	177.18843	MaO
-37.52103	177.18814	MaP
-37.52111	177.18825	MaQ
-37.52311	177.18681	MaR
-37.52326	177.18604	MaS
-37.52301	177.18697	MaT1
-37.52301	177.18698	MaT2
-37.52364	177.18843	MaU
-37.52208	177.18641	MDM1
-37.52220	177.18666	MDM2
-37.52181	177.18749	MDM3
-37.52242	177.18696	MDM4
-37.52183	177.18652	MDM5
-37.52123	177.18634	M1
-37.52364	177.19317	M2

Table B.2: Magnetic data in nT after each processing step.

Survey date	Site	Raw averaged	Diurnal variations corrected	Final (rel. to AjP)
20110524	Aj	53799.2	53801.4	86.9
	AJp	53711.5	53714.5	0
	Ma	53697.9	53699.5	-15
	MaA	53371.6	53372.8	-341.7
	MaB1	53365	53366.1	-348.4

Magnetic data in nT (continued).

Survey date	Site	Raw averaged	Diurnal variations corrected	Final (rel. to AjP)
	MaB2	53350.6	53352.2	-362.3
	MaC	53845.6	53846.9	132.4
	MaD	53632.2	53633.8	-80.7
	MaE	53747.6	53748.6	34.1
	MaF1	53635.5	53636.2	-78.3
	MaF2	53648	53649.8	-64.7
	MaG1	53750	53750.9	36.4
	MaG2	53786.6	53788	73.5
	MaH1	53696.2	53697.9	-16.6
	MaH2	53711.5	53713	-1.5
	MaH3	53732.5	53734	19.5
	MaI1	54142.1	54143.2	428.7
	MaI2	53987.7	53989.5	275
	MaJ	53903.6	53908	193.5
	MaK	53908.4	53913	198.5
	MaL	53897.2	53903	188.5
	MaM	53866.5	53872.4	157.9
	MaN	53560.4	53565.2	-149.3
	MaO	53538.9	53543.6	-170.9
	MaP	53821.7	53825.9	111.4
	MaQ	53831.7	53835.6	121.1
	MaR	53655.4	53658.7	-55.8
	MaS	53820.6	53823.2	108.7
	MaT1	53538.4	53541	-173.5
	MaT2	53515.5	53518	-196.5
	MaU	53750.2	53753	38.5
	Mb	53773.5	53775.9	61.4
	Mc	53677.8	53678.8	-35.7
	Md	53664.2	53665.5	-49
	Me	53708.4	53709.9	-4.6
	Mf	53981.7	53982.2	267.7

Magnetic data in nT (continued).

Survey date	Site	Raw averaged	Diurnal variations corrected	Final (rel. to AjP)
	Mg	53963.9	53964.8	250.3
	Mh	53855.4	53857.7	143.2
	Mi	53881	53881.3	166.8
	Mj	53654.2	53654	-60.5
	Mk	53770.8	53771.8	57.3
	Ml	53940.7	53941	226.5
	Mm	53985.8	53985.8	271.3
	Mn1	53951.2	53951.4	236.9
	Mn2	53920.1	53920.1	205.6
	Mo	54036.5	54038.9	324.4
	Mp	53782.6	53782.7	68.2
	Mq	54016.9	54017.5	303
	Mr	54134.1	54134.8	420.3
	Ms	54028.1	54028.3	313.8
	Mt1	54316.3	54315.2	600.7
	Mt2	54330.8	54329.6	615.1
	Mu	54154.5	54152.7	438.2
	Mv	54814.9	54815.3	1100.8
	Mw	54238.4	54239.7	525.2
	Mx1	54776.1	54787.8	1063.1
	Mx2	54786.5	54777.6	1073.3
	My	53701.5	53703.2	-11.3
	Mz	53373.6	53375.1	-339.4
	VIII	53786.7	53789.8	75.3
20120307	Aj	53788.4	53790.3	74.6
	AJp	53713.3	53715.7	0
	Ma	53681.1	53683	-32.7
	Ma2	53702.9	53704.8	-10.9
	MaA	53354.3	53360.4	-355.3
	MaB1	53341	53343	-372.7
	MaB2	53325.4	53328.7	-387

Magnetic data in nT (continued).

Survey date	Site	Raw averaged	Diurnal variations corrected	Final (rel. to AjP)
	MaC	53820	53824.8	109.1
	MaD	53609.8	53610.8	-104.9
	MaE	53726.7	53727.8	12.1
	MaF1	53604.7	53603.8	-111.9
	MaF2	53621.4	53621	-94.7
	MaG1	53727.5	53726.2	10.5
	MaG2	53766.1	53764.8	49.1
	MaH1	53661	53660.7	-55
	MaH2	53676.4	53676	-39.7
	MaH3	53713.1	53712.2	-3.5
	MaI2	53979.6	53982.7	267
	MaI3	53936.2	53939.5	223.8
	MaJ	53874.5	53880.8	165.1
	MaK	53878.4	53885.4	169.7
	MaL	53864.3	53870	154.3
	MaN	53535.1	53541	-174.7
	MaO	53523.2	53530	-185.7
	MaP	53803.5	53815.4	99.7
	MaQ	53814.4	53825.6	109.9
	MaR	53625.9	53630	-85.7
	MaS	53794.8	53800.2	84.5
	MaT1	53503.8	53507.5	-208.2
	MaT2	53482.7	53486	-229.7
	Mb	53765.2	53767.8	52.1
	Mc	53643.7	53645.7	-70
	Md	53636.7	53638.2	-77.5
	MDM1	55058.4	55063.3	1347.6
	MDM2	54410	54415.3	699.6
	MDM3	53931.6	53935	219.3
	MDM4	54249.1	54253.7	538
	Me	53680.3	53681.6	-34.1

Magnetic data in nT (continued).

Survey date	Site	Raw averaged	Diurnal variations corrected	Final (rel. to AjP)
	Mf	53953.4	53955.8	240.1
	Mg	53938.5	53942.2	226.5
	Mh	53832.5	53835.4	119.7
	Mi	53852.7	53857.4	141.7
	Mj	53633.5	53644	-71.7
	Mk	53748.4	53759	43.3
	Ml	53907.9	53917.6	201.9
	Mm	53962.9	53968.3	252.6
	Mn1	53921.2	53924	208.3
	Mn2	53887.7	53890.8	175.1
	Mo	54008.5	54010.2	294.5
	Mp	53763.2	53771	55.3
	Mq	53988.7	53990.8	275.1
	Mr	54087	54089.8	374.1
	Ms	53975.9	53979	263.3
	Mt1	54241.8	54245.8	530.1
	Mt2	54253.9	54258	542.3
	Mu	54084.4	54088.8	373.1
	Mv	54733.6	54737.3	1021.6
	Mw	54209.5	54212	496.3
	Mw2	54262.7	54265.4	549.7
	Mx1	54746.1	54748.4	1032.7
	Mx2	54757.6	54759.6	1043.9
	My	53678.1	53681.5	-34.2
	Mz	53351.3	53355.2	-360.5
	Mz2	53280.2	53284	-431.7
	VIII	53776.6	53781	65.3
20120608	Aj	53768.4	53767	61.3
	AJp	53704.9	53705.7	0
	M1	54097.6	54104.4	398.7
	M2	53842.4	53841.8	136.1

Magnetic data in nT (continued).

Survey date	Site	Raw averaged	Diurnal variations corrected	Final (rel. to AjP)
	Ma	53670.3	53668.8	-36.9
	Ma2	53700.1	53696.2	-9.5
	MaA	53363.1	53359	-346.7
	MaB1	53351.8	53348.8	-356.9
	MaB2	53340.1	53339.6	-366.1
	MaC	53824.7	53827	121.3
	MaD	53620.8	53617.8	-87.9
	MaE	53738	53732.7	27
	MaF1	53627.2	53622.7	-83
	MaF2	53633	53630.4	-75.3
	MaG1	53734.5	53728	22.3
	MaG2	53774.4	53769	63.3
	MaH1	53674	53668.1	-37.6
	MaH2	53694.7	53687.8	-17.9
	MaH3	53715.5	53710.4	4.7
	MaI1	54128.5	54124.6	418.9
	MaI2	53963.4	53960	254.3
	MaI3	53935.3	53932.6	226.9
	MaJ	53875	53877.4	171.7
	MaK	53880	53883.2	177.5
	MaL	53867.2	53874.8	169.1
	MaM	53842.1	53849.7	144
	MaN	53531.4	53539	-166.7
	MaO	53510.5	53517.6	-188.1
	Map	53664.7	53663	-42.7
	MaP	53785.7	53791	85.3
	MaQ	53797.5	53802.8	97.1
	MaR	53643.6	53639	-66.7
	MaS	53808.2	53805.6	99.9
	MaT1	53523.5	53516.8	-188.9
	MaT2	53500.9	53496.8	-208.9

Magnetic data in nT (continued).

Survey date	Site	Raw averaged	Diurnal variations corrected	Final (rel. to AjP)
	Mb	53750.7	53747.2	41.5
	Mc	53640.8	53639.2	-66.5
	Md	53644.8	53641.4	-64.3
	MDM1	55067.3	55065.8	1360.1
	MDM2	54405.8	54408.4	702.7
	MDM3	53933.5	53939	233.3
	MDM4	54255.9	54252.3	546.6
	MDM5	55348.7	55348.5	1642.8
	Me	53683.5	53684.4	-21.3
	Mf	53958.1	53960.8	255.1
	Mg	53937.8	53939.2	233.5
	Mh	53831	53832.6	126.9
	Mi	53852.7	53854.2	148.5
	Mj	53622.8	53626.2	-79.5
	Mk	53739.2	53742.8	37.1
	Ml	53915	53917.6	211.9
	Mm	53954.5	53960.9	255.2
	Mn1	53923.5	53931.2	225.5
	Mn2	53889	53896.8	191.1
	Mn3	53887.4	53895	189.3
	Mo	54010.1	54018.6	312.9
	Mp	53748.5	53753.8	48.1
	Mq	53988.9	53996.2	290.5
	Mr	54114.4	54122.8	417.1
	Ms	53998.4	54007	301.3
	Mt1	54278.6	54287	581.3
	Mt2	54291.8	54299.6	593.9
	Mu	54117.2	54124.6	418.9
	Mv	54787.7	54791.6	1085.9
	Mw	54210.3	54219.6	513.9
	Mw2	54269.1	54277.6	571.9

Magnetic data in nT (continued).

Survey date	Site	Raw averaged	Diurnal variations corrected	Final (rel. to AjP)
	Mx1	54759.2	54756.8	1051.1
	Mx2	54764.8	54764	1058.3
	My	53685.1	53682	-23.7
	Mz2	53289.8	53285.8	-419.9
	VIII	53763.1	53759.3	53.6
20121011	Aj	53772	53746.6	70.3
	AJp	53700	53676.3	0
	M1	54084	54071.1	394.8
	M2	53838	53809.8	133.5
	Ma	53670	53643.6	-32.7
	Ma2	53694	53666.1	-10.2
	MaA	53333	53330.6	-345.7
	MaB1	53317	53315.3	-361
	MaB2	53302	53300.8	-375.5
	MaC	53797	53793.7	117.4
	MaD	53592	53589.9	-86.4
	MaE	53703	53701.7	25.4
	MaF1	53586	53585.6	-90.7
	MaF2	53603	53602.4	-73.9
	MaG1	53697	53696.3	20
	MaG2	53737	53736.3	60
	MaH1	53641	53641.7	-34.6
	MaH2	53658	53658.2	-18.1
	MaH3	53684	53684.2	7.9
	MaI1	54121	54097	420.7
	MaI2	53956	53931.8	255.5
	MaI3	53927	53903.4	227.1
	MaJ	53868	53847.8	171.5
	MaK	53871	53851.2	174.9
	MaL	53873	53852.6	176.3
	MaM	53834	53819.6	143.3

Magnetic data in nT (continued).

Survey date	Site	Raw averaged	Diurnal variations corrected	Final (rel. to AjP)
	MaN	53334	53313.8	-362.5
	MaO	53512	53490.3	-186
	MaP	53784	53767.9	91.6
	MaQ	53797	53780.8	104.5
	MaR	53612	53608.8	-67.5
	MaS	53776	53773.5	97.2
	MaT1	53492	53489.2	-187.1
	MaT2	53467	53465.4	-210.9
	Mb	53747	53718.9	42.6
	Mc	53643	53615.4	-60.9
	Md	53642	53614.8	-61.5
	MDM1	55034	55029.8	1353.5
	MDM2	54383	54377.8	701.5
	MDM3	53911	53902.8	226.5
	MDM4	54218	54215	538.7
	MDM5	55318	55312	1635.7
	Me	53681	53657	-19.3
	Mf	53955	53932.2	255.9
	Mg	53932	53909.2	232.9
	Mh	53830	53806.6	130.3
	Mi	53846	53824.4	148.1
	Mj	53617	53600.3	-76
	Mk	53735	53718.3	42
	Ml	53907	53889.3	213
	Mm	53946	53933.7	257.4
	Mn1	53903	53894.6	218.3
	Mn2	53873	53863.5	187.2
	Mo	53996	53983.5	307.2
	Mp	53746	53730	53.7
	Mq	53975	53962.1	285.8
	Mr	54104	54092.6	416.3

Magnetic data in nT (continued).

Survey date	Site	Raw averaged	Diurnal variations corrected	Final (rel. to AjP)
	Ms	53982	53970.7	294.4
	Mt1	54269	54253.5	577.2
	Mt2	54281	54267.3	591
	Mu	54112	54096.7	420.4
	Mv	54789	54772.5	1096.2
	Mw	54189	54182.6	506.3
	Mw2	54246	54239.7	563.4
	Mx1	54745	54739	1062.7
	Mx2	54729	54722.9	1046.6
	My	53656	53652.8	-23.5
	Mz	53335	53332.6	-343.7
	Mz2	53262	53258.4	-417.9
	VIII	53738	53738	61.7
20150225	Aj	53673.4	53696.9	75.3
	AJp	53606.2	53621.6	0
	M1	53990	53991.6	370
	M2	53477	53487.1	-134.5
	Ma	53569.1	53589.3	-32.3
	Ma2	53591	53611.3	-10.3
	MaB1	53267.1	53259.1	-362.5
	MaC	53729.5	53727.1	105.5
	MaD	53544.3	53533.9	-87.7
	MaE	53656.1	53646.3	24.7
	MaF1	53540.8	53529.4	-92.2
	MaF2	53555.5	53543.9	-77.7
	MaG1	53653.3	53643.1	21.5
	MaG2	53691.4	53681.2	59.6
	MaH1	53595.5	53588.7	-32.9
	MaH3	53636.1	53628.9	7.3
	MaI1	53880.7	53878.9	257.3
	MaI2	54033.2	54030.8	409.2

Magnetic data in nT (continued).

Survey date	Site	Raw averaged	Diurnal variations corrected	Final (rel. to AjP)
	MaI3	53856.8	53855.3	233.7
	MaJ	53783.8	53793.8	172.2
	MaK	53784.6	53792.8	171.2
	MaL	53781.5	53786.3	164.7
	MaM	53750.1	53754.3	132.7
	Map	53568.5	53588.2	-33.4
	MaQ	53713.2	53719.3	97.7
	MaR	53561.3	53555.8	-65.8
	MaS	53724.6	53720	98.4
	Mb	53643.9	53665.1	43.5
	Mc	53538.9	53558	-63.6
	MDM3	53834.7	53834.5	212.9
	MDM4	54132.9	54133.5	511.9
	MDM5	55227.8	55228.4	1606.8
	Me	53591.8	53609.2	-12.4
	Mg	53845	53854.8	233.2
	Mi	53761.6	53771.8	150.2
	Mk	53651.3	53658.4	36.8
	Ml	53819.2	53825.5	203.9
	Mn1	53829.2	53827.9	206.3
	Mo	53911.6	53913.4	291.8
	Mq	53893.7	53894.9	273.3
	Mr	53959.9	53962.3	340.7
	Ms	53899.6	53902.1	280.5
	Mt2	54188.8	54192.4	570.8
	Mu	54024	54026.3	404.7
	Mw	54111.2	54112.5	490.9
	Mw2	54168.7	54170.1	548.5
	Mx1	54640.4	54641.1	1019.5
	VIII	53691.5	53685.8	64.2

B.2 Gravity

Table B.3: Gravity tiles location (WGS84).

Site	Longitude	Latitude	Elevation (m)
GR01	177.18991	-37.52499	9
GR02	177.18799	-37.52346	12
GR03	177.18674	-37.52287	24
GR04	177.18617	-37.52078	26
GR05	177.18657	-37.52171	31
GR06	177.18765	-37.52150	13
GR07	177.18872	-37.52158	16
GR08	177.18964	-37.52282	17
GR09	177.19229	-37.52332	7
GR10	177.19273	-37.52456	9

Table B.4: Gravity data in mGals after each processing step.

Survey date	Site	Raw	Tides corrected	Drift corrected
20110624	GR03	3670.368435	3670.320155	3670.324889
		3670.368435	3670.319973	
		3670.373670	3670.329805	
	GR02	3672.174510	3672.135826	3672.130506
		3672.176604	3672.139057	
	GR07	3673.064460	3673.032955	3673.017169
		3673.059225	3673.032327	
		3673.066554	3673.037620	
	GR03	3670.365294	3670.339621	3670.324889
		3670.370529	3670.349964	
	GR06	3672.434166	3672.418503	3672.389780
		3672.436260	3672.415404	
	GR05	3669.604125	3669.586517	3669.559152
		3669.609360	3669.591749	
		3669.607266	3669.588843	
	GR03	3670.371576	3670.354723	3670.324889

Gravity data in mGals (continued).

Survey date	Site	Raw	Tides corrected	Drift corrected
		3670.371576	3670.357794	
		3670.375764	3670.363186	
	GR05	3669.625065	3669.612881	3669.559152
		3669.630300	3669.613814	
		3669.628206	3669.613623	
	GR04	3669.693120	3669.683275	3669.637192
		3669.697308	3669.683531	
		3669.698355	3669.688485	
	GR06	3672.425790	3672.418638	3672.379768
		3672.431025	3672.422474	
		3672.415320	3672.404880	
	GR05	3669.604125	3669.595826	3669.559152
		3669.609360	3669.597108	
		3669.612501	3669.600747	
	GR06	3672.402756	3672.386829	3672.362746
		3672.413226	3672.396770	
		3672.415320	3672.403241	
	GR07	3672.017460	3672.003254	3672.967176
		3672.022695	3672.005030	
		3672.022695	3672.003748	
	GR04	3669.719295	3669.693034	3669.662291
		3669.722436	3669.697113	
		3669.725577	3669.701751	
	GR06	3672.425790	3672.399042	3672.368430
		3672.434166	3672.403889	
		3672.439401	3672.407135	
	GR05	3669.622971	3669.586508	3669.559149
		3669.632394	3669.596039	
		3669.635535	3669.596337	
	GR01	3673.718835	3673.656399	3673.660248
		3673.720929	3673.656394	

Gravity data in mGals (continued).

Survey date	Site	Raw	Tides corrected	Drift corrected
	GR10	3673.693707	3673.623156	3673.631161
		3673.701036	3673.629493	
		3673.703130	3673.631944	
	GR09	3673.517811	3673.438730	3673.442694
		3673.524093	3673.446480	
		3673.525140	3673.445691	
	GR01	3673.745010	3673.663685	3673.660461
		3673.752339	3673.667135	
		3673.754433	3673.667386	
	GR02	3672.222672	3672.129297	3672.130506
		3672.226860	3672.134612	
	GR08	3672.787005	3672.688019	3672.694243
		3672.792240	3672.692661	
	GR01	3673.755480	3673.648295	3673.660461
		3673.762809	3673.656125	
	GR02	3672.535725	3672.511483	3672.130506
		3672.537819	3672.514108	
	GR08	3673.074930	3673.054818	3672.679129
		3673.080165	3673.062890	
	GR02	3672.525255	3672.506515	3672.130506
		3672.525255	3672.509103	
	GR10	3674.043405	3674.027196	3673.657959
		3674.047593	3674.036781	
	GR09	3673.828770	3673.814439	3673.453552
		3673.834005	3673.824055	
		3673.836099	3673.825596	
	GR02	3672.507456	3672.497695	3672.130506
		3672.509550	3672.500210	
		3672.5105971	3672.498973	
20111221	GR02	177.902549	178.034121	178.032451
		177.903131	178.030780	

Gravity data in mGals (continued).

Survey date	Site	Raw	Tides corrected	Drift corrected
		177.905461	178.026464	
	GR03	176.167877	176.276156	176.290696
		176.169624	176.277561	
		176.171371	176.275435	
		176.173700	176.278467	
	GR04	175.455142	175.502953	175.522248
		175.458636	175.504099	
	GR03	176.237753	176.262441	176.295588
		176.240665	176.263255	
		176.247070	176.266871	
	GR02	177.986983	177.995993	178.032451
		177.989894	177.996907	
		177.992806	177.993207	
	GR01	179.545217	179.531093	179.574000
		179.546382	179.529181	
	GR10	179.514938	179.486720	179.535657
		179.517267	179.483261	
	GR01	179.558028	179.518293	179.574000
		179.559193	179.516711	
	GR02	178.026579	177.970139	178.032451
		178.027744	177.971967	
	GR03	176.176030	176.114235	176.172843
		176.175447	176.111305	
	GR04	175.555298	175.475632	175.536658
		175.558792	175.483193	
	GR06	178.306083	178.222493	178.278273
		178.306665	178.224154	
	GR08	178.620525	178.536741	178.590477
		178.621690	178.538369	
	GR02	178.066175	177.980742	178.032451
		178.065011	177.982676	

Gravity data in mGals (continued).

Survey date	Site	Raw	Tides corrected	Drift corrected
20120608	GR02	184.082499	183.988859	183.995160
		184.083664	184.001461	
	GR03	182.377525	182.288982	182.291008
		182.376360	182.292009	
	GR05	181.486606	181.404651	181.413196
		181.487770	181.419693	
	GR04	181.534354	181.463290	181.468361
		181.535519	181.470414	
	GR06	184.297950	184.241524	184.242250
		184.297950	184.238879	
	GR07	184.968760	184.925774	184.925418
		184.967595	184.919834	
	GR02	184.028927	183.994245	183.995160
		184.026598	183.989822	
	GR08	184.551833	184.526434	184.538931
		184.552997	184.537572	
	GR09	185.285531	185.271901	185.282862
		185.286695	185.272363	
	GR10	185.507969	185.501046	185.515347
		185.506805	185.501578	
	GR01	185.514957	185.512918	185.526802
		185.513792	185.506005	
	GR02	183.970697	183.974527	183.995160
		183.969533	183.975822	

Table B.5: Final gravity data.

Survey date	Site	Averaged data (mgals)	Relative to GR01
20110614	GR01	3673.6604	0
	GR02	3672.1305	-1.5299
	GR03	3670.3249	-3.3355
	GR04	3669.6497	-4.0107
	GR05	3669.5592	-4.1012
	GR06	3672.3752	-1.2852
	GR07	3672.9922	-0.6682
	GR08	3672.6867	-0.9737
	GR09	3673.4481	-0.2123
	GR10	3673.6446	-0.0158
20111221	GR01	179.5740	0
	GR02	178.0325	-1.5415
	GR03	176.1728 (AM: 176.2931)	-3.4012 (AM: -3.2809)
	GR04	175.5367 (AM: 175.5222)	-4.0373 (AM: -4.0518)
	GR06	178.2783	-1.2957
	GR08	178.5905	-0.9835
	GR10	179.5357	-0.0383
20120608	GR01	185.5268	0
	GR02	183.9952	-1.5316
	GR03	182.2910	-3.2358
	GR04	181.4684	-4.0584
	GR05	181.4132	-4.1136
	GR06	184.2423	-1.2845
	GR07	184.9254	-0.6014
	GR08	184.5389	-0.9879
	GR09	185.2829	-0.2439
	GR10	185.5153	-0.0115

Table B.6: Levelling and gravity changes (with and without elevation correction, using a Free-Air gradient of 3.086 $\times$ 10^{-4} mGal mm$-$1) between surveys.

Dates	Site	Gravity changes (mGal)	Levelling (mm)	Gravity, FAG corrected (mGal)
20110614–	GR01	0	0	0
20111221	GR02	-0.0116	-23	-0.0187
	GR03	-0.0657 (AM: 0.0546)	-30	-0.0564 (AM: 0.0639)
	GR04	-0.0266 (AM: -0.0411)	-8	-0.0241 (AM: -0.0386)
	GR06	-0.0105	-10	-0.0136
	GR08	-0.0098	-8	-0.0123
	GR10	-0.0225	-1	-0.0228
20111221–	GR01	0	0	0
20120608	GR02	0.0099	23.7	0.0172
	GR03	0.1654 (AM: 0.0451)	-12	0.1691 (AM: 0.0488)
	GR04	-0.0211 (AM: -0.0066)	34	-0.0106 (AM: 0.0039)
	GR06	0.0112	-1	0.0109
	GR08	-0.0044	26.5	0.0038
	GR10	0.0268	2	0.0274
20110614–	GR01	0	0	0
20120608	GR02	-0.0017	0.7	-0.0015
	GR03	0.0997	-50	0.0843
	GR04	-0.0477	16	-0.0428
	GR05	-0.0124	-11	-0.0158
	GR06	0.0007	-10	-0.0024
	GR07	0.0668	-5	0.0653
	GR08	-0.0142	18.5	-0.0085
	GR09	-0.0316	1	-0.0313
	GR10	0.0043	2.4	0.0050

Appendix C

Magnetic field due to a dipole–formulation

A magnetic dipole of dipole moment $\vec{m}$ (in SI unit A m^2) creates a magnetic field ($\vec{H}$) (or magnetic field strength, in SI unit A m^{-1}) which derives from a magnetic scalar potential (Φ_m) (Equation C.1).

$$\vec{H} = -\nabla\Phi_m \tag{C.1}$$

This magnetic scalar potential (Φ_m) obeys to the Laplace law (Equation C.2) outside the magnetic dipole.

$$\nabla^2\Phi_m = 0 \tag{C.2}$$

A solution of the Laplace law (Equation C.2) is:

$$\Phi_m = \frac{\vec{m}.\vec{r}}{4\pi r^3} \tag{C.3}$$

where $\vec{r}$ (in m) is the distance from the dipole centre to the surface location where the magnetic scalar potential is calculated.
$\vec{H}$ can then be deduced by combining Equations C.1 and C.3:

$$\vec{H} = -\frac{1}{4\pi}\nabla\frac{\vec{m}.\vec{r}}{r^3} \tag{C.4}$$

The magnetic induction ($\vec{B}$) (in SI unit Tesla (T)) is the total field and can be written as:

$$\vec{B} = \mu_0(\vec{H} + \vec{J}) \tag{C.5}$$

where μ_0 is the vacuum permeability ($= 4\pi \times 10^{-7}$ T m A^{-1}), and $\vec{J}$ is the magnetisation (or magnetic polarisation or dipole moment per unit volume, in SI unit A m^{-1}).

The magnetisation ($\vec{J}$) is proportional and in the same direction as $\vec{H}$ for low magnetic fields and is due to the fact that a magnetisable body placed in an external magnetic field becomes magnetised by induction which is due to the reorientation of atoms and molecules so that their spins line up.

$$\vec{J} = k\vec{H} \tag{C.6}$$

where k is the magnetic susceptibility (dimensionless parameter) measuring the degree to which a body is magnetised in reponse to an applied magnetic field.

Then,

$$\vec{B} = \mu_0(1+k)\vec{H} \tag{C.7}$$

Combining Equations C.4 and C.7 gives:

$$\vec{B} = \frac{\mu_0(1+k)}{4\pi}\nabla\frac{\vec{m}.\vec{r}}{r^3} \tag{C.8}$$

If the magnetic source is volumetric, then the magnetic dipole moment ($\vec{m}$) can be expressed as:

$$\vec{m} = \vec{J}V \tag{C.9}$$

where V is the volume of the magnetic body (in m^3).

For a volumetric source of magnetisation, $\vec{B}$ can finally be expressed as:

$$\vec{B} = \frac{\mu_0(1+k)}{4\pi}V\nabla\frac{\vec{J}.\vec{r}}{r^3} \tag{C.10}$$

where V $= \frac{4}{3}\pi a^3$ for a sphere, with a the radius of the sphere.

Given $\vec{B}$ the magnetic anomaly created by the dipole, $\vec{M}$ the measured magnetic field and $\vec{R}$ the regional magnetic field, we have $\vec{B} = \vec{M} - \vec{R}$. On the field, we measure M (i.e. the magnetic field intensity) and we know $\vec{R}$. If we assume that the magnetic anomaly is small compared to the regional magnetic field, then the definition of the magnetic anomaly $B = \vec{M} - \vec{R}$ implies that B is the projection of the anomaly field vector on the regional magnetic field vector. The magnetic anomaly is then defined by:

$$B = \vec{B}.\vec{R} \tag{C.11}$$

Bibliography

Acocella, V. (2014). Great challenges in volcanology: how does the volcano factory work? *Frontiers in Earth Science 2*, 1–10.

Afanasyev, A., A. Costa, and G. Chiodini (2015). Journal of Volcanology and Geothermal Research. *Journal of Volcanology and Geothermal Research 299*(C), 68–77.

Aki, K. and R. Koyanagi (1981). Deep volcanic tremor and magma ascent mechanism under Kilauea, Hawaii. *Journal of Geophysical Research: Solid Earth 86*(B8), 7095–7109.

Anderson, K. and P. Segall (2013). Bayesian inversion of data from effusive volcanic eruptions using physics-based models: Application to Mount St. Helens 2004-2008. *Journal of Geophysical Research: Solid Earth 118*(5), 2017–2037.

Aspinall, W. P. and G. Woo (2014). Santorini unrest 2011-2012: an immediate Bayesian belief network analysis of eruption scenario probabilities for urgent decision support under uncertainty. *Journal of Applied Volcanology 3*, 1–12.

Battaglia, M. and P. Segall (2004, May). The Interpretation of Gravity Changes and Crustal Deformation in Active Volcanic Areas. *Pure and Applied Geophysics 161*, 1453–1457.

Battaglia, M., C. Troise, F. Obrizzo, F. Pingue, and G. D. Natale (2006). Evidence for fluid migration as the source of deformation at Campi Flegrei caldera (Italy). *Geophysical Research Letters 33*(1), 4.

Bean, C. J., L. De Barros, I. Lokmer, J.-P. Métaxian, G. S. O'Brien, and S. Murphy (2014). Long-period seismicity in the shallow volcanic edifice formed from slow-rupture earthquakes. *Nature Geoscience 7*, 71–75.

Bell, A. F., J. Greenhough, M. J. Heap, and I. G. Main (2011). Challenges for forecasting based on accelerating rates of earthquakes at volcanoes and laboratory analogues. *Geophysical Journal International 185*(2), 718–723.

Bell, A. F., M. Naylor, M. J. Heap, and I. G. Main (2011). Forecasting volcanic eruptions and other material failure phenomena: An evaluation of the failure forecast method. *Geophysical Research Letters 38*(15), L15304.

Bell, A. F., M. Naylor, and I. G. Main (2013). The limits of predictability of volcanic eruptions from accelerating rates of earthquakes. *Geophysical Journal International 194*(3), 1541–1553.

Benoit, J. P., S. R. McNutt, and V. Barboza (2003). Duration - amplitude distribution of volcanic tremor. *Journal of Geophysical Research: Solid Earth 108*(B3), 2146.

Berrino, G. (1994). Gravity changes induced by height-mass variations at the Campi Flegrei caldera. *Journal of Volcanology and Geothermal Research 61*, 293–309.

Black, P. M. (1970). Observations on White Island volcano, New Zealand. *Bulletin of Volcanology 34*, 158–167.

Bloomberg, S., C. A. Werner, C. Rissmann, A. Mazot, T. Horton, D. M. Gravley, B. M. Kennedy, and C. Oze (2014). Soil CO2 emission as a proxy for heat and mass flow assessment, Taupo Volcanic Zone, New Zealand. *Geochemistry Geophysics Geosystems 15*, 1–20.

Bonaccorso, A., S. Calvari, G. Currenti, C. Del Negro, G. Ganci, A. T. Linde, R. Napoli, I. S. Sacks, and A. Sicali (2013, February). From source to surface: dynamics of Etna's lava fountains investigated by continuous strain, magnetic, ground and satellite thermal data. *Bulletin of Volcanology 75*(2), 690.

Boue, A., P. Lesage, G. Cortes, B. Valette, and G. A. Reyes-Davila (2015). Real-time eruption forecasting using the material Failure Forecast Method with a Bayesian approach. *Journal of Geophysical Research: Solid Earth 120*, 1–19.

Bouligand, C., J. M. G. Glen, and R. J. Blakely (2014). Distribution of buried hydrothermal alteration deduced from high-resolution magnetic surveys in Yellowstone National Park. *Journal of Geophysical Research: Solid Earth 119*.

Bruno, P. P. G., G. P. Ricciardi, Z. Petrillo, V. Di Fiore, A. Troiano, and G. Chiodini (2007, June). Geophysical and hydrogeological experiments from a shallow hydrothermal system at Solfatara Volcano, Campi Flegrei, Italy: Response to caldera unrest. *Journal of Geophysical Research 112*(B6), B06201.

Carn, S. A., J. S. Pallister, L. E. Lara, J. W. Ewert, S. F. L. Watt, A. J. Prata, R. J. Thomas, and G. Villarosa (2009). The unexpected awakening of Chaiten Volcano, Chile. *EOS Transactions AGU 90*(24), 205–212.

Carniel, R. (2010). Comments on the paper "Automatic detection and discrimination of volcanic tremors and tectonic earthquakes: An application to Ambrym volcano, Vanuatu" by Daniel Rouland, Denis Legrand, Mikhail Zhizhin and Sylvie Vergniolle. *Journal of Volcanology and Geothermal Research 194*(1-3), 61–62.

Carniel, R. (2014). Characterization of volcanic regimes and identification of significant transitions using geophysical data: a review. *Bulletin of Volcanology 76*, 848.

Carniel, R., O. Jaquet, and M. Tarraga (2008). Perspectives on the Application of the Geostatistical Approach to Volcano Forecasting at Different Time Scales. In *Caldera Volcanism: Analysis, modelling and response*, pp. 471–487. Developments in Volcanology.

Cashman, K. and J. Biggs (2014). Common processes at unique volcanoes—a volcanological conundrum. *Frontiers in Earth Science 2*, 1–4.

Cashman, K. V. and R. S. J. Sparks (2013). How volcanoes work: A 25 year perspective. *Geological Society of America Bulletin 125*(5-6), 664–690.

Chardot, L., B. W. Christenson, M. Todesco, A. W. Hurst, and N. Fournier (2013). Geophysical changes and hydrothermal activity at the early stage of the White Island 2012 unrest episode. In *IAVCEI 2013 Scientific Assembly, July 20-24*, Kagoshima, Japan.

Chardot, L., A. D. Jolly, B. M. Kennedy, N. Fournier, and S. Sherburn (2015, September). Using volcanic tremor for eruption forecasting at White Island volcano (Whakaari), New Zealand. *Journal of Volcanology and Geothermal Research 302*(C), 11–23.

Chiodini, G., M. Todesco, S. Caliro, C. Del Gaudio, G. Macedonio, and M. Russo (2003). Magma degassing as a trigger of bradyseismic events: The case of Phlegrean Fields (Italy). *Geophysical Research Letters 30*(8), 1434.

Chiodini, G., J. Vandemeulebrouck, S. Caliro, L. D'Auria, P. De Martino, A. Mangiacapra, and Z. Petrillo (2015). Evidence of thermal-driven processes triggering the 2005-2014 unrest at Campi Flegrei caldera. *Earth and Planetary Science Letters 414*(C), 58–67.

Chouet, B. A. (1996). Long-period volcano seismicity: its source and use in eruption forecasting. *Nature 380*, 309–316.

Chouet, B. A., R. A. Page, C. D. Stephens, J. C. Lahr, and J. A. Power (1994). Precursory swarms of long-period events at Redoubt Volcano (1989-1990), Alaska: Their origin and use as a forecasting tool. *Journal of Volcanology and Geothermal Research 62*, 95–135.

Christenson, B. W., A. G. Reyes, R. Young, A. Moebis, S. Sherburn, J. Cole-Baker, and K. Britten (2010, October). Cyclic processes and factors leading to phreatic eruption events: Insights from the 25 September 2007 eruption through Ruapehu Crater Lake, New Zealand. *Journal of Volcanology and Geothermal Research 191*(1-2), 15–32.

Christoffel, D. (1989). Variations in magnetic filed intensity at White Island volcano related to the 1976-82 eruption sequence. *N.Z. Geological Survey Bulletin 103*, 109–118.

Clark, R. H. and P. M. Otway (1989). Deformation monitoring associated with the 1976-82 White Island eruption sequence. *N.Z. Geological Survey Bulletin 103*, 69–84.

Cole, J. W. and K. B. Lewis (1981). Evolution of the Taupo-Hikurangi subduction system. *Tectonophysics 72*, 1–21.

Cole, J. W. and I. A. Nairn (1975). Catalogue of the active volcanoes of the world including Solfatara fields. *Part 22: New Zealand Int. Assoc. Volcanol. Chem. Earth Inter., Naples*.

Cole, J. W., T. Thordarson, and R. Burt (2000). Magma Origin and Evolution of White Island (Whakaari) Volcano, Bay of Plenty, New Zealand. *Journal of Petrology 41*(6), 867–895.

Cornelius, R. R. and B. Voight (1994). Seismological aspects of the 1989–1990 eruption at Redoubt Volcano, Alaska: the Materials Failure Forecast Method (FFM) with RSAM and SSAM seismic data. *Journal of Volcanology and Geothermal Research 62*, 469–498.

Cornelius, R. R. and B. Voight (1995). Graphical and PC-software analysis of volcano eruption precursors according to the Materials Failure Forecast Method (FFM). *Journal of Volcanology and Geothermal Research 64*(3), 295–320.

Cornelius, R. R. and B. Voight (1996). Real-time Seismic Amplitude Measurement (RSAM) and Seismic Spectral Amplitude Measurement (SSAM) Analyses with the Materials Failure Forecast Method (FFM), June 1991 Explosive Eruption at Mount Pinatubo. In C. G. Newhall and R. S. Punongbayan (Eds.), *Fire and Mud: Eruptions and Lahars of Mount Pinatubo, Philippines*, pp. 249–268. Seattle: University of Washinton Press.

Croucher, A. (2011). PyTOUGH: a Python scripting library for automating TOUGH2 simulations. In *Proceedings of the New Zealand Geothermal Workshop 2011*, pp. 1–6.

D'Agostino, M., G. Di Grazia, F. Ferrari, H. Langer, A. Messina, D. Reitano, and S. Spampinato (2013). Volcano monitoring and early warning on Mt. Etna, Sicily based on volcanic tremor: Methods and Technical aspects. In V. M. Zobin (Ed.), *Complex Monitoring of Volcanic Activity*, pp. 53–91. Nova Science Publishers, Inc.

Das, I. and M. D. Zoback (2013). Long-period long-duration seismic events during hydraulic stimulation of shale and tight-gas reservoirs — Part 2: Location and mechanisms. *Geophysics 78*(6), KS109–KS117.

De la Cruz-Reyna, S. and G. A. Reyes-Davila (2001). A model to describe precursory material-failure phenomena: applications to short-term forecasting at Colima volcano, Mexico. *Bulletin of Volcanology 63*(5), 297–308.

Endo, E. T. and T. Murray (1991). Real-time Seismic Amplitude Measurement (RSAM): a volcano monitoring and prediction tool. *Bulletin of Volcanology 53*(7), 533–545.

Fournier, N. (2003). *Shallow volcanic processes at persistently active volcanoes: evidence from a multidisciplinary study at Poas volcano, Costa Rica*. Ph. D. thesis, The Open University.

Fournier, N. and L. Chardot (2012). Understanding volcano hydrothermal unrest from geodetic observations: Insights from numerical modeling and application to White Island volcano, New Zealand. *Journal of Geophysical Research 117*, B11208.

Fry, B., L. Chardot, and A. D. Jolly (2015). Shallow velocity imaging of an active volcano. In *AGU Fall Meeting 2014, 15-19 December*, San Francisco.

Fukuzono, T. (1985). A new method for predicting the failure time of a slope. In *Proc IV International Conference and Field Workshop on Landslides*, Tokyo, Japan.

Fukuzono, T. and H. Terashima (1985). Experimental study of slope failure in cohesive soils caused by rainfall. In *International Symposium on Erosion, Debri Flow and Disaster Prevention*, Tsukuba, Japan.

Garcia, A., M. Berrocoso, J. M. Marrero, A. Fernández-Ros, G. Prates, S. De la Cruz-Reyna, and R. m. Ortiz (2014). Volcanic alert system (VAS) developed during the 2011–2014 El Hierro (Canary Islands) volcanic process. *Bulletin of Volcanology 76*(6), 825.

Gerstenberger, M. C. and D. A. Rhoades (2010). New Zealand Earthquake Forecast Testing Centre. *Pure and Applied Geophysics 167*(8-9), 877–892.

Giggenbach, W. (1987). Redox processes governing the chemistry of fumarolic gas discharges from White Island, New Zealand. *Applied Geochemistry 2*(2), 143–161.

Giggenbach, W., H. Shinohara, M. Kusakabe, and T. Ohba (2003). Formation of acid volcanic brines through interaction of magmatic gases, sea-water, and rock within the White Island volcanic-hydrothermal system, New Zealand . *Spec. Publ. Soc. Econ. Geol. 10*, 19–40.

Giggenbach, W. F. and G. P. Glasby (1977). The influence of thermal activity on the trace metal distribution in marine sediments around White Island, New Zealand. *DSIR Res. Bull. 218*, 121–126.

Giggenbach, W. F. and D. S. Sheppard (1989). Variations in the temperature and chemistry of White Island fumarole discharges 1972-85. *N.Z. Geological Survey Bulletin 103*, 119–126.

Gottsmann, J., A. G. Camacho, J. Marti, L. Wooller, J. Fernández, A. Garcia, and H. Rymer (2008, July). Shallow structure beneath the Central Volcanic Complex of Tenerife from new gravity data: Implications for its evolution and recent reactivation. *Physics of the Earth and Planetary Interiors 168*(3-4), 212–230.

Gottsmann, J., R. Carniel, N. Coppo, Wooller, S. Hautmann, and H. Rymer (2007). Oscillations in hydrothermal systems as a source of periodic unrest at caldera volcanoes: Multiparameter insights from Nisyros, Greece. *Geophysical Research Letters 34*, L07307.

Gottsmann, J., H. Rymer, and Wooller (2005). On the interpretation of gravity variations in the presence of active hydrothermal systems: Insights from the Nisyros Caldera, Greece. *Geophysical Research Letters 32*, L23310.

Gottsmann, J., L. Wooller, J. Marti, J. Fernández, A. G. Camacho, P. J. Gonzalez, A. Garcia, and H. Rymer (2006, October). New evidence for the reawakening of Teide volcano. *Geophysical Research Letters 33*(20), L20311.

Greenhough, J. and I. G. Main (2008). A Poisson model for earthquake frequency uncertainties in seismic hazard analysis. *Geophysical Research Letters 35*, L19313.

Gudmundsson, A., N. Lecoeur, N. Mohajeri, and T. Thordarson (2014). Dike emplacement at Bardarbunga, Iceland, induces unusual stress changes, caldera deformation, and earthquakes. *Bulletin of Volcanology 76*(10), 869.

Hammer, C. and J. W. Neuberg (2009). On the dynamical behaviour of low-frequency earthquake swarms prior to a dome collapse of Soufrière Hill volcano, Montserrat. *Geophysical Research Letters 36*(6), L06305.

Harris, A. J. L., R. Carniel, and J. Jones (2005). Identification of variable convective regimes at Erta Ale Lava Lake. *Journal of Volcanology and Geothermal Research 142*(3-4), 207–223.

Hashimoto, T., T. Mofi, N. Yasunori, Y. Ogawa, N. Ujihara, M. Oikawa, M. Saito, Nurhasan, S. Mizuhashi, T. Wakabayashi, R. Yoshimura, A. W. Hurst, M. Utsugi, and Y. Tanaka (2004). Self-Potential Studies in Volcanic Areas (5) - Rishiri, Kusatsu-Shirane, and White Island -. *Journal of Faculty of Science 12*(2), 93–113.

Heap, M. J., B. M. Kennedy, N. Pernin, L. Jacquemard, P. Baud, J. Farquharson, B. Scheu, Y. Lavallee, A. Gilg, M. Letham-Brake, K. Mayer, A. D. Jolly, T. Reuschle, and D. B. Dingwell (2015). Mechanical behaviour and failure modes within the White Island (Whakaari) volcano hydrothermal system, New Zealand. *Journal of Volcanology and Geothermal Research 295*, 26–42.

Hickey, J. and J. Gottsmann (2014). Benchmarking and developing numerical Finite Element models of volcanic deformation. *Journal of Volcanology and Geothermal Research 280*(C), 126–130.

Hincks, T., J.-C. Komorowski, S. R. Sparks, and W. P. Aspinall (2014). Retrospective analysis of uncertain eruption precursors at La Soufrière volcano, Guadeloupe, 1975–77: volcanic hazard assessment using a Bayesian Belief Network approach. *Journal of Applied Volcanology 3*, 1–26.

Houghton, B. F. and I. Nairn (1989a). A model for the 1976-82 phreatomagmatic and strombolian eruption sequence at White Island volcano, New Zealand. *N.Z. Geological Survey Bulletin 103*, 127–137.

Houghton, B. F. and I. Nairn (1989b). The phreatomagmatic and strombolian eruption events at White Island volcano 1976-82: Eruption narrative. *N.Z. Geological Survey Bulletin 103*, 13–23.

Houghton, B. F. and I. Nairn (1991). The 1976-82 strombolian and phreatomagmatic eruptions of White Island, New Zealand: eruptive and depositional mechanisms at a "wet" volcano . *Bulletin of Volcanology 54*, 25–49.

Hurst, A. W. and D. Christoffel (1973). Surveillance of White Island volcano, 1968-1972 Part 3: Thermo-magnetic effects due to volcanic activity. *New Zealand Journal of Geology and Geophysics 16*(4), 965–972.

Hurst, A. W., P. Rickerby, B. J. Scott, and T. Hashimoto (2004). Magnetic field changes on White Island, New Zealand, and the value of magnetic changes for eruption forecasting. *Journal of Volcanology and Geothermal Research 136*, 53–70.

Hurwitz, S., L. B. Christiansen, and P. A. Hsieh (2007). Hydrothermal fluid flow and deformation in large calderas: Inferences from numerical simulations. *Journal of Geophysical Research 112*, B02206.

Hutnak, M., S. Hurwitz, and S. E. Ingebritsen (2009). Numerical models of caldera deformation: Effects of multiphase and multicomponent hydrothermal fluid flow. *Journal of Geophysical Research 114*, B04411.

Ingebritsen, S. E., S. Geiger, S. Hurwitz, and T. Driesner (2010, March). Numerical simulation of magmatic hydrothermal systems. *Reviews of Geophysics 48*(1), RG1002.

Ingham, M. R. (1992). Audiomagnetotelluric soundings on White Island volcano. *Journal of Volcanology and Geothermal Research 50*(3), 301–306.

Jellinek, A. M. and D. Bercovici (2011). Seismic tremors and magma wagging during explosive volcanism. *Nature 470*, 522–525.

Johnston, M. J. S. (1997). Review of electric and magnetic fields accompanying seismic and volcanic activity. *Surveys in Geophysics 18*, 441–475.

Jolly, A. D., L. Chardot, J. Neuberg, N. Fournier, B. J. Scott, and S. Sherburn (2012). High impact mass drops from helicopter: A new active seismic source method applied in an active volcanic setting. *Geophysical Research Letters 39*, L12306.

Jolly, A. D., W. Power, N. Fournier, and X. Wang (2013). Capturing Transient Mass Changes for the 2011 Tohoku Tsunami on a Spring Gravity Meter. *Bulletin of the Seismological Society of America 103*(2B), 1622–1627.

Julian, B. R. (1994). Volcanic tremor: Nonlinear excitation by fluid flow. *Journal of Geophysical Research: Solid Earth 99*(B6), 11859–11877.

Kato, A., T. Terakawa, Y. Yamanaka, Y. Maeda, S. Horikawa, K. Matsuhiro, and T. Okuda (2015). Preparatory and precursory processes leadingup to the 2014 phreatic eruption of MountOntake, Japan. *Earth, planets and space 67*(111).

Kilburn, C. R. J. (2003). Multiscale fracturing as a key to forecasting volcanic eruptions. *Journal of Volcanology and Geothermal Research 125*, 271–289.

Kilburn, C. R. J. (2012). Precursory deformation and fracture before brittle rock failure and potential application to volcanic unrest. *Journal of Geophysical Research 117*(B2), B02211.

Kilburn, C. R. J. and B. Voight (1998). Slow rock fracture as eruption precursor at Soufriere Hills Volcano, Montserrat. *Geophysical Research Letters 25*(19), 3665–3668.

Konstantinou, K. I. and V. Schlindwein (2002). Nature, wavefield properties and source mechanism of volcanic tremor: a review. *Journal of Volcanology and Geothermal Research 119*, 161–187.

Kumagai, H. and B. A. Chouet (2000). Acoustic properties of a crack containing magmatic or hydrothermal fluids. *Journal of Geophysical Research: Solid Earth 105*(B11), 25–493–25–512.

Kumagai, H. and B. A. Chouet (2001). The dependence of acoustic properties of a crack on the resonance mode and geometry. *Geophysical Research Letters 28*(17), 3325–3328.

Latter, J. H., B. J. Scott, and R. Dibble (1989). Seismic activity associated with the 1976-82 eruption sequence at White Island volcano. *N.Z. Geological Survey Bulletin 103*, 85–107.

Leet, R. C. (1988). Saturated and subcooled hydrothermal boiling in groundwater flow channels as a source of harmonic tremor. *Journal of Geophysical Research 93*(B5), 4835–4849.

Legaz, A., J. Vandemeulebrouck, A. Revil, A. Kemna, A. W. Hurst, R. Reeves, and R. Papasin (2009, June). A case study of resistivity and self-potential signatures of hydrothermal instabilities, Inferno Crater Lake, Waimangu, New Zealand. *Geophysical Research Letters 36*(12), L12306.

Lesage, P., M. M. Mora, G. E. Alvarado, J. Pacheco, and J.-P. Métaxian (2006). Complex behavior and source model of the tremor at Arenal volcano, Costa Rica. *Journal of Volcanology and Geothermal Research 157*(1-3), 49–59.

Letham-Brake, M. (2013, November). *Geological constraints on fluid flow at Whakaari volcano (White Island)*. Ph. D. thesis, University of Canterbury.

López, C., M. J. Blanco, R. Abella, B. Brenes, V. M. Cabrera Rodríguez, B. Casas, I. Domínguez Cerdeña, A. Felpeto, M. F. De Villalta, C. Del Fresno, O. García, M. J. García-Arias, L. García-Cañada, A. Gomis Moreno, E. González-Alonso, J. Guzmán Pérez, I. Iribarren, R. López-Díaz, N. Luengo-Oroz, S. Meletlidis, M. Moreno, D. Moure, J. P. De Pablo, C. Rodero, E. Romero, S. Sainz-Maza, M. A. Sentre Domingo, P. A. Torres, P. Trigo, and V. Villasante-Marcos (2012). Monitoring the volcanic unrest of El Hierro (Canary Islands) before the onset of the 2011-2012 submarine eruption. *Geophysical Research Letters 39*(13), L13303.

Marzocchi, W., L. Sandri, and J. Selva (2008). BETEF: a probabilistic tool for long- and short-term eruption forecasting. *Bulletin of Volcanology 70*(5), 623–632.

McNutt, S. R. (1992). Volcanic tremor. *Encyclopedia of Earth System Science 4*, 417–425.

Menke, W. (2012). *Geophysical Data Analysis: Discrete Inverse Theory*. Elsevier Inc.

Mogi, K. (1958). Relations between the eruptions of various volcanoes and the deformations of the ground surfaces around them. *Bulletin of the Earthquake Research Institute 36*, 99–134.

Mongillo, M. and C. P. Wood (1995). Thermal infrared mapping of White Island volcano, New Zealand. *Journal of Volcanology and Geothermal Research 69*, 59–71.

Neuberg, J., R. Luckett, B. Baptie, and K. Olsen (2000). Models of tremor and low-frequency earthquake swarms on Montserrat. *Journal of Volcanology and Geothermal Research 101*, 83–104.

Newhall, C. G. and D. Dzurisin (1988). Historical Unrest at Large Calderas of the World. *U.S. Geological Survey Bulletin*, 1–1130.

Nishi, Y., T. Ishido, N. Matsushima, Y. Ogawa, T. Tosha, J. Miyazaki, A. Yasuda, B. J. Scott, S. Sherburn, and C. Bromley (1996). Self-potential and audio-magnetotelluric survey in White Island Volcano. In *Proceedings 18th NZ Geothermal Workshop*, pp. 237–242.

Nishi, Y., S. Sherburn, B. J. Scott, and M. Sugihara (1996). High-frequency earthquakes at White Island volcano, New Zealand: insights into the shallow structure of a volcano-hydrothermal system. *Journal of Volcanology and Geothermal Research 72*(3-4), 183–197.

Norton, D. (1984). Theory of hydrothermal systems. *Annual Reviews of Earth and Planetary Sciences 12*, 155.

Ortiz, R. m., H. Moreno, A. Garcia, G. Fuentealba, M. Astiz, P. Peña, N. Sánchez, and M. Tarraga (2003). Villarrica volcano (Chile): characteristics of the volcanic tremor and forecasting of small explosions by means of a material failure method. *Journal of Volcanology and Geothermal Research 128*, 247–259.

Peltier, A., B. J. Scott, and T. Hurst (2009). Ground deformation patterns at White Island volcano (New Zealand) between 1967 and 2008 deduced from levelling data. *Journal of Volcanology and Geothermal Research 181*, 207–218.

Pruess, K., C. M. Oldenburg, and G. Moridis (1999). *TOUGH2 User's Guide* (2.0 ed.).

Qamar, A. I., S. D. Malone, S. C. Moran, W. P. Steele, and T. W. e. A (2008). Near-Real-Time Information Products for Mount St. Helens—Tracking the Ongoing Eruption. In D. R. Sherrod, W. E. Scott, and P. H. Stauffer (Eds.), *A Volcano Rekindled: The Renewed Eruption of Mount St. Helens, 2004-2006*, pp. 61–70. U.S. Geological Survey Professional Paper.

Reyes-Davila, G. A. and S. De la Cruz-Reyna (2002). Experience in the short-term eruption forecasting at Volcan de Colima, Mexico, and public response to forecasts. *Journal of Volcanology and Geothermal Research 117*, 121–127.

Rikitake, T. and I. Yokoyama (1955). Volcanic activity and changes in geomagnetism. *Journal of Geophysical Research 60*(2), 165–172.

Rinaldi, A. P., M. Todesco, and M. Bonafede (2010). Hydrothermal instability and ground displacement at the Campi Flegrei caldera. *Physics of the Earth and Planetary Interiors 178*, 155–161.

Rinaldi, A. P., M. Todesco, J. Vandemeulebrouck, A. Revil, and M. Bonafede (2011). Electrical conductivity, ground displacement, gravity changes, and gas flow at Solfatara crater (Campi Flegrei caldera, Italy): Results from numerical modeling. *Journal of Volcanology and Geothermal Research 207*, 93–105.

Ripepe, M., A. J. L. Harris, and R. Carniel (2002). Thermal, seismic and infrasonic evidences of variable degassing rates at Stromboli volcano. *Journal of Volcanology and Geothermal Research 118*(3), 285–297.

Rogers, J. A. and C. D. Stephens (1995). SSAM: Real-Time Seismic Spectral Amplitude Measurement. *Bulletin of the Seismological Society of America 85*, 632–639.

Rouwet, D., L. Sandri, W. Marzocchi, J. Gottsmann, J. Selva, R. Tonini, and P. Papale (2014). Recognizing and tracking volcanic hazards related to non-magmatic unrest: a review. *Journal of Applied Volcanology 3*, 1–17.

Rymer, H. (1994). Microgravity change as a precursor to volcanic activity. *Journal of Volcanology and Geothermal Research 61*, 311–328.

Rymer, H. (1996). Microgravity Monitoring. In *Monitoring and Mitigation of Volcano Hazards*, pp. 1–29. Springer.

Sahagian, D. (2005, May). Volcanic eruption mechanisms: Insights from intercomparison of models of conduit processes. *Journal of Volcanology and Geothermal Research 143*(1-3), 1–15.

Scott, B. J., V. Manville, G. T. Hancox, W. D. Smith, and J. L. Hoverd (2004). Assessment of the risk posed by the Crater Lake, White Island. Technical Report 2004/28, Institute of Geological & Nuclear Sciences.

Shelly, D. R., G. C. Beroza, and S. Ide (2007). Non-volcanic tremor and low-frequency earthquake swarms. *Nature 446*, 305–307.

Sherburn, S. and B. J. Scott (1993). B-type volcanic earthquakes at White Island volcano, New Zealand. *Journal of Volcanology and Geothermal Research 56*, 351–355.

Sherburn, S., B. J. Scott, and A. W. Hurst (1996). Volcanic tremor and activity at White Island, New Zealand, JulySeptember 1991. *New Zealand Journal of Geology and Geophysics 39*, 329–332.

Sherburn, S., B. J. Scott, Y. Nishi, and M. Sugihara (1998). Seismicity at White Island volcano, New Zealand: a revised classification and inferences about source mechanism. *Journal of Volcanology and Geothermal Research 83*(3-4), 287–312.

Siebert, L., E. Cottrell, E. Venzke, and B. Andrews (2015). Earth's Volcanoes and Their Eruptions: An Overview. In H. Sigurdsson, B. F. Houghton, S. R. McNutt, H. Rymer, and J. Stix (Eds.), *The Encyclopedia of Volcanoes*, pp. 239–255. Elsevier.

Sigmundsson, F., A. Hooper, S. Hreinsdóttir, K. S. Vogfjörd, B. G. Ófeigsson, E. R. Heimisson, S. Dumont, M. Parks, K. Spaans, G. B. Gudmundsson, V. Drouin, T. Arnadottir, K. Jónsdóttir, M. T. Gudmundsson, T. Högnadóttir, H. M. Fridriksdóttir, M. Hensch, P. Einarsson, E. Magnússon, S. Samsonov, B. Brandsdóttir, R. S. White, T. Ágústsdóttir, T. Greenfield, R. G. Green, Á. R. Hjartardóttir, R. Pedersen, R. A. Bennett, H. Geirsson, P. C. La Femina, H. Björnsson, F. Pálsson, E. Sturkell, C. J. Bean, M. Möllhoff, A. K. Braiden, and E. P. S. Eibl (2014). Segmented lateral dyke growth in a rifting event at Bardarbunga volcanic system, Iceland. *Nature 517*(7533), 191–195.

Sparks, R. S. J. (2003). Forecasting volcanic eruptions. *Earth and Planetary Science Letters 210*(1), 1–15.

Stacey, F. D., K. G. Barr, and G. R. Robson (1965). The Volcano-magnetic Effect. *Pure and Applied Geophysics 62*, 96–104.

Tarraga, M., R. Carniel, R. m. Ortiz, and A. Garcia (2008). The Failure Forecast Method: Review and Application for the Real-Time Detection of Precursory Patterns at Reawakening Volcanoes. In J. Gottsmann and J. Marti (Eds.), *Caldera Volcanism: Analysis, modelling and response*, pp. 447–469. Elsevier.

Tarraga, M., R. Carniel, R. m. Ortiz, J. M. Marrero, and A. Garcia (2006). On the predictability of volcano-tectonic events by low frequency seismic noise analysis at Teide-Pico Viejo volcanic complex, Canary Islands. *Natural Hazards and Earth System Sciences 6*, 365–376.

Tarraga, M., R. m. Ortiz, A. Garcia, M. Hall, I. Molina, and A. Llinares (2004). Aplicacion del Material Failure Forecast Method (FFM) para el pronostico de la reactivacion del Volcan Tungurahua (Ecuador) en Agosto de 2003. In *Resumes 4 Asamblea Hispano-Portuguesa de Geodesia y Geofisica*, pp. 591–592.

Todesco, M. (2008). Hydrothermal fluid circulation and its effect on caldera unrest. In J. Gottsmann and J. Marti (Eds.), *Caldera volcanism: Analysis, Modelling and Response*, pp. 393–416. Elsevier.

Todesco, M. (2009). Signals from the Campi Flegrei hydrothermal system: Role of a "magmatic" source of fluids. *Journal of Geophysical Research 114*, B05201.

Todesco, M. and G. Berrino (2005). Modeling hydrothermal fluid circulation and gravity signals at the Phlegraean Fields caldera. *Earth and Planetary Science Letters 240*, 328–338.

Todesco, M., G. Chiodini, and G. Macedonio (2003). Monitoring and modelling hydrothermal fluid emission at La Solfatara (Phlegrean Fields, Italy). An interdisciplinary approach to the study of diffuse degassing. *Journal of Volcanology and Geothermal Research 125*(1-2), 57–79.

Todesco, M., A. P. Rinaldi, and M. Bonafede (2010). Modeling of unrest signals in heterogeneous hydrothermal systems. *Journal of Geophysical Research 115*, B09213.

Todesco, M., J. Rutqvist, G. Chiodini, K. Pruess, and C. M. Oldenburg (2004). Modeling of recent volcanic episodes at Phlegrean Fields (Italy): geochemical variations and ground deformation. *Geothermics 33*, 531–547.

Vandemeulebrouck, J., J.-C. Sabroux, H. M, Surono, P. N, J. Grangeon, and J. Tabbagh (2000). Hydroacoustic noise precursors of the 1990 eruption of Kelut Volcano, Indonesia. *Journal of Volcanology and Geothermal Research 97*, 443–456.

Vandemeulebrouck, J., D. Stemmelen, A. W. Hurst, and J. Grangeon (2005). Analogue modeling of instabilities in crater lake hydrothermal systems. *Journal of Geophysical Research 110*(B02212).

Voight, B. (1988). A method for prediction of volcanic eruptions. *Nature 332*, 125–130.

Voight, B. and R. R. Cornelius (1991). Prospects for eruption prediction in near real-time. *Nature 350*, 695–698.

Wardell, L., P. R. Kyle, N. Dunbar, and B. W. Christenson (2001). White Island volcano, New Zealand: carbon dioxide and sulfur dioxide emission rates and melt inclusion studies. *Chemical Geology 177*, 187–200.

Werner, C. A., A. W. Hurst, B. J. Scott, S. Sherburn, B. W. Christenson, K. Britten, J. Cole-Baker, and B. Mullan (2008). Variability of passive gas emissions, seismicity, and deformation during crater lake growth at White Island Volcano, New Zealand, 2002–2006. *Journal of Geophysical Research 113*, B01204.

Williams-Jones, G. and H. Rymer (2002). Detecting volcanic eruption precursors: a new method using gravity and deformation measurements. *Journal of Volcanology and Geothermal Research 113*(3-4), 379–389.

Williams-Jones, G., H. Rymer, G. Mauri, J. Gottsmann, M. Poland, and D. Carbone (2008, November). Toward continuous 4D microgravity monitoring of volcanoes. *Geophysics 73*(6), WA19–WA28.

Williams-Jones, G., H. Rymer, and D. A. Rothery (2003). Gravity changes and passive SO2 degassing at the Masaya caldera complex, Nicaragua. *Journal of Volcanology and Geothermal Research 123*(1-2), 137–160.

Wilson, C. J. N., B. F. Houghton, M. McWilliams, M. Lanphere, S. Weaver, and R. Briggs (1995). Volcanic and structural evolution of Taupo Volcanic Zone, New Zealand: a review. *Journal of Volcanology and Geothermal Research 68*, 1–28.

Wood, C. P. (1994). Mineralogy at the magma-hydrothermal system interface in andesite volcanoes, New Zealand. *Geology 22*(1), 75.

Woodward, D. and T. Mumme (1993). Variation of magnetisation on White Island, New Zealand. *New Zealand Journal of Geology and Geophysics 36*(4), 447–451.

Zlotnicki, J. and M. Bof (1998). Volcanomagnetic signals associated with the quasi-continuous activity of the andesitic Merapi volcano, Indonesia: 1990-1995. *Physics of the Earth and Planetary Interiors 105*(3-4), 119–130.

Zlotnicki, J. and J.-L. Le Mouel (1988). Volcanomagnetic effects observed on Piton de la Fournaise Volcano (Reunion Island): 1985-1987. *Journal of Geophysical Research 93*(B8), 9157–9171.

Zurek, J., G. William-Jones, D. Johnson, and A. Eggers (2012). Constraining volcanic inflation at Three Sisters Volcanic Field in Oregon, USA, through microgravity and deformation modeling. *Geochemistry Geophysics Geosystems 13*(10), Q10013.